2018

Direct analysis of solid samples by electrospray laser desorption ionization mass spectrometry imaging: From plants to pharmaceuticals

Patrick Alden Mcvey
Iowa State University

Direct analysis of solid samples by electrospray laser desorption ionization mass spectrometry imaging: From plants to pharmaceuticals

by

Patrick A. McVey

A dissertation submitted to the graduate faculty

in partial fulfillment of the requirements for the degree of

DOCTOR OF PHILOSOPHY

Major: Analytical Chemistry

Program of Study Committee:
Robert S. Houk, Major Professor
Young-Jin Lee
Basil J. Nikolau
Joseph Burnett
Robbyn Anand

The student author, whose presentation of the scholarship herein was approved by the program of study committee, is solely responsible for the content of this dissertation. The Graduate College will ensure this dissertation is globally accessible and will not permit alterations after a degree is conferred.

Iowa State University

Ames, Iowa

2018

TABLE OF CONTENTS

Page

ACKNOWLEDGMENTS

First and foremost I would like to thank my mentor, Dr. Houk, for taking me on as his final graduate student! I would like to especially thank him for allowing me the freedom to take care of my family while pursuing my graduate education, as well as all his help and guidance throughout my time at ISU. I must acknowledge my wife Brittany for all her support throughout our 5 years here; I couldn't have done it without her! Also, thanks to my daughter Brielle (and baby #2), she was the best motivation to finish my degree. I cannot forget my parents too, I wouldn't be here without them!

I have been supported by many extraordinary coworkers during my research career at ISU and Ames Lab. Stan Bajic was an exceptional help in getting the ELDI method working and interpreting data, as well as a good friend. Katie-Jo Galayda was the best group member I've ever worked with, and made our small group not so lonely! Tim Anderson was instrumental in preparing me for research during my first year.

The second and third chapters of this dissertation could not have been done without the help of Liza Alexander! Thank you for growing the plants, analyzing the biology portion, and being a good friend! Similarly, chapter four couldn't have been accomplished without Xinyu Fu, who was also a huge help with the biology and a good friend! Greg Webster has been a huge help with the pharmaceutical portion of this dissertation, and I've always enjoyed his witty comments.

I would also like to thank my committee for their involvement during my tenure here at ISU. The ELDI experiments could not have been done without the support of Dr. Lee, who provided the laser and guidance during project meetings. Dr. Nikolau's

guidance was also imperative for the biology and chapter 3. Dr. Burnett was an excellent teaching mentor, preparing me for a career in academia (hopefully!). I always enjoyed talking with Joe about students, teaching, and sarcasm. I also want to thank Dr. Anand for agreeing to serve on my committee at the last minute!

Last, but certainly not least, I would like to thank North Grand Christian Church and pastor Mike Morton for their support of me and my family during our time in Ames. Our spiritual growth through the past five years could not have happened without NGCC and Mike, and we cannot thank them enough for the impact they have had on my family's lives. It was by my faith in Jesus that I got this far, and for this I must thank Christ for His sacrifice that we may live in Him.

"And whatever you do, whether in word or deed, do it all in the name of the Lord Jesus, giving thanks to God the Father through him." Colossians 3:17

ABSTRACT

This dissertation describes new applications for electrospray laser desorption ionization mass spectrometry imaging (ELDI-MSI). While ELDI was introduced over a decade ago, relatively few technical advancements or applications have been published. ELDI combines laser ablation with an ultraviolet (UV) laser with electrospray ionization (ESI). A similar method using an infrared (IR) laser known as laser ablation electrospray ionization (LAESI) operates under the same general setup as ELDI. However, the inherent shorter wavelengths used allow for ELDI to achieve higher spatial resolutions when compared with LAESI. Thus, ELDI was used on various plant samples as a comparison to studies done with LAESI, but at greater spatial resolutions than reported in those studies. The results using ELDI were shown to be comparable to LAESI.

A more extensive study on plant leaves was done to show the applicability of ELDI to study biological pathways and phenomena. Light exposure was altered across coleus leaves and the differences in concentrations of sugars, amino acids, and flavonoids were monitored over time. Using ELDI-MSI, a source-sink relationship between the two halves of each leaf was observed.

Next, the uptake of isotopically labeled glucose media was observed in Arabidopsis plants over a two-week time period. This was done at high spatial resolution (50 µm) for an atmospheric pressure, matrix-free method. Plants grown in the isotopically labeled glucose solution were shown to have isotopically enriched amino acid signals in the mass spectra and corresponding MS-images. This showed that the

glucose media directly participated in the biological pathways which make the amino acids. The localization of the glucose uptake was observed in the MS-images.

LAESI utilizing an IR laser needs appreciable water content for an ablation event to occur. However, ELDI using a UV laser does not. Therefore, ELDI can analyze “dry” samples where traditional LAESI cannot. This led to the analysis of pharmaceutical tablets with ELDI and its capability to image tablets was demonstrated. The study was the first application of either LAESI or ELDI to image tablets, and the first MSI-method to diagnose agglomeration and crystallinity in pills. This is important to the pharmaceutical industry, as crystallinity alters the bioavailability of active pharmaceutical ingredients.

CHAPTER 1.

GENERAL INTRODUCTION

Mass Spectrometry Imaging

Many well-established analytical methods have been put into practice to elucidate chemical information. Mass spectrometry (MS) is one of the most widely used techniques due to its superior sensitivity and wide ranging applications. While separations in the form of chromatography commonly precede detection by MS, important spatial information about the distributions of compounds is lost.[1] The spatial distributions of compounds in their natural biological matrices contain important information for the fields of lipidomics, metabolomics, and proteomics.[2,3,4] Similarly, biomedical research benefits greatly from accumulation information of drug-uptake in animal tissue.[5]

Recently, mass spectrometry imaging (MSI) has emerged as a viable source of spatial distribution data utilizing the sensitivity and versatility that MS provides. Since MSI is a non-targeted technique it is not limited to detection of a single compound of interest, but can concurrently provide valuable molecular distribution data for different classes of compounds. This has led to an explosion of applications and ionization mechanisms for MSI in the past decade.[6]

In principle, MSI requires extraction and ionization of analyte molecules from a sample surface in a spatially resolved manner.[7] This is typically done by rastering a laser beam or solvent stream across the sample surface. The spatial positioning of the beam is related to mass spectra collected at that specific time point. Each individual point

across the sample surface is then combined to form a molecular map and compared to an optical image of the sample. **Figure 1** shows how mass spectra combine to form an MS-image. A point-by-point rastering method allows mass spectra to be collected from compounds in a confined spatial area which determines the lateral resolution of the ionization method. Since data are collected for the entire m/z range, molecular distribution maps can be created for all detected compounds from a single MSI acquisition. An important consideration when using MSI is that analyte extraction and ionization efficiency may differ based on the makeup of biological sample matrices.[8] This effect is also called ion suppression. For example, when imaging a biological sample that has two very different types of tissues, the laser energy absorbance may differ between those tissues, thus extraction and ionization of analyte molecules may also differ.

Many factors must be taken into consideration when choosing an MSI method. As previously mentioned, there have been a number of ionization methods introduced for MSI and each have their own advantages and drawbacks. MSI methods are generally compared by their spatial resolution, ion source pressure, and sample preparation protocols.[9] Higher spatial resolutions have allowed techniques such as matrix-assisted laser desorption ionization (MALDI) MSI to collect sub-cellular data.[10] While a higher spatial resolution is almost always desirable, data collection and analysis times are subsequently increased. The most commonly used imaging techniques (e.g. MALDI and secondary ion mass spectrometry (SIMS)) usually operate under vacuum.[9] This is a factor in the superior spatial resolution associated with these methods, due to a high ion

extraction efficiency under reduced pressure. However there are benefits to analyzing samples in their native environment at atmospheric pressure (AP), which has led to the introduction of AP techniques such as desorption electrospray ionization (DESI), laser ablation electrospray ionization (LAESI), and electrospray laser desorption ionization (ELDI).[6] Sample preparation is also a key factor which differs based on the MSI method utilized. Treating the sample prior to analysis can improve ion yields, but can also be time consuming and alter the sample surface.[11]

This dissertation focuses on ELDI-MSI applications for plant metabolomics and pharmaceutical preparations. The most common ionization sources for these fields will be explained in more detail. These sources include MALDI, DESI, and LAESI. The recent contributions to these two fields for each method will also be discussed. Subsequently, a description of ELDI-MSI and its potential for analysis of plants and pharmaceutical preparations will be discussed. **Figure 2** shows the key differences in these four ionization sources.

MALDI-MSI

MALDI is the most widely used ionization source for MSI. MALDI requires the uniform application of a matrix (often a small organic compound) across the entire surface of the sample.[12] This applied matrix absorbs the energy from an incident laser beam and facilitates desorption of analyte molecules. Upon desorption of both matrix and analyte compounds, ionization transfer of the energy absorbing matrix and the analyte molecules takes place, although this process is not fully understood.

MALDI is a well-researched method that has many different matrices available for different analyses. Careful deposition of the ionization matrix is important and the matrix particle size can determine the spatial resolution of MALDI experiments.[10] Extensive sample preparation, such as sectioning or using a cryostat, before matrix application may be needed depending on the sample.

MALDI has been demonstrated with both IR and UV lasers, although UV lasers are more common. One of the biggest advantages for MALDI is its soft ionization, leading to little fragmentation of analyte ions. Important for the field of proteomics, MALDI can measure large molecules (>100 kDa), but has also been demonstrated to be effective in the field of metabolomics.[13] Typical MALDI ion sources operate under vacuum to increase ion yields and spatial resolution, but AP-MALDI has been demonstrated at high spatial resolutions for small molecules. Under vacuum, spatial resolutions of 1 µm have been reported. Using MALDI under high vacuum however can lead to loss of small volatile molecules and takes the sample out of its native environment, possibly altering sample morphology.[9]

As reported by Roessner[14] in 2015, MALDI accounts for approximately half of all plant-based MSI papers. Achieving high spatial resolution and utilizing a multiplex imaging approach for more robust analysis of plant tissues has been discussed.[15] Continued research in MALDI matrices for plant endogenous compounds is needed for MALDI-MSI.[16] MALDI-MSI has been used for multiple types of plant tissue including roots, stems, leaves, flowers, fruit, and seeds.[16] High resolution MALDI (~5 µm) has been shown to spatially resolve lipids and metabolites in maize roots.[17] While the lower mass

range can have matrix-ion interferences with MALDI, recent studies have shown its utility for imaging plant metabolites in this lower mass range.[18,19] MALDI-MSI has been especially successful for interrogating physiological information on biological processes in plant leaves.[14,20,21]

MALDI-MSI has been reported extensively for use in drug metabolism studies. For example, MALDI-MSI has tracked drug development in brain tissue[22], as well as distribution of drugs in organs[23] and tumors.[24] MALDI-MSI has even been shown at atmospheric pressure at very high resolution (<2 µm).[25] However, very little research has been done using MALDI-MSI for imaging active pharmaceutical ingredients (API) in tablet formulations.[26] The first example was done by Earnshaw et al.[27] as a proof-of-concept. In this study, MALDI was shown to work on a variety of tablets for API imaging. However, due to the need for a flat surface for matrix-application, certain tablets could not be imaged. One issue the authors identified with using MALDI-MSI for tablet imaging was the need to ablate through the external tablet coating. Also, certain shapes and textures of tablets made surface imaging difficult.

Another example of MALDI-MSI on pharmaceutical tablets was by Gut and coworkers.[28] In this study, MALDI-MSI was combined with statistical analysis methods to determine variation in MALDI matrices and spatial distributions of active ingredients. The authors tested their method on a home-made aspartame tablet and the commercial tablet Coversyl® 4 mg. This study had the same constraints as the aforementioned MALDI-MSI experiment, as both were sensitive to tablet features and homogeneous matrix application.

DESI-MSI

Introduced in 2004 by Cooks' group[29], DESI uses a charged solvent stream from an altered ESI source to desorb and ionize surface molecules from a solid sample. DESI doesn't require extensive sample preparation and is operated at AP. Since DESI is a non-destructive method, as opposed to laser-based MSI methods, it has the advantage of preserving most of the sample for additional analyses (e.g. histology). However, the surface is somewhat altered after DESI analysis. While DESI cannot achieve the high resolutions that MALDI boasts, lateral resolutions of <50 µm have been reported with a nano-spray capillary known as nano-DESI.[30] One downside to DESI is its sensitivity to the properties of the sample surface due to the desorption process. Thus, an imprinting process is sometimes used to account for uneven sample surfaces.[31] The desorption solvent used can also lead to selective extraction, skewing results.[27] The mass range for DESI is limited to below 2000 Da, so it is better suited for analysis of lipids, metabolites, and small peptides.[14]

DESI is the most widely used non laser-based MSI method. Many variations of DESI have been introduced, which are discussed in review articles.[4-6] For example, a recently demonstrated method called reactive nano-DESI adds reactive chemical species into the ESI stream to target specific chemical classes.[32] DESI-MSI has spatially resolved flavonoids, sugars, anthocyanins, glycoalkaloids, and secondary metabolites in plant samples.[33]

DESI-MSI has been shown to identify counterfeit pharmaceuticals qualitatively.[34] Using MSI, it was determined that counterfeit drug manufacturers were adept at

creating pharmaceutical preparations due a homogeneous spatial distribution of drug compounds in counterfeit tablet samples. In this study, DESI-MSI was done in conjunction with nuclear magnetic resonance (NMR) spectroscopy and direct analysis in real-time (DART) MS for a multi-faceted forensic analysis. This was the first real application of MSI on pharmaceutical preparations found in the literature.[26] In 2013, Cooks' lab demonstrated the use of fiducial markers in combination with DESI-MSI on pharmaceutical tablets. This method was shown to be a possible tool for quality control and counterfeit drug identification.[35]

LAESI-MSI

LAESI utilizes an IR laser (typically 2940 nm) on water-rich samples for ablation with post-ionization via ESI.[36] The laser energy is absorbed by water which acts as a pseudo-matrix. This makes LAESI quite applicable for biological samples. The laser ablation event is due to heating caused by water absorbing the IR radiation (through the O-H bond vibration), causing vaporization of surface molecules. The ablation plume is mostly neutral, hence the need for the addition of the ESI source. Charged droplets from the ESI interact with the ablation plume, transferring charge and extracting analyte molecules from sample particulates in the ablation plume.[37] A similar method introduced before LAESI called matrix-assisted laser desorption electrospray ionization (MALDESI) uses the same general setup as LAESI but with an externally applied matrix (similar to MALDI) and charged sample slide.[38] However, MALDESI has been shown to work with ice as a matrix, ultimately using water as a pseudo-matrix, similar to LAESI.[39]

Although LAESI now has a commercial source available (Protea LAESI DP-1000[40]), it still has not been widely used for plant metabolomics beyond proof-of-concept studies.[41] This is partly due to its poor spatial resolution (~200 µm) relative to reduced pressure MALDI. Many of these proof-of-principle studies have been done with modified LAESI sources on plant samples.[41] LAESI was successful in imaging flavonoids and other small metabolites in various plant samples.[42] Recently, single-cell LAESI-MSI has been reported, but was limited to very large cells (>100 µm).[43,44] LAESI has also been used in tandem with other methods for semi-quantitative MSI in plant leaves.[45]

Before this dissertation, the only moderately detailed plant study using LAESI-MSI was done by Etalo and coworkers.[46] This previous study analyzed metabolite changes in infected tomato leaves. This showed the applicability of LAESI for plant metabolomics, but suffered from a lateral resolution of 500 µm.

Since its introduction, LAESI has seen many advances and applications. For example, coupling LAESI-MSI to ion mobility separation (IMS) has been shown to concurrently image and separate isobaric compounds.[47] LAESI in tandem with IMS has been used on plants, although without MSI.[48] While not as adept at analyzing proteins as MALDI, LAESI-MSI has been used to image small proteins in mouse lungs.[49] Another study has explored the utility of LAESI-MSI for 3D imaging of bacteria with lipids and peptides reported.[50] However, LAESI-MSI has not been reported for use in studying the morphology of pharmaceutical preparations.

Another ion source was introduced using an infrared laser called laser ablation metastable-induced chemical ionization (LAMICI).[51] This was used to image tablets, but

only for proof of concept. LAMICI was successful in detecting the API in acetaminophen tablets. None of the aforementioned MSI studies diagnosed agglomeration or crystallinity in pharmaceutical preparations.

ELDI-MSI

ELDI was first introduced by Shiea and coworkers[52] in 2005, and was the first MS ionization method to couple laser desorption with electrospray ionization. ELDI is analogous to LAESI, but uses a UV laser. This difference has specific implications on the analyte extraction process as the incident photons are not absorbed by water in the sample, but by UV-absorbing compounds in the natural sample matrix.[53] Therefore, ELDI can desorb molecules from samples without appreciable water content whereas conventional LAESI cannot. Due to the inherent shorter wavelengths of UV lasers, ELDI has the potential to achieve much lower spot sizes and therefore better spatial resolutions as compared to IR-laser based methods.[54] As long as a sample has UV-absorbing molecules an ablation event will occur, thus extracting analyte compounds from the natural sample matrix. Due to the addition of post-ionization via ESI, no applied matrix is needed for ionization of non UV-absorbers. The specifics of the ELDI ionization source[55] are discussed in the Chapter 2 materials and methods section. **Figure 3A** shows the ELDI-MSI source setup used for the work in this dissertation. **Figure 3B** is a schematic of the mass spectrometer utilized.

Laser desorption ionization (LDI) using a UV laser without post-ionization via electrospray has been used by Svatos[56] at subcellular spatial resolutions, but suffers

from low ionization efficiency (~1% ion yield as compared with MALDI). Only strong absorbers at the particular laser wavelength used are ionized and ultimately detected. The addition of ESI after the laser ablation event allows for extracted molecules that are not ionized by the laser desorption process to be detected.

ELDI has not been as widely used as the previously discussed ionization methods. This is in part due to the lack of a commercial ELDI source.[57] ELDI-MSI has been used on fungi[58] as well as plant and animal tissues[53] to show its capabilities. However, ELDI-MSI for plants has not been explored beyond brief proof-of-concept studies. While ELDI has successfully shown to determine API content in tablets[59], ELDI-MSI has not been explored for these samples. ELDI has seen some technique advancements, such as liquid-ELDI using an inorganic matrix in solutions to detect proteins[60] and reactive-ELDI for proteomic studies using reactants in the ESI solution.[61] However, ELDI-MSI has not seen major technical advancement since its introduction thirteen years ago.[57]

This thesis describes applications of ELDI-MSI to the field of plant metabolomics and the pharmaceutical industry. This is the first time ELDI-MSI has been used to interrogate spatial distributions of small molecules (<1200 Da) in plants. This method was successful in imaging flavonoids, carbohydrates, amino acids, and organic acids in multiple types of plant leaves. Also described is one of the few MSI studies on pharmaceutical preparations, and the first using MSI to diagnose crystallinity and agglomeration.

Dissertation Organization

This dissertation is organized into six chapters and two appendices. This first chapter discusses the commonly used MSI methods for plant metabolomics and pharmaceutical analysis. Chapter 2 discusses our initial work with ELDI-MSI on plant tissue. The method specifics of the ELDI experiment are discussed in the chapter 2 experimental section. Chapter 3 demonstrates the ability of ELDI-MSI for biological applications. This chapter uses ELDI-MSI to track metabolic changes due to environmental stimuli in coleus leaves. Chapter 4 shows the ability of high-resolution ELDI-MSI at 50 µm lateral resolution for studies of Arabidopsis plants. Arabidopsis grown in isotopically labeled glucose solutions were monitored via ELDI-MSI to track glucose uptake in amino acids over the course of 14 days. Chapter 5 is the first application of ELDI-MSI to image APIs in pharmaceutical preparations, and the first MSI method to diagnose crystallinity and agglomeration. Chapter 6 is a summary of the work done in this thesis and discusses directions for future experiments.

Appendix A is additional work done on coleus leaves to track pathway preference of anthocyanin biosynthesis. My contribution to this work was supporting analysis of MS and MSI data, and peak identification. Appendix B discusses new nitrides grown in a calcium-rich flux and their crystalline structure. My contribution to this work was inductively coupled plasma mass spectrometry (ICP-MS) for elemental analysis of sample crystals.

References

1) Norris, J. L. and Caprioli, R. M., Imaging mass spectrometry: A new tool for pathology in a molecular age. Prot. Clin. Appl., **2013**, 7: 733-738.

2) Goto-Inoue, N., Hayasaka, T., Zaima, N., Setou, M., Imaging mass spectrometry for lipidomics, Biochimica et Biophysica Acta (BBA) - Molecular and Cell Biology of Lipids, **2011**, 1811: 961-969.

3) Aichler, M., & Walch, A., MALDI imaging mass spectrometry: current frontiers and perspectives in pathology research and practice. Laboratory Investigation, **2015**, 95: 422–431.

4) Sturtevant, D., Lee, Y. J., Chapman, K. D., Matrix assisted laser desorption/ionization-mass spectrometry imaging (MALDI-MSI) for direct visualization of plant metabolites in situ. Current Opinion in Biotechnology, **2016**, 37: 53-60.

5) Swales, J. G., Hamm, G., Clench, M. R., Goodwin, R. J. A., Mass spectrometry imaging and its application in pharmaceutical research and development: A concise review. International Journal of Mass Spectrometry, **2018**, In Press.

6) Perez, C.J., Bagga, A.K., Prova, S., Taemeh, M.Y., Ifa, D.R., Review and perspectives on the applications of mass spectrometry imaging under ambient conditions. Rapid Commun. Mass Spectrom., **2018**, In Press.

7) McDonnell, L.A., Römpp, A., Balluff, B. et al. Discussion point: reporting guidelines for mass spectrometry imaging. Analytical and Bioanalytical Chem., **2015**, 407: 2035-2045.

8) Hölscher, D. , Shroff, R. , Knop, K. , Gottschaldt, M. , Crecelius, A. , Schneider, B. , Heckel, D. G., Schubert, U. S., and Svatoš, A., Matrix-free UV-laser desorption/ionization (LDI) mass spectrometric imaging at the single-cell level: distribution of secondary metabolites of Arabidopsis thaliana and Hypericum species. The Plant Journal, **2009**, 60: 907-918.

9) Spengler, B., Mass Spectrometry Imaging of Biomolecular Information. Analytical Chemistry, **2015**, 87: 64−82.

10) Baker, T. C., Han, J., Borchers, C. H., Recent advancements in matrix-assisted laser desorption/ionization mass spectrometry imaging. Current Opinion in Biotechnology, **2017**, 43: 62-69.

11) Wu, C., Dill, A. L., Eberlin, L. S., Cooks, R. G. and Ifa, D. R., Mass spectrometry imaging under ambient conditions. Mass Spectrom. Rev., **2013**, 32: 218-243.

12) Caprioli, R.M., Farmer, T.B., Gile, J., Molecular imaging of biological samples: localization of peptides and proteins using MALDI-TOF MS. Anal. Chem., **1997**, 69: 4751–4760.

13) Lee, Y. J., Perdian, D. C., Song, Z. , Yeung, E. S. and Nikolau, B. J., Use of mass spectrometry for imaging metabolites in plants. The Plant Journal, **2012**, 70: 81-95.

14) Boughton, B.A., Thinagaran, D., Sarabia, D., Bacic, A., Roessner, U., Mass spectrometry imaging for plant biology: a review. Phytochem. Rev., **2015**, 15: 445-488.

15) R. L. Hansen, Y. J. Lee, High-spatial resolution MSI toward single cell metabolomics in plant tissues. The Chemical Record, **2018**, 18, 65.

16) Qin, L., Zhang, Y., Liu, Y., He, H., Han, M., Li, Y., Zeng, M., Wang, X., Recent advances in matrix-assisted laser desorption/ionization mass spectrometry imaging (MALDI-MSI) for in situ analysis of endogenous molecules in plants. Phytochemical Analysis. **2018**; 1-14.

17) Feenstra, A.D., Dueñas, M.E., & Lee, Y.J., Five micron high resolution MALDI mass spectrometry imaging with simple, interchangeable, multi-resolution optical system. J. Am. Soc. Mass Spectrom., **2017**, 28: 434-442.

18) Misiorek, M., Sekula, J., Ruman T., Mass spectrometry imaging of lowmolecular weight compounds in garlic (Allium sativum L.) with gold nanoparticle enhanced target. Phytochem Anal., **2017**; 28: 479-486.

19) Korte, A.R., Lee, Y.J., MALDI-MS analysis and imaging of small molecule metabolites with 1,5-diaminonaphthalene (DAN). J. Mass Spectrom., **2014**, 49: 737-741.

20) Shroff, R., Schramm, K., Jeschke, V., Nemes, P., Vertes, A., Gershenzon, J., Svatos, A., Quantification of plant surface metabolites by matrix-assisted laser desorption-ionization mass spectrometry imaging: glucosinolates on Arabidopsis thaliana leaves. Plant J., **2015**, 81:961-972.

21) Poth, A.G., Mylne, J.S., Grassl, J., Lyons, R.E., Miller, A.H., Colgrave, M.L., Craik, D.J., Cyclotides associate with leaf vasculature and are the products of a novel precursor in petunia (Solanaceae). J Biol Chem., **2012**, 287: 27033-27046.

22) Takai, N., Tanaka, Y., Inazawa, K., Saji, H., Quantitative analysis ofpharmaceutical drug distribution in multiple organs by imaging massspectrometry. Rapid Commun. Mass Spectrom., **2012**, 26: 1549–1556.

23) Liu, X., Ide, J.L., Norton, I., Marchionni, M.A., Ebling, M.C., Wang, L.Y., Davis, E., Sauvageot, C.M., Kesari, S., Kellersberger, K.A., Easterling, M.L., Santagata, S., Stuart, D.D., Alberta, J., Agar, J.N., Stiles, C.D., Agar, N.Y.R., Molecular imaging of drug transit through the blood-brain barrier with MALDI mass spectrometry imaging. Sci. Rep. 3, **2013**, 2859.

24) S.J. Atkinson, P.M. Loadman, C. Sutton, L.H. Patterson, M.R. Clench, Examination of the distribution of the bioreductive drug AQ4N and its activemetabolite AQ4 in solid tumours by imaging matrix-assisted laserdesorption/ionisation mass spectrometry, Rapid Commun. Mass Spectrom., **2007**, 21: 1271–1276.

25) Kompauer, M., Heiles, S., & Spengler, B., Atmospheric pressure MALDI mass spectrometry imaging of tissues and cells at 1.4-µm lateral resolution. Nature Methods, **2017**, 14: 90–96.

26) Kempson, I.M., Prestidge, C.A., Mass Spectrometry Imaging of Pharmaceuticals: From Tablets to Tissues. In: Müllertz A., Perrie Y., Rades T. (eds) Analytical Techniques in the Pharmaceutical Sciences. Advances in Delivery Science and Technology, **2016**, Springer, New York, NY.

27) Earnshaw, C. J., Carolan, V. A., Richards, D. S. and Clench, M. R., Direct analysis of pharmaceutical tablet formulations using matrix-assisted laser desorption/ionisation mass spectrometry imaging. Rapid Commun. Mass Spectrom., **2010**, 24: 1665-1672.

28) Gut, Y., Boiret, M., Bultel, L., Renaud, T., Chetouani, A., Hafiane, A., Ginot, Y-M., Jennane, R., Application of chemometric algorithms to MALDI mass spectrometry imaging of pharmaceutical tablets. Journal of Pharmaceutical and Biomedical Analysis, **2015**, 105: 91-100.

29) Takats, Z., Wiseman, J.M., Gologan, B., Cooks, R.G., Mass spectrometry sampling under ambient conditions with desorption electrospray ionization. Science, **2004**, 306: 471-473.

30) Lanekoff, I., Heath, B. S., Liyu, A., Thomas, M., Carson, J. P., and Laskin, J., Automated platform for high-resolution tissue imaging using nanospray desorption electrospray ionization mass spectrometry. Analytical Chemistry, **2012**, 84: 8351-8356.

31) Ifa, D.R., Srimany, A., Eberlin, L.S., Naik, H.R., Bhat, V., Cooks, R.G., and Pradeep, T., (2011) Tissue imprint imaging by desorption electrospray ionization mass spectrometry. Anal. Methods, **2011**, 3: 1910.

32) Laskin, J., Eckert, P.A., Roach, P.J., Heath, B.S., Nizkorodov, S.A., and Laskin, A., Chemical Analysis of Complex Organic Mixtures Using Reactive Nanospray Desorption Electrospray Ionization Mass Spectrometry. Analytical Chemistry, **2012**, *84*: 7179-7187.

33) Bjarnholt, N., Li, B., D'Alvise, J., and Janfelt, C., Mass spectrometry imaging of plant metabolites – principles and possibilities (Review Article). Nat. Prod. Rep., **2014**, 31: 818- 837

34) Nyadong, L., Harris, G.A., Balayssac, S., Galhena, A.S., Malet-Martino, M., Martino, R., Parry, R.M., Wang, M.D., Fernández, F.M., and Gilard, V., Combining Two-Dimensional Diffusion-Ordered Nuclear Magnetic Resonance Spectroscopy, Imaging Desorption Electrospray Ionization Mass Spectrometry, and Direct Analysis in Real-Time Mass Spectrometry for the Integral Investigation of Counterfeit Pharmaceuticals. Analytical Chemistry, **2009**, 81: 4803-4812.

35) Ferreira, C.R., Wu, L., Vogt, F.G., Bornancini, E.R., & Cooks, R.G., Fiducial Markers for Distribution of Drug and Excipient on Tablet Surfaces by Multimodal Desorption Electrospray Ionization–Mass Spectrometry (DESI–MS) Imaging. Analytical Letters, **2013**, 47(1): 91-101.

36) Nemes, P., and Vertes, A., Laser Ablation Electrospray Ionization for Atmospheric Pressure, in Vivo, and Imaging Mass Spectrometry. Analytical Chemistry, **2007**, 79(21): 8098-8106.

37) Nemes, P., Barton, A.A, Li, Y., and Vertes. A., Ambient Molecular Imaging and Depth Profiling of Live Tissue by Infrared Laser Ablation Electrospray Ionization Mass Spectrometry. Analytical Chemistry, **2008**, 80(12): 4575-4582

38) Sampson, J.S., Hawkridge, A.M., Muddiman, D.C., Generation and Detection of Multiply-Charged Peptides and Proteins by Matrix-Assisted Laser Desorption Electrospray Ionization (MALDESI) Fourier Transform Ion Cyclotron Resonance Mass Spectrometry. Journal of the American Society for Mass Spectrometry, **2006**, 17(12): 1712-1716.

39) Robichaud, G., Barry, J. A., & Muddiman, D. C., IR-MALDESI MASS SPECTROMETRY IMAGING OF BIOLOGICAL TISSUE SECTIONS USING ICE AS A MATRIX. Journal of the American Society for Mass Spectrometry, **2014**, 25(3): 319–328.

40) http://www.proteabio.com/laesi-dp-1000-specifications.html

41) Bartels, B., & Svatoš, A., Spatially resolved in vivo plant metabolomics by laser ablation-based mass spectrometry imaging (MSI) techniques: LDI-MSI and LAESI. Frontiers in Plant Science, **2015**, 6: 471.

42) Nemes, P., Barton, A. A., and Vertes, A., Three-dimensional imaging of metabolites in tissues under native conditions by laser ablation electrospray ionization mass spectrometry. Anal. Chem., **2009**, 81: 6668–6675.

43) Stolee, J. A., Shrestha, B., Mengistu, G., and Vertes, A., Observation of Subcellular Metabolite Gradients in Single Cells by Laser Ablation Electrospray Ionization Mass Spectrometry. Angew. Chem. Int. Ed., **2012**, 51: 10386-10389.

44) Shrestha, B., Patt, J.M., and Vertes, A., In Situ Cell-by-Cell Imaging and Analysis of Small Cell Populations by Mass Spectrometry. Analytical Chemistry, **2011**, 83(8): 2947-2955.

45) Shroff, R., Schramm, K., Jeschke, V., Nemes, P., Vertes, A., Gershenzon, J. and Svatoš, A., Quantification of plant surface metabolites by matrix-assisted laser desorption–ionization mass spectrometry imaging: glucosinolates on Arabidopsis thaliana leaves. Plant Journal, **2015**, 81: 961-972.

46) Etalo, D.W., De Vos, R.C.H., Joosten, M.H.A.J., Hall, R.D., Spatially Resolved Plant Metabolomics: Some Potentials and Limitations of Laser-Ablation Electrospray Ionization Mass Spectrometry Metabolite Imaging. Plant Physiology, **2015**, 169(3): 1424-1435.

47) Li, H., Smith, B.K., Márk, L., Nemes, P., Nazarian, J., Vertes, A., Ambient molecular imaging by laser ablation electrospray ionization mass spectrometry with ion mobility separation. International Journal of Mass Spectrometry, **2015**, 377: 681-689.

48) Stopka, S. A., Agtuca, B. J., Koppenaal, D. W., Paša-Tolić, L. , Stacey, G. , Vertes, A. and Anderton, C. R., Laser-ablation electrospray ionization mass spectrometry with ion mobility separation reveals metabolites in the symbiotic interactions of soybean roots and rhizobia. Plant Journal, **2017**, 91: 340-354.

49) Kiss, A. , Smith, D. F., Reschke, B. R., Powell, M. J. and Heeren, R. M., Top-down mass spectrometry imaging of intact proteins by laser ablation ESI FT-ICR MS. Proteomics, **2014**, 14: 1283-1289.

50) Li, H., Balan, P., Vertes, A., Molecular Imaging of Growth, Metabolism, and Antibiotic Inhibition in Bacterial Colonies by Laser Ablation Electrospray Ionization Mass Spectrometry. Angew Chem Int Ed., **2016**, 55(48):15035-15039.

51) Galhena, A.S., Harris, G.A., Nyadong, L., Murray, K.K., and Fernandez, F.M., Small Molecule Ambient Mass Spectrometry Imaging by Infrared Laser Ablation Metastable-Induced Chemical Ionization. Anal. Chem., **2010**, 82: 2178–2181.

52) Shiea, J., Huang, M., HSu, H., Lee, C., Yuan, C., Beech, I., and Sunner, J., Electrospray-assisted laser desorption/ionization mass spectrometry for direct ambient analysis of solids. Rapid Commun. Mass Spectrom., **2005**, 19: 3701-3704.

53) Huang M.Z., Jhang S.S., Shiea J., Electrospray Laser Desorption Ionization (ELDI) Mass Spectrometry for Molecular Imaging of Small Molecules on Tissues. In: He, L. (eds) Mass Spectrometry Imaging of Small Molecules. Methods in Molecular Biology (Methods and Protocols), **2015**, vol 1203. Humana Press, New York, NY.

54) Shinn, M., Basics of Lasers and Laser Optics. In: Schaaf P. (eds) Laser Processing of Materials. Springer Series in Materials Science, **2010**, vol 139. Springer, Berlin, Heidelberg.

55) Galayda, K.J., Use of ultraviolet laser ablation electrospray ionization mass spectrometry for plant metabolite imaging. Iowa State University Graduate Theses and Dissertations, **2017**, 15517.

56) Hölscher, D., Shroff, R., Knop, K., Gottschaldt, M., Crecelius, A., Schneider,B. , Heckel, D.G., Schubert, U. S. and Svatoš, A., Matrix-free UV-laser desorption/ionization (LDI) mass spectrometric imaging at the single-cell level: distribution of secondary metabolites of Arabidopsis thaliana and Hypericum species. The Plant Journal, **2009**, 60: 907-918.

57) Cheng, S-C., Shiea, C., Huang, Y-L., Wang, C-H., Cho, Y-T., and Shiea, J., Laser-based ambient mass spectrometry (Minireview). Anal. Methods, **2017**, 9: 4924-4935.

58) Huang, M-Z., Cheng, S-C., Jhang, S-S., Chou, C-C., Cheng, C-N., Shiea, J., Popov, I.A., Nikolaev, E.N., Ambient molecular imaging of dry fungus surface by electrospray laser desorption ionization mass spectrometry. International Journal of Mass Spectrometry, **2012**, 325–327: 172-182.

59) Huang, M., Hsu, H., Wu, C., Lin, S., Ma, Y., Cheng, T. and Shiea, J., Characterization of the chemical components on the surface of different solids with electrospray-assisted laser desorption ionization mass spectrometry. Rapid Commun. Mass Spectrom., **2007**, 21: 1767-1775.

60) Shiea, J., Yuan, C-H., Huang, M-Z., Cheng, S-C., Ma, Y-L., Tseng, W-L., Chang, H-C., and Hung, W-C., Detection of Native Protein Ions in Aqueous Solution under Ambient Conditions by Electrospray Laser Desorption/Ionization Mass Spectrometry. Analytical Chemistry, **2008**, 80(13): 4845-4852.

61) Peng, I.X., Loo, R.R.O., Shiea, J., and Loo, J.A., Reactive-Electrospray-Assisted Laser Desorption/Ionization for Characterization of Peptides and Proteins. Analytical Chemistry, **2008**, 80(18): 6995-7003.

Figures

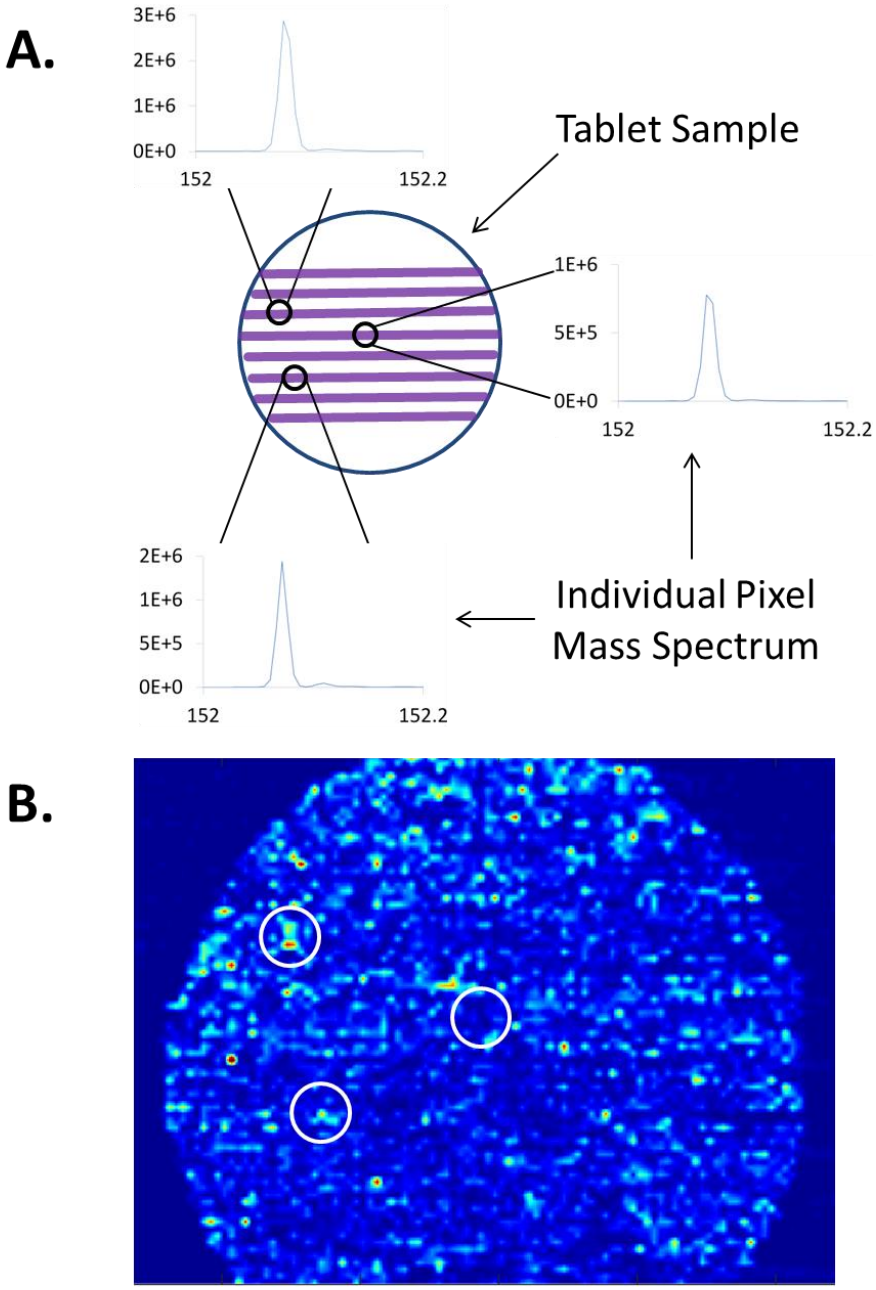

Figure 1. Mass spectra combining to form an MS-image. **A)** Tablet sample with ablation trenches formed by a UV laser using ELDI-MSI. Individual pixels are circled on the tablet sample figure, which correspond to the mass spectra of acetaminophen $[M+H]^+$ shown. **B)** An MS-image of a tablet sample. The white circles represent the same spatial positions in **1A**. When the relative ion count for acetaminophen is higher the intensity shown in the MS-image shows a subsequent increase at that spatial position.

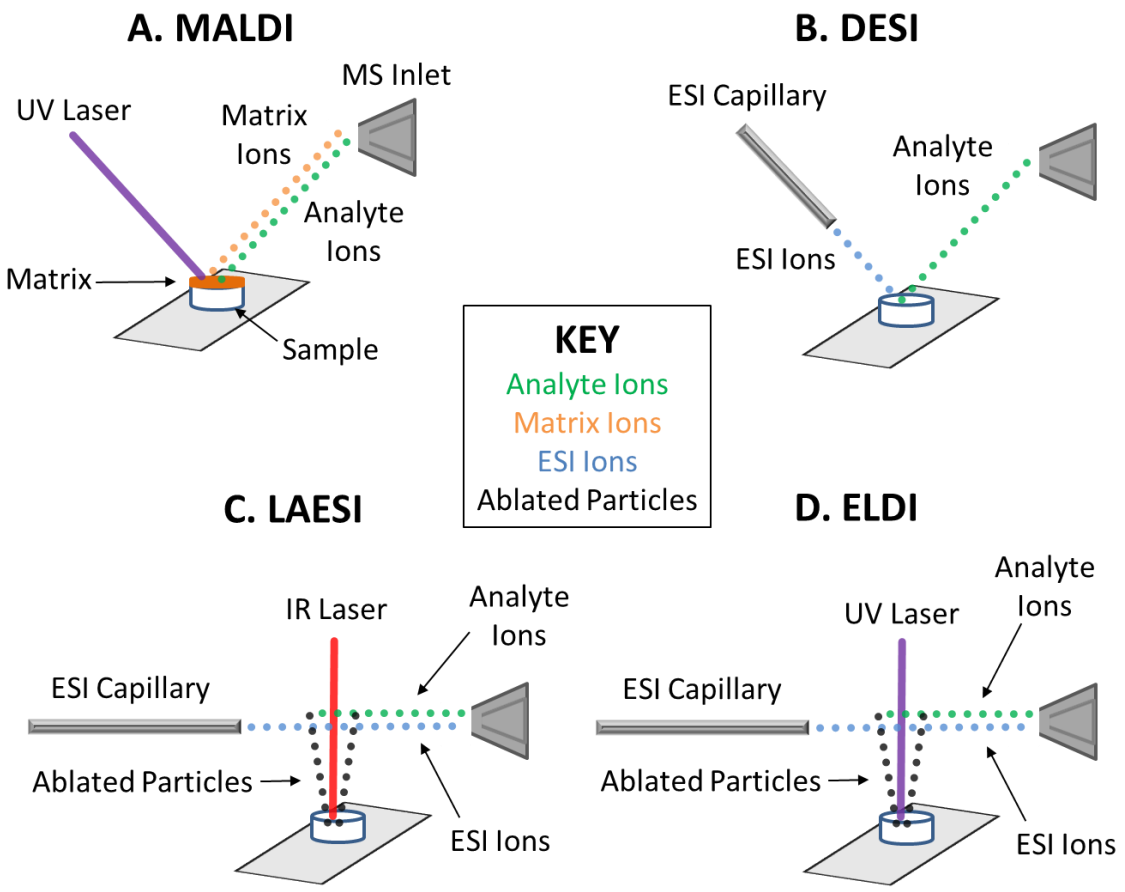

Figure 2. Schematics of the four ionization sources discussed in this chapter. **A)** MALDI is shown ablating a sample covered in a UV-absorbing matrix at atmospheric pressure. Both matrix and analyte ions are detected. **B)** DESI is shown desorbing analyte ions from the sample surface with a directed ESI solvent. **C)** LAESI is shown ablating a sample with an IR laser, causing an explosion of particulates. The ablated particles interact with the ESI solvent and ESI ions as well as analyte ions are detected. **D)** ELDI is shown using the same general setup as LAESI, but with a UV laser for ablation. Again, both analyte and ESI ions are detected.

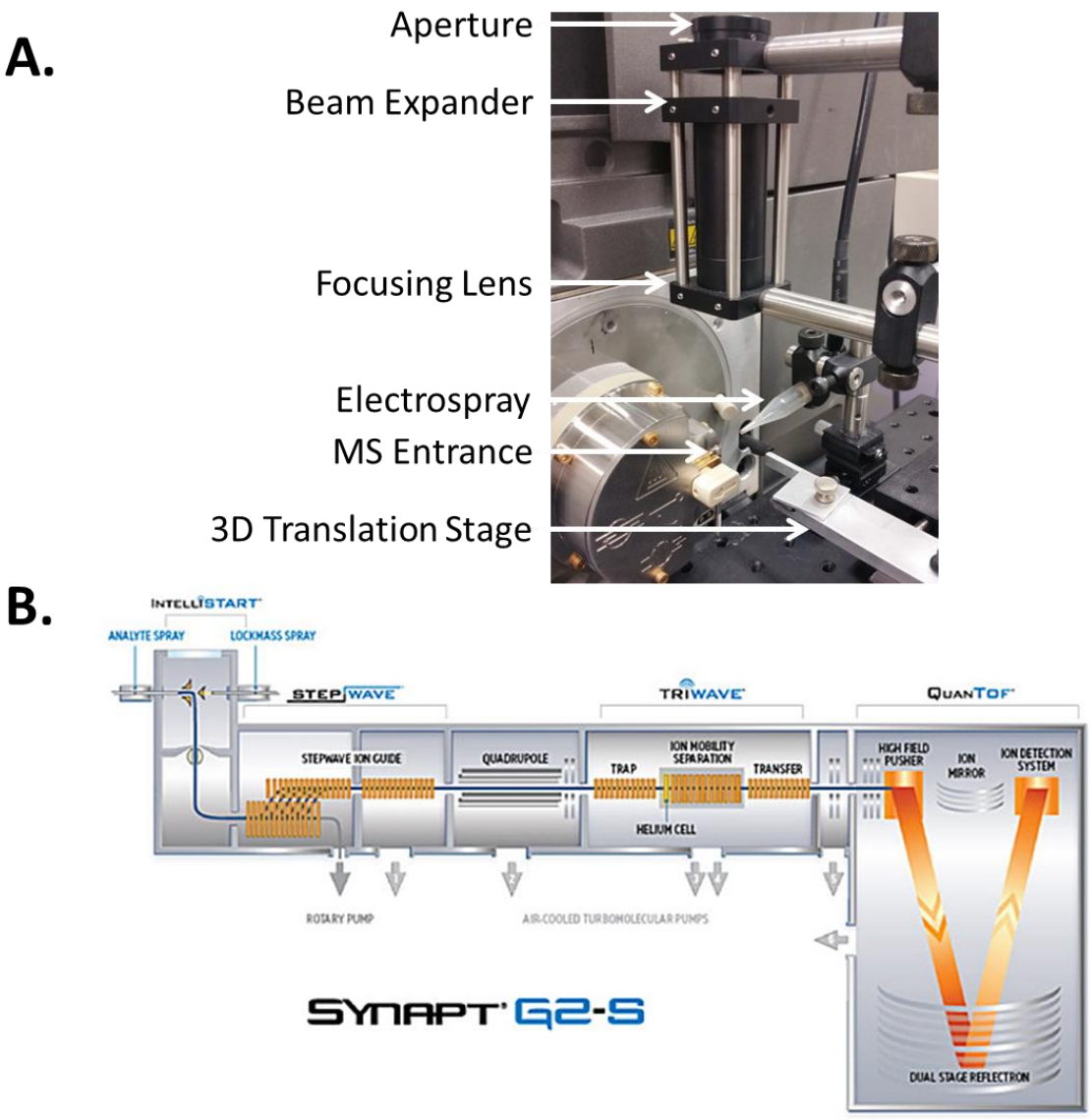

Figure 3. Setup used for ELDI-MSI in this dissertation. **A)** The laser beam is expanded prior to focusing to decrease the spot size at the focal point. The beam is focused to a 50 µm spot size onto a sample slide (not shown) attached to the 3D translation stage. The electrospray capillary is 10 mm from the MS entrance, and both are 8 mm above the sample stage. **B)** Schematic for the Waters Synapt G2-S quadrupole TOF mass spectrometer used for all ELDI-MSI work done in this dissertation.

CHAPTER 2.

MATRIX-FREE ATMOSPHERIC PRESSURE ELECTROSPRAY LASER DESORPTION IONIZATION MASS SPECTROMETRY IMAGING OF PLANT MATERIAL

Patrick A. McVey[1,2,3], Katherine-Jo Galayda[1,2,3], Timothy J. Anderson[4], David P. Baldwin[5], Stanley J. Bajic[1] and R. S. Houk[1,2]

[1]*The Ames Laboratory, Iowa State University, Ames, Iowa, USA*

[2]*Department of Chemistry, Iowa State University, Ames, Iowa, USA*

[3]*These authors contributed equally to this work*

[4]*Exxon Mobil, Houston TX 77520 USA*

[5]*Special Technologies Laboratory, Santa Barbara, California, USA*

Abstract

Electrospray laser desorption ionization (ELDI) is a way to analyze materials without an added matrix coating. Most previous work on plant material has utilized laser ablation electrospray ionization (LAESI) with infrared lasers that are absorbed by the ambient water in the solid sample. Both methods use electrospray ionization post-ablation. In this work, ELDI (which uses an ultraviolet laser) was tested to see if it could achieve better spatial resolution as compared to LAESI. The diffraction-limited spot size is smaller for a shorter wavelength laser, so UV laser could potentially yield better spatial resolution. A frequency tripled Nd:YAG laser at 355 nm which was focused to a 125 µm spot size and used to ablate material directly from leaves. Positive or negative

ions were generated from the ablated material by ESI and measured with an ion mobility time-of-flight mass spectrometer (TOF-MS). No matrix coating was used. Plant leaves readily absorbed the ablation laser at 355 nm. Common metabolites were identified from peony, French marigold, geranium and hosta leaves by accurate mass and tandem MS measurements. Ion maps show spatial variations of several metabolites in different areas of the leaves, especially for variegated plants like hosta. Thus, it can be concluded that plant materials are amenable to ELDI for metabolite identification and spatial profiling.

Introduction

Plant metabolomics is important for many studies, such as a) genotyping and phenotyping, b) comparing transgenic plants with their wild types, c) identifying biomarkers, and d) elucidating bioactive compounds with possible human medicinal uses. Metabolomics is also important in the production of renewable energy sources and breeding of improved food products.[1] Many different analytical methods are used to investigate metabolite composition from a variety of different plant species. These methods commonly include extraction, pre-concentration, and separation steps prior to analysis by mass spectrometry (MS), thus providing detailed and accurate compound identification. However, such pretreatment steps do not provide spatially-resolved information within the plant.

To this end, many recent plant metabolomic analytical developments have focused on techniques that provide fast and sensitive in-situ analysis to generate MS

images of plant materials and structures. Most of these imaging experiments are done at reduced pressure and use an additive or matrix coated onto the plant surface prior to analysis, i.e., matrix-assisted laser desorption ionization (MALDI).[2] An important exception is described by Svatos' group[3] who achieve 10 µm spatial resolution for plants by reduced pressure LDI ablating at 337 nm without an added matrix.

As with most techniques, conventional reduced pressure MS imaging methods that use an applied matrix have both advantages and disadvantages. In general, sensitivity is better when the sample is ionized at reduced pressure, so small laser spots can be used for good spatial resolution. On the opposite side, analytes can become delocalized on the sample surface when the matrix is applied. Furthermore, as the matrix solvent dries, different size matrix crystals may form, affecting the area and amount of sample interrogated by the laser. The need to evacuate the sample also limits the ability to see volatile analytes and complicates time-resolved experiments or measurements on living plants.

In order to circumvent these issues, a number of workers have investigated schemes for laser desorption at atmospheric pressure. Enhancing sensitivity and managing the usual trade-off between sensitivity and spatial resolution are key points for instrumentation or application studies using atmospheric pressure ablation. Many such experiments still use an added matrix coating.[2,4,5] For example, Spengler's group[6] recently reported atmospheric pressure MALDI measurements of many analytes in licorice rhizome using a 337 nm laser and samples coated with 2,5-dihydroxybenzoic acid (DHB). In their instrumentation, the laser is focused coaxially with the ion

extraction capillary, which provides excellent sensitivity and spatial resolution (as good as ~ 5 µm).[7]

An alternative approach is to couple a supplemental ionization source (usually electrospray ionization, ESI) with atmospheric pressure laser desorption or ablation to improve sensitivity. Shiea, Sunner and co-workers initially described electrospray laser desorption ionization (ELDI) experiments that employed a UV laser (337 nm).[8] Shiea's group has continued this work with a UV laser for a variety of sample types and potential applications.[9] Muddiman's group started with an added matrix and a UV laser[10] and has progressed to an infrared (IR) laser with ice matrix.[11] The water in most biological samples serves as a convenient absorbing "matrix" when IR lasers are used, as also shown by Murray.[12,13] Vertes group[14,15] has reported extensive studies on a matrix-free method called laser ablation electrospray ionization mass spectrometry (LAESI-MS). An IR laser at 2.94 µm is used that is readily absorbed by the ambient water in the sample, so no matrix coating is necessary. The laser desorbs analytes which are then ionized by interaction with an ESI plume. A number of analytical development and application studies of LAESI have been reported, including ion mobility,[16,17] measurement of contaminants in food products,[18,19] identification of explosives,[20] and forensic drug analysis.[21] Halls group[22] also employs a 2.94 µm laser and has imaged *Phalaenopsis* leaves and determined major flavonoids, including anthocyanins. Atmospheric pressure photoionization (APPI) can be substituted for ESI for compounds not readily ionized by the latter technique.[23]

The bulk of the previous LAESI or LAAPPI work uses an IR ablation laser, often at wavelength 2.94 µm. Most of these experiments are done with very large spot sizes, e.g., 200 µm.[24] In the present work we show that ELDI using a UV laser (355 nm) is comparable to LAESI, at least for plant samples. A UV laser can be focused to a smaller diffraction limited spot size than an IR laser.[25,26] Thus, the spatial resolution is potentially better with a UV laser. Of course utilization of smaller laser spots generally means less analyte is desorbed, so the instrument sensitivity and background also affect the achievable spatial resolution.

Of the other groups that have investigated ELDI or LAESI with a UV laser at atmospheric pressure,[8,27] there are no reports of imaging of metabolites in plants, the closest materials being fungus slices ablated at 337 nm.[28] In related papers specifically involving laser ablation of plants, Levis' group uses LAESI with an IR (800 nm wavelength) fs laser,[29,30] and Harada et al. report analysis of ginger rhizome at 355 nm, but without supplementary ESI.[31] Sunner's group recently reports laser ablation and solvent capture by aspiration (LASCA) for plants with ablation at 2.94 µm.[32]

Thus, it appears that the combination of UV lasers with additional ESI and no added matrix has not been extensively investigated specifically for MS analysis and mass spectrometry imaging (MSI) of plants. No such papers are listed in the recent reviews by Bjarnholt et al.,[4] Spengler[33] and Muddiman's group.[34] For that matter, MSI by any means has been used much less extensively for plants than for animal or human medical applications, although interest in MS imaging of plants is growing rapidly.[33] In the

present work, instrumentation and initial results, including images, are described for atmospheric pressure ELDI on peony, French marigold, geranium and hosta leaves.

Experimental

Mass spectrometer

A Waters Synapt G2-S quadrupole time-of-flight mass spectrometer was used in these experiments. Ions were collected with the standard ESI source enclosure removed. The Synapt fluidic systems and high voltage connections were bypassed, utilizing a specialized adapter supplied by Waters. No other modifications were made to the mass spectrometer. Mass spectra were recorded from either m/z 100 to 1200 or m/z 100 to 2000. The TOF mass analyzer was operated in "sensitivity" mode, i.e., the ions made one pass through only the main reflectron. The mass resolution was m/Δm 10,000 (FWHM). In tandem MS experiments the quadrupole resolution was Δm/z ~ 3 Da, and the collision energy was nominally 10 eV. Data were acquired and analyzed using Waters MassLynx V4.1 (SCN851) software.

Laser and ion source

Samples were mounted on glass microscope slides with double-stick tape and trimmed to the shape of the slide, if necessary. No matrix or additional treatment was applied. The samples were placed 8 mm below the ESI axis (Fig.1) and attached to a computer controlled xyz-translation stage (Z825B, Thorlabs, Inc. Newton, NJ). The sample slide was translated at a rate of 0.4 mm/s during ablation to provide spatial

resolution and to ensure that a fresh sample area was interrogated during the experiment

The leaves were irradiated normal to the sample surface with the laser beam axis approximately 2 mm downstream from the ESI capillary tip (Fig. 1). The third harmonic (355 nm) output from a Nd:YAG laser (ULTRA, Big Sky Laser Tech, Inc., Bozeman, MT) was focused onto the sample by a single fused-silica plano-convex focusing lens (focal length 75 mm). The nominal spot size was ~125 µm at the sample. The laser was operated at 10 Hz, 5 ns pulse width, with a nominal energy of 250 µJ/pulse measured before the focusing lens.

The tip of the ESI capillary was positioned on the ion extraction axis approximately 10 mm from the sample cone inlet of the mass spectrometer (Fig. 1). A mixture of methanol and water (1:1 v/v) was pumped through a 53 µm i.d. polyimide-coated capillary at 0.4 µl/min by a syringe pump (Model 22, Harvard Apparatus, South Natick, MA). In positive ion mode, a 0.1% solution of formic acid (purity ≥ 99.5%, Fischer Scientific) was sprayed by the ESI source. In negative ion mode, 0.1% ammonium hydroxide (purity ≥ 99.99%, Sigma-Aldrich) was sprayed. Additionally, leucine-enkephalin (0.1 ppm, Waters) was added to the electrospray solutions and used as the lockspray mass calibrant. The ESI voltage was + 2.3 kV for positive ions or -2.3 kV for negative ions. The inlet sample cone completed the electrospray circuit and was kept at 100 ^{o}C with a nitrogen curtain gas (~ 1 l/hr, Waters default value).

Data Handling

Mass spectra and ion maps were generated from total ion chromatograms (TICs) provided by Waters MassLynx software. For images the *.raw data files were first converted into mzML files using the Proteowizard Mass ConverterTool .[35] The mzML files were then converted into imzML files using imzMLConverter.[36] The imzML files were viewed in DatacubeExplorer.[37] The black and white images from DatacubeExplorer were interpolated with cubic-spline smoothing and converted to false-color images using GIMP 2.8.

Safety Considerations

Laser safety goggles specifically for UV beams were used whenever the beam was exposed. Care was taken to avoid contact with the ESI spray tip.

Results and Discussion

The set-up for the experiments discussed here is shown in Figure 1. The distances depicted in the figure represent the optimized positions for maximum signal when analyzing plant material. With the ESI voltage off, the mass spectrometer observed few or no ions from laser ablation or desorption alone, as seen previously by Shiea et al.[8] With the ESI voltage on and the laser beam blocked, only background ions from the spray solution were observed, as shown by the left section of the total ion chromatogram in Fig 2a. These ions include the lockspray-mass calibrant at m/z 556.27, protonated leucine-enkephalin $[M+H]^+$. This observation indicates that no desorption

ESI (DESI) effect[38,39] is produced from the original plant surface with the ions used in our usual setup. With the electrospray and laser both active the total ion signal is much higher than with ESI alone (Fig. 2a right), and many peaks are seen from the plant sample (Fig. 2b).

Varying the distance from the sample surface to the sample-cone axis between 6 to 10 mm, while also refocusing the laser, did not have a large effect on the ion signal intensity. Thus, the sample itself does not have to be perfectly flat. At closer distances (~ 4 to 6 mm) the ESI signal decreased, likely due to the distortion of the electric field because of the presence of the nonconductive microscope slide and holder. When the sample was closer than 4 mm from the ESI - sample cone axis, a DESI effect was observed, i.e., ions were seen from the sample without the laser.

A typical freshly ablated trench is presented in Figure 3. The sides of the trench are clean with little or no sample damage outside the 125 µm laser spot size. In the images in a subsequent figure, photos of the ablated sample appear to show more damage and wider trenches, but these latter photos were taken several hours after the actual experiment, and the sample leaf dried and cracked along the ablated trenches in the interim. Figure 3 also shows that, with the sample moving at 0.4 mm/s, the trench does not penetrate the leaf completely. Thus, the adhesive used to mount the sample is not desorbed and ionized.

Peony

Figure 2 illustrates a typical acquisition for a peony leaf in positive-ion mode. Similar results were obtained for other plants and in negative ion mode. Changes in the TIC are shown as a function of time. The length of time for a single acquisition was two minutes. A single acquisition here corresponds to a single ablated line across the surface of the sample, resulting in a trench like that shown in Fig. 3 approximately 24 mm long.

In the TIC shown in Figure 2, when the laser starts ablating material from the sample at 1 min; the TIC greatly increases. Each point in the TIC in the 2nd minute corresponds to a complete, spatially-resolved mass spectrum from a particular location on the leaf generated by ELDI.

A representative positive-ion mass spectrum (integrated from one laser ablation trench, 50 points) from the peony leaf is shown in Fig. 2b. The most abundant ion signals are observed at m/z 287.0535 and 449.1084. These peaks correspond to the singly-charged flavonoids kaempferol and kaempferol-3-glucoside, respectively (for structures of these metabolites, refer to S1).[40] Ion signals were measured up to approximately m/z 950 for the peony in positive ion mode. The identities of these higher mass ions are not clear; they may originate from the peony cuticle, which is harder and thicker than those of the other plants investigated in this study. Low abundance doubly-charged ions were observed at m/z 244.0344, 460.0985, and 692.1361 from this sample. No other multiply charged ions were detected.

Some of the more abundant peaks observed from the peony and their suggested assignments are listed in Table 1. Peak assignments for the other plant samples are also given there.[41,42] Tandem MS measurements in both positive and negative ion mode were used to help identify many analyte compounds.

French Marigold

In order to assess the effectiveness of studying metabolic processes in plant materials by ELDI, the technique was applied to several common plants that have been studied previously by LAESI. A positive-ion mass spectrum from a French marigold leaf is shown in Figure 4. A number of high abundance metabolites are observed. These include peaks at m/z 287.0609, 303.0548, 433.1310, 633.1613, and 649.1422. These ion signals mainly correspond to the singly-charged flavonoid and flavonoid glucoside species of kaempferol and quercetin.

Positive and negative ion MS and tandem MS spectra were collected from the marigold leaves. Below m/z 600, all but one compound from our French marigold leaves were reported in a previous analysis performed by LAESI.[14] In the present work, we observed more peaks above m/z 600, for several possible reasons. These are not exactly the same marigold samples. They were not grown in the same location, for example. The diversity of metabolites in a particular plant genus depends on a number of factors (e.g., species, environment, and harvest time),[41,42] which also may account for some of the differences in the observed metabolites.

Some of the more abundant peaks and their suggested assignments are listed in Table 1. Since the main goal of this work is to assess this UV ablation technique for studying plant metabolites, comprehensive assignments of all peaks was not undertaken. The assignments listed in Table 1 are based on a combination of exact mass measurements, database search results, tandem MS spectral information, and comparison with previous results from the literature.

Geranium

In order to assess the capability for imaging metabolites by atmospheric pressure ELDI, several variegated plants were investigated. Figure 5 shows the integrated mass spectrum acquired from the leaf of a geranium plant. This leaf had both green and purple regions. The mass spectrum in Fig. 5 is an average of mass spectra collected from one track across the entire length of the leaf encompassing all the hues found. The three most abundant ion signals are at m/z 153.0410, 287.0535, and 303.0532. The suggested assignments for these mass peaks are cysteine + Na^+, kaempferol + H^+, and quercetin + H^+, respectively. Some of the more intense peaks from both positive and negative ion acquisitions from the geranium and their suggested assignments are listed in Table 1.

The inset in Figure 5 shows two groups of cluster species. The first group of clusters from m/z ~ 900 through 1000, are separated by Δm/z 16 u and are likely from lipid-type moieties and similar isomers. The second group of clusters from m/z ~ 1400 through 1750 are 76 u apart, and have been identified in previous work[14] as

predominantly doubly-charged clusters of geranial oil, which is commonly found in geraniums. These clusters are believed to be in the plant and not artifacts of the ionization process. Other low abundance doubly-charged ions are also observed at m/z 461, 477, 484, and 492.

Tandem and Ion Mobility MS

Typical tandem MS spectra are given in Fig. 6a and 6b for two abundant positive ions from geranium: glucose + Na^+ (m/z 203) and kaempferol + H^+ (m/z 287). An IMS plot of drift time vs. m/z is shown for geranium positive ions in Fig 6c. Doubly charged (2+) ions are readily distinguished from 1+ ions, as seen using LAESI ionization by Vertes' group,[17] and the expected broad stripes of different slopes corresponding to different compound classes are observed.[43] A number of isobars or near-isobars in have resolvable drift times.[17]

Hosta

Spatial images were generated for the various plant samples discussed above. An example of these MSI results is described below for a hosta leaf sample, which has variegated leaves with separate dark green and yellow sections. Figure 7 shows an integrated mass spectrum for one ablation track in the hosta leaf. Some of the more abundant peaks and their suggested assignments are listed in Table 1.

A post-ablation photograph and false-color ion maps for a selected portion of hosta leaf are shown in Figure 8. The broad, fuzzy horizontal lines observed in the photo

(Fig. 8a) are the tracks left behind after the ablated leaf has been allowed to dry ~ 8 hours. During an actual experiment the tracks are much sharper, like the one shown in Fig. 3. For the image shown in Figure 8 there are 11 ablation tracks 125 µm wide x 300 µm apart.

The ion-map for m/z 561.171 (Fig. 8b) shows that this unknown compound is concentrated in the veins and in the dark green portion of the hosta leaf. Conversely, the map for m/z 663.126 (kaempferol 5-methyl ether 3-galactoside-4'-glucoside + K^+) (Fig. 8c) shows that the concentrations of this metabolite are low in the vein areas of this leaf. The ion map for m/z 175.117 (arginine + H^+) (Fig. 8d) shows that this metabolite is mainly in the yellow portion of the leaf. While m/z 381.078 (sucrose + K^+) (Fig. 8e) is found throughout the leaf, it is much more abundant in the greener portions.

Conclusions

This work demonstrates the potential value of atmospheric-pressure ELDI for the analysis of metabolites in plants. For the analysis of lower abundance compounds further developments are desired to improve sensitivity of the method. By increasing the sensitivity, the laser spot size can be decreased for improved spatial resolution, allowing for analysis of compounds at various growth or uptake stages in specific parts of the plant. Recent work with this device has generated reasonable spectra with spot sizes of 50 µm (data not shown).

This technique requires very little sample preparation and does not need an applied matrix to analyze plant materials. The UV laser penetrates a few micrometers

(~ 30 µm) into the sample, enough to desorb a variety of analytes. The experiment is not restricted to green plants; woods, nuts and corn kernels ablate readily and produce good spectra using this laser. Since the plant sample is kept at atmospheric pressure, time-resolved measurements on living plants are possible. These and other studies are underway in our laboratory.

Acknowledgments

This work was supported by the US Department of Energy (DOE), Office of Basic Energy Sciences, Division of Chemical Sciences, Geosciences, and Biosciences. The Ames Laboratory is operated by Iowa State University under DOE contract DE-AC02-07CH11358. The authors thank Young-Jin Lee for providing the laser and for many helpful suggestions. The authors would also like to thank Akos Vertes for early advice and demonstrations of the LAESI technique.

References

1) R. D. Hall. Plant metabolomics: from holistic hope, to hype, to hot topic. New Phytologist. 2006, 169, 453.

2) J. Grassl, N. L. Taylor, A. H. Millar. Matrix-assisted laser desorption/ionization mass spectrometry imaging and its development for plant protein imaging. *Plant Methods* **2011**, *7*, 21 (online content).

3) D. Holscher, R. Shroff, K. Knop, M. Gottschaldt, A. Grecelius, B. Schneider, D. G. Heckel, U. S. Schubery, A. Scatos, Matrix-free UV-laser desorption/ionization (LDI) mass spectrometric imaging at the single cell level: distribution of secondary metabolites of Arabidopsis thaliana and Hypericum species. Plant. J. 2009, 60, 907.

4) N. Bjarnholt, B. Li, J. D'Alviseb, C. Janfelt. Mass spectrometry imaging of plant metabolites – principles and possibilities. Nat. Prod. Rep., 2014, 31, 818.

5) D. C. Perdian, G. M. Schieffer, R. S. Houk, Atmospheric pressure laser desorption ionization of plant metabolites and plant tissues using colloidal graphite, Rapid Commun. Mass Spectrom. 2010, 24, 397.

6) B. Li, D. R. Bhandari, C. Janfelt, A, Roempp, B. Spengler, Natural products in Glycyrrhiza glabra (licorice) rhizome imaged at the celleular level by atmospheric pressure matrix assisted laser desorption/ionization tandem mass spectrometry imaging, Plant. J. 2014, 80, 161.

7) M. Koestler, D. Kirsch, A. Hester, S. Guenther, B. Spengler, A high-resolution scanning microprobe matrix-assisted laser desorption/ionization mass spectrometer for imaging analysis on an ion trap/Fourier transform ion cyclotron resonance mass spectrometer, Rapid Commun. Mass Spectrom. 2008, 22, 3275.

8) J. Shiea, M. Z. Huang, H. J. H. Su, C. Y. Lee, C. H. Yuan, I. Beech, J. Sunner, Electrospray-assisted laser desorption ionization mass spectrometry for direct ambient analysis of solids, Rapid Commun. Mass Spectrom. 2005, 19, 3701.

9) Y.-Y. Kao, S.-C. Cheng, C.-N. Cheng, J. Shiea, H.-O Ho, Detection of trace ink compounds in erased handwritings using electrospray assisted laser desorption ionization mass spectrometry, J. Mass Spectrom. 2014, 49, 445.

10) J. S. Sampson, A. M. Hawkridge, D. C. Muddiman, Generation and detection of multiply-charged peptides and proteins by matrix-assisted laser desorption electrospray ionization (MALDESI) Fourier transform ion cyclotron mass spectrometry, J. Amer. Soc. Mass Spectrom. 2006, 17, 1712.

11) C. Robichaud, J. A. Barry, D. C. Muddiman, IR-MALDESI mass spectrometry imaging of biological tissue sections using ice as a matrix, J. Amer. Soc. Mass Spectrom. 2014, 25, 319.

12) Y. H. Rezenom, J. Dong, K. K. Murray, Infrared laser-assisted desorption electrospray ionization mass spectrometry, Analyst 2008, 133, 226.

13) J. S. Sampson, K. K. Murray, D. C. Muddiman, Intact and top-down characterization of biomolecules and direct analysis using infrared matrix-assisted laser desorption electrospray ionization coupled to FT-ICR mass spectrometry, J. Amer. Soc. Mass Spectrom. 2009, 20, 667.

14) P. Nemes, A. Vertes. Laser ablation electrospray ionization for atmospheric pressure, in vivo, and imaging mass spectrometry. Anal. Chem. 2007, 79, 8098.

15) A. Vertes, P. Nemes, B. Shrestha, A. A. Barton, Z. Chen, Y. Li. Molecular imaging by mid-IR laser ablation mass spectrometry. Appl. Phys. A 2008, 93, 885.

16) B. Shrestha, A. Vertes. High-throughput cell and tissue analysis and enhanced molecular coverage by laser ablation electrospray ionization mass spectrometry using ion mobility separation. Anal. Chem. 2014, 86, 4308.

17) H. Li, B. K. Smith, L. Mark, P. Nemes, J. Nazarian, A. Vertes, Ambient molecular imaging by laser ablation electrospray ionization mass spectrometry with ion mobility separation, Int. J. Mass Spectrom. 2015, 375, 681.

18) J. Liu, B. Qui, H. Luo. Fingerprinting of yogurt products by laser desorption spray post-ionization mass spectrometry. Rapid Commun. Mass Spectrom. 2010, 24, 1365.

19) M. W. F. Nielen, T. A. van Beek. Macroscopic and microscopic spatially-resolved analysis of food contaminants and constituents using laser-ablation electrospray ionization mass spectrometry imaging. Anal. Bioanal. Chem. 2014, 406, 6805.

20) J. J. Brady, E. J. Judge, R. J. Levis. Identification of explosives and explosive formulations using laser electrospray mass spectrometry. Rapid Commun. Mass Spectrom. 2010, 24, 1659.

21) R. E. Deimler, T. T. Razunguzwa, B. R. Reschke, C. M. Walsh, M. J. Powell, G. P. Jackson. Direct analysis of drugs in forensic applications using laser ablation electrospray ionization-tandem mass spectrometry (LAESI-MS/MS). Anal. Methods, 2014, 6, 4810.

22) Etalo, D. W., De Vos, R. C., Joosten, M. H., & Hall, R. D. Spatially resolved plant metabolomics: some potentials and limitations of laser-ablation electrospray ionization mass spectrometry metabolite imaging. Plant physiology. 2015, 169(3): 1424-1435.

23) A. Vaikkinen, B. Shrestha, J. Koivisto, R. Kostiainen, A. Vertes, T. J. Kauppila. Laser Ablation Atmospheric Pressure Photoionization Mass Spectrometry Imaging of Phytochemicals from Sage Leaves. Rapid Commun. Mass Spectrom. 2014, 28, 2490.

24) D. W. Etalo, R. C. H. De Vos, M. H. A. J. Joosten, R. D. Hall. Spatially-resolved plant metabolomics: some potentials and limitations of laser ablation electrospray ionization mass spectrometry metabolite imaging. Plant Physiol. Preview 2015, doi: 10.1104/pp.15.01176.

25) A. Roempp, B. Spengler. Mass spectrometry imaging with high resolution in mass and space. Histochem. Cell Biol. 2013, 139(6), 759.

26) W. T. Silfvast, Laser Fundamentals, 2nd ed., Cambridge, University Press, 2004, p. 419.

27) M.-Z. Huang, H.-J. Hsu, C.-I. Wu, S.-Y. Lin, Y.-L. Ma, T.-L. Cheng, J. Shiea, Characterization of the chemical components on the surface of different solids with electrospray-assisted laser desorption ionization mass spectrometry. Rapid Commun. Mass Spectrom. 2007, 21, 1767

28) M.-Z. Huang, S.-C. Cheng, S.-S. Jiang, C.-C. Chou, C.-N. Cheng, J. Shiea, I. A Popov, E. N. Nikolaev, Ambient molecular imaging of dry fungus surface by electrospray laser desorption ionization mass spectrometry, Int. J. Mass Spectrom. 2012, 325-327, 172.

29) E. A. Judge, J. J. Brady, P. E. Barbano, R. J. Levis, Nonresonant femtosecond laser vaporization with electrospray postionization for ex vivo plant tissue typing using compressive linear classification, Anal. Chem. 2011, 83, 2145.

30) P. M. Flanigan IV, L. L. Radell, J. J. Brady, R. J. Levis, Differentiation of eight phenotypes and discovery of potential biomarkers for a single plant organ class using laser electrospray mass spectrometry and multivariate statistical analysis, Anal. Chem. 2012, 84, 6225.

31) T. Harada, A. Yuba-Kubo, Y. Sugiura, N. Zaima, T. Hayasdaka, N. Goto-Inoue, M. Wakui, M. Suematsu, K. Takeshita, K. Ogawa, Y. Yoshida, M. Setou, Visualization of volatile substances in different organelles with an atmospheric-pressure mass microscope, Anal. Chem. 2009, 81, 9153.

32) J. I. Brauer, I. B. Beech, J. Sunner, Mass spectrometric imaging using laser ablation and solvent capture by aspiration (LASCA), J. Amer. Soc. Mass Spectrom. 2015, 26, 1538.

33) B. Spengler, Mass spectrometry imaging of biomolecular information, Anal. Chem. 2014, 87, 64.

34) G. Robichaud, J. A. Barry, D. C. Muddiman, Atmospheric pressure mass spectrometry imaging, Encyclopedia of Analytical Chemistry, Wiley, 2014, p. 1. DOI:10.1002/9780470027318.a9399

35) M. C. Chambers, B. MacLean, R. Burke, D. Amode, D. L. Ruderman, S. Neumann, L. Gatto, B. Fischer, B. Pratt, J. Egertson, K. Hoff, D. Kessner, N. Tasman, N. Shulman, B. Frewen, T. A. Baker, M.-Y. Brusniak, C. Paulse, D. Creasy, L. Flashner, K. Kani, C.

Moulding, S. L. Seymour, L. M. Nuwaysir, B. Lefebvre, F. Kuhlmann, J. Roark, P. Rainer, S. Detlev, T. Hemenway, A. Huhmer, J. Langridge, B. Connolly, T. Chadick, K. Holly, J. Eckels, E. W. Deutsch, R. L. Moritz, J. E. Katz, D. B. Agus, M. MacCoss, D. L. Tabb, P. Mallick, A cross-platform toolkit for mass spectrometry and proteomics. Nature Biotechnology 2012, 30, 918.

36) I. M. Race, I. B. Styles, J. Bunch. Inclusive sharing of mass spectrometry imaging data requires a converter for all. J. Proteomics 2012, 75, 5111.

37) I. Klinkert, K. Chughtai, S.R. Ellis, R.M.A. Heeren. Methods for full resolution data exploration and visualization for large 2D and 3D mass spectrometry imaging datasets. Int. J. Mass Spectrom. 2014, 362, 40.

38) F. M. Green, T. L. Salter, I. S. Gilmore, P. Stokes and G. O'Connor. The effect of electrospray solvent composition on desorption electrospray ionisation (DESI) efficiency and spatial resolution. Analyst, 2010, 135, 731.

39) D. R. Ifa, C. Wu, Z. Ouyang, R. G. Cooks. Desorption electrospray ionization and other ambient ionization methods: current progress and preview. Analyst 2010, 135, 669.

40) F. Sanchez-Rabaneda, O. Jauregui, R. M. Lamuela-Raventos, F. Viladomat, J. Bastida, C. Codina. Qualitative analysis of phenolic compounds in apple pomace using liquid chromatography coupled to mass spectrometry in tandem mode. Rapid. Commun. Mass Spectrom. 2004, 18, 553.

41) E. Urbanczyk-Wochniak, C. Baxter, A. Kolbe, J. Kopka, L. J. Sweetlove, A. R. Fernie. Profiling of diurnal patterns of metabolite and transcript abundance in potato (Solanum tuberosum) leaves. Planta 2005, 221, 891.

42) H. K. Kim, R. Verpoorte. Sample preparation for plant metabolomics. Phytochem. Anal. 2010, 21, 4.

43) J. C. May, J. A. McLean, The conformational landscape of biomolecules in ion mobility – mass spectrometry, in Ion mobility mass spectrometry theory and applications, C. L. Wilkins, S. Trimpin, Eds., CRC Press, Boca Raton, FL, Chap. 16 Figs. 16.4 and 16.5

Table 1. Metabolites identified in peony, French marigold, geranium, and hosta by ELDI.

Plant	Suggested Assignment	Measured Mass (Da)	Accurate Mass (Da)	Δ ppm	Adduct	Measured Product Ions
Peony	Kaempferol	287.0535	287.0555	-6.97	$[M+H]^+$	258, 213, 165, 153
	Isorhamnetin	317.062	317.0661	-12.93	$[M+H]^+$	
	Kaempferol-3-glucoside	449.1084	449.109	-1.34	$[M+H]^+$	287
	Kaempferol-7-glucoside	471.0906	471.0903	0.64	$[M+Na]^+$	287
	Quercetin 3-O-glucoside or Quercetin 7-O-glucoside	487.0751	487.0853	-20.94	$[M+Na]^+$	
	p-Hydrobenzoic acid	137.0245	137.0239	4.38	$[M-H]^-$	
	Kaempferol 3-O-arabinoside	417.0837	417.0822	3.60	$[M-H]^-$	
	Luteolin 7-O-glucoside	447.0995	447.0927	15.21	$[M-H]^-$	285
	Kaempferol 3-O-galloyl glucoside	599.1116	599.1037	13.19	$[M-H]^-$	
Marigold	Kaempferol	287.0609	287.0555	18.81	$[M+H]^+$	258, 213, 165, 153
	Quercetin	303.0548	303.0504	14.52	$[M+H]^+$	285, 257, 229, 165, 153
	Kaempferol-3-rhamnoside	433.1183	433.1134	11.31	$[M+H]^+$	287
	Kaempferol-3-glucoside or quercetin-3-rhamnoside	449.1084	449.109	-1.34	$[M+H]^+$	303, 287
	Quercetin 3-O-glucoside or Quercetin 7-O-glucoside	487.0891	487.0853	7.80	$[M+Na]^+$	325, 303, 287, 177, 147
	Kaempferol 3-O-arabinoside	603.1431			$[M+H]^+$	
	Quercetin 3-O-galloylglucoside	617.1606			$[M+H]^+$	325, 287, 147
	Quercetin 3-O-arabinoside	433.0787	433.0771	3.69	$[M-H]^-$	
	Luteolin 7-O-glucoside	447.0995	447.0927	15.21	$[M-H]^-$	285

Table 1. Continued.

Plant	Suggested Assignment	Measured Mass	Accurate Mass	Δ ppm	Adduct	Measured Product Ions
Marigold (cont.)	Quercetin 3-O-glucoside or Quercetin 7-O-glucoside	463.0906	463.0877	6.26	$[M-H]^-$	301
	Kaempferol 3-O-glucoside-7-O-rhamnoside	593.16	593.1507	15.68	$[M-H]^-$	447
	Kaempferol 3,7-di-O-glucoside	609.1509	609.1456	8.70	$[M-H]^-$	447, 285
	Quercetin 3,7-di-O-glucoside	625.1469	625.1405	10.24	$[M-H]^-$	
Geranium	Glucose	203.0602	203.053	35.46	$[M+Na]^+$	
	Kaempferol	287.0535	287.0555	-6.97	$[M+H]^+$	
	Quercetin	303.0532	303.0504	9.24	$[M+H]^+$	
	Quercetin-O-α-L-arabinofuranoside	435.0921	435.0927	-1.38	$[M+H]^+$	
	Quercetin-O-glucoside	465.1059	465.1033	5.59	$[M+H]^+$	
	Kaempferol arabinoside	417.0863	417.0822	9.83	$[M-H]^-$	285
	Quercetin arabinoside	433.0812	433.0771	9.47	$[M-H]^-$	301
	Kaempferol 3-glucoside	447.0927	447.0927	0.00	$[M-H]^-$	
	Quercetin 3-glucoside	463.0929	463.0877	11.23	$[M-H]^-$	301
	Myricetin glycoside	479.0875	479.0826	10.23	$[M-H]^-$	317
	Kaempferol galloylgalactoside or Kaempferol galloylglucoside	599.1019	599.1037	-3.00	$[M-H]^-$	
	Quercetin 3-(2-galloyl)galactoside or Quercetin 3-(2-galloyl)glucoside	615.1069	615.0986	13.49	$[M-H]^-$	
	Trigalloyl quinic acid	647.094	647.0884	8.65	$[M-H]^-$	
	Hexagalloylglucose	1091.131	1091.1213	8.98	$[M-H]^-$	
	Heptagalloylglucose	1243.14	1243.1323	6.19	$[M-H]^-$	
	Octagalloylglucose	1395.137	1395.1432	-4.73	$[M-H]^-$	*
	Nonagalloylglucose	1547.157	1547.1542	1.55	$[M-H]^-$	*
	Decagalloylglucose	1699.159	1699.1652	-3.83	$[M-H]^-$	*

Table 1. Continued.

Plant	Suggested Assignment	Measured Mass	Accurate Mass	Δ ppm	Adduct	Measured Product Ions
Hosta	Arginine	175.1165	175.1195	-17.13	$[M+H]^+$	157, 139
	Sucrose	381.0782	381.0799	-4.46	$[M+K]^+$	
	Kaempferol 5-methyl ether 3-galactoside-4'-glucoside	663.1257	663.1327	-10.56	$[M+K]^+$	
	Kaempferol 7-O-(6-trans-caffeoyl)-beta-glucopyranosyl-(1->3)-alpha-rhamnopyranoside-3-O-beta-glucopyranoside	957.2174	957.2067	11.18	$[M+K]^+$	671. 525,509, 363, 287
	Citric Acid	191.0194	191.0197	-1.57	$[M-H]^-$	
	Sucrose	341.1103	341.1089	4.10	$[M-H]^-$	179, 161, 149
	Kaempferol diglucoside	609.1463	609.1456	1.15	$[M-H]^-$	489, 447, 429, 285
	Kaempferol 3-O-diglucoside-7-O-glucoside	771.1934	771.1983	-6.35	$[M-H]^-$	609, 591, 429, 285

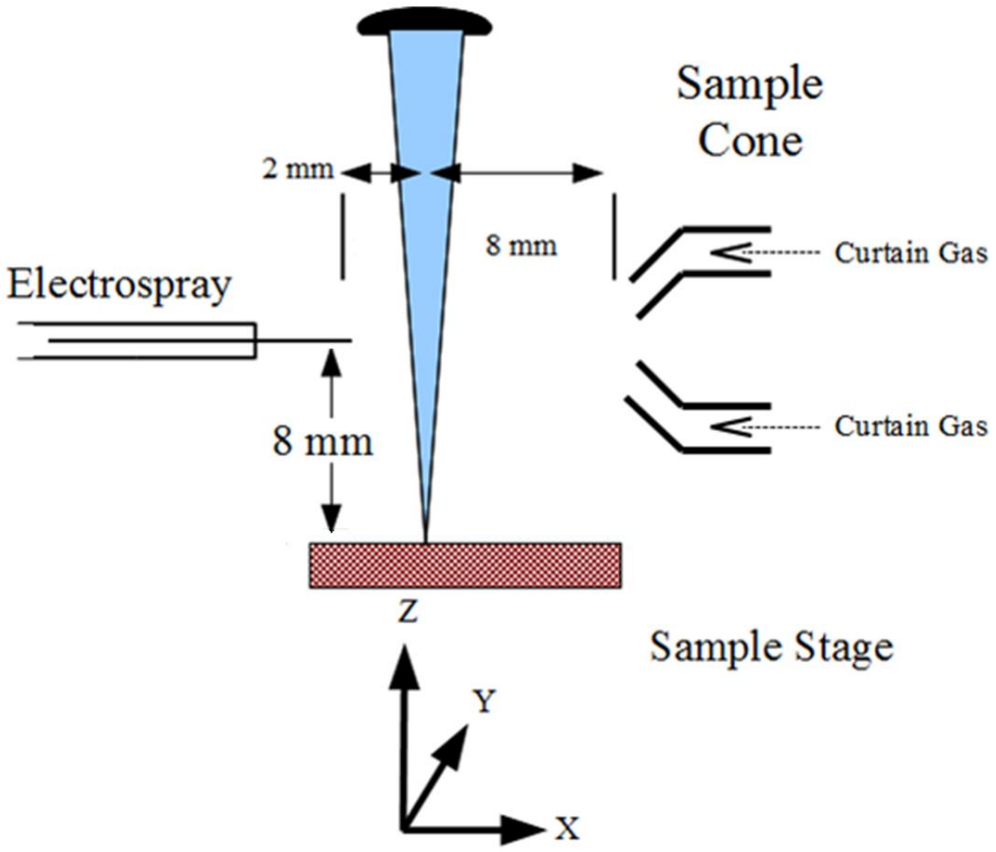

Figure 1. Experimental setup for ELDI. The dimensions noted in the figure produced optimal signal intensities. The sample stage was a glass microscope slide with the plant sample taped to the top side.

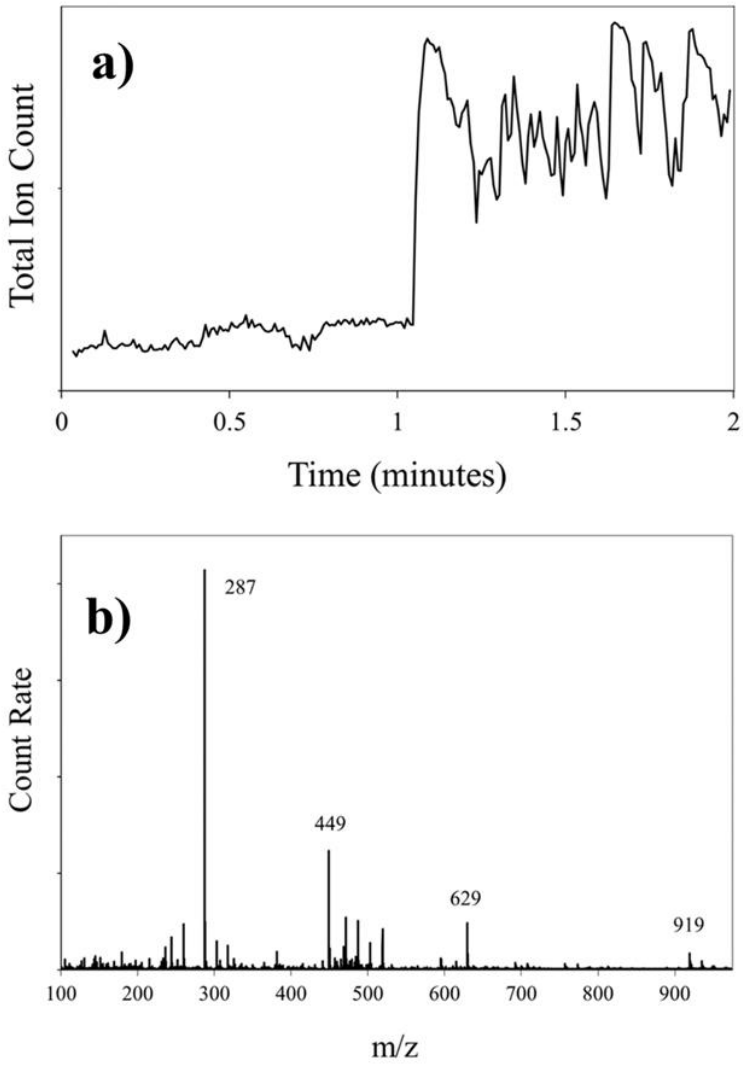

Figure 2. Typical chromatogram and spectra for an ELDI acquisition. **A)** Typical total ion chromatogram recorded from one ablation track during ambient-pressure ELDI acquisition. During the first minute of the acquisition, the laser is blocked and the TIC is solely due the ions generated from the electrospray. The laser is unblocked during the second minute of the acquisition and the TIC is a combination of ions from the ESI and the ions produced by electrospray ionization of ablated material. **B)** Integrated positive ion mass spectrum obtained from a peony leaf acquired by atmospheric-pressure ELDI. This spectrum was integrated from the TIC in the latter part of Fig. 4a. The ESI background (time < 1 min) has been subtracted from the ELDI spectrum (time > 1 min).

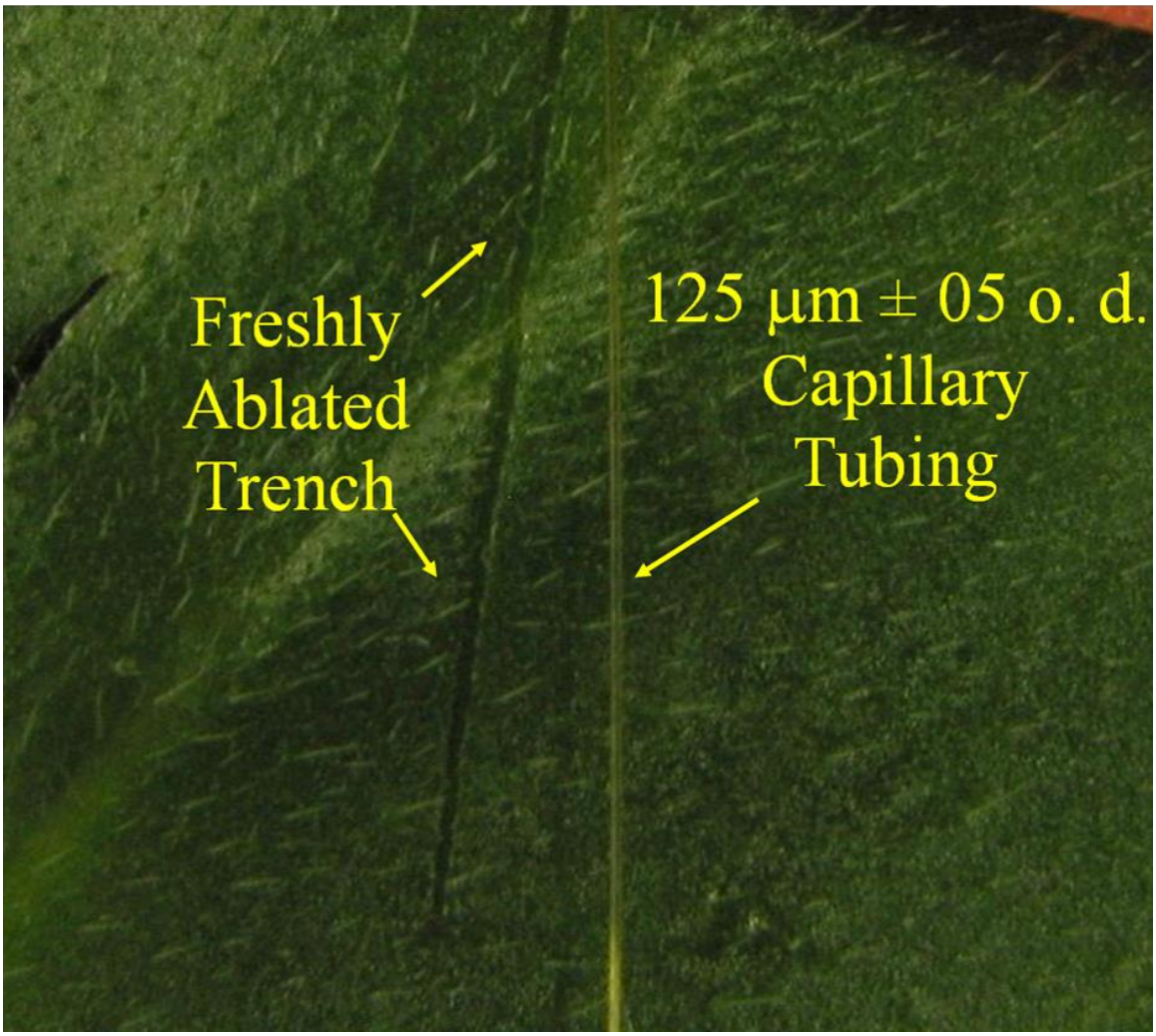

Figure 3. Photo showing nominal size of ablation trench produced on a translated French marigold leaf by the UV laser. This picture was taken a few seconds after an ablation run, before the sample dried and cracked.

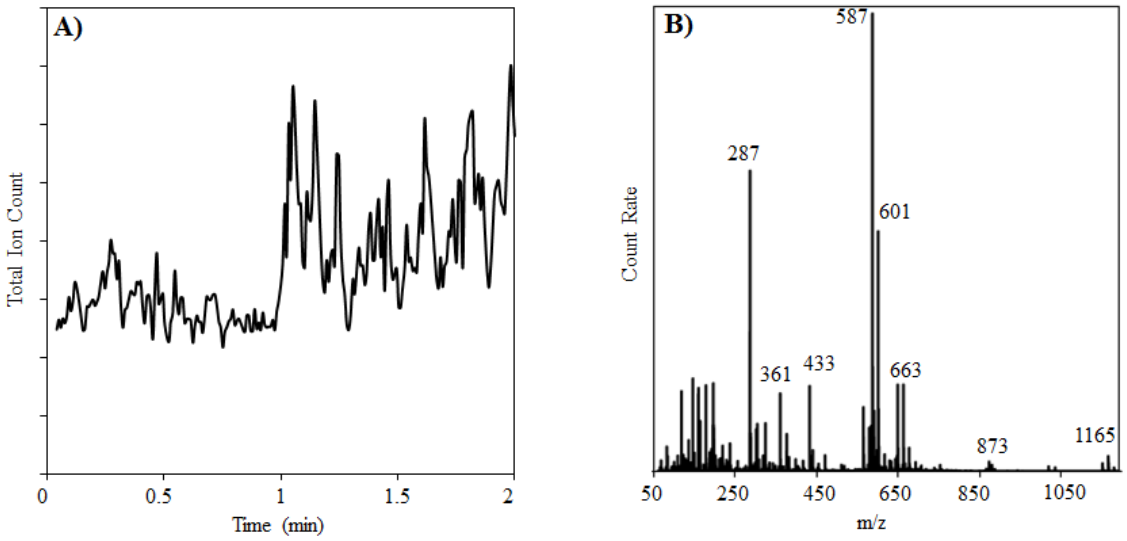

Figure 4. Integrated positive ion mass spectrum obtained from one ablation track in a French marigold leaf acquired by atmospheric-pressure ELDI. The inset (~ 90x zoom) shows a range of clusters at higher m/z. The ESI background has been subtracted from this ELDI spectrum.

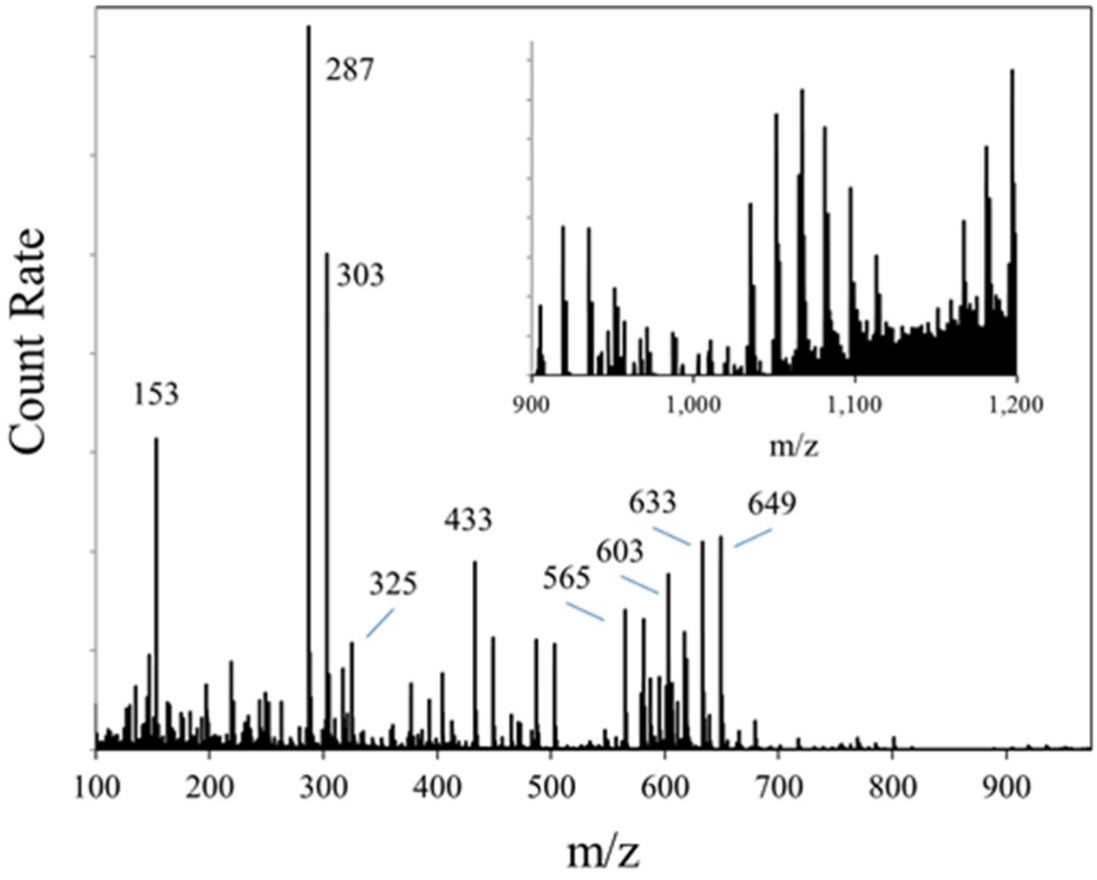

Figure 5. Integrated positive-ion mass spectrum obtained from a geranium leaf acquired by atmospheric-pressure ELDI. The inset (~28x zoom) shows a range of cluster peaks at higher m/z. The electrospray background has been subtracted from this ELDI spectrum.

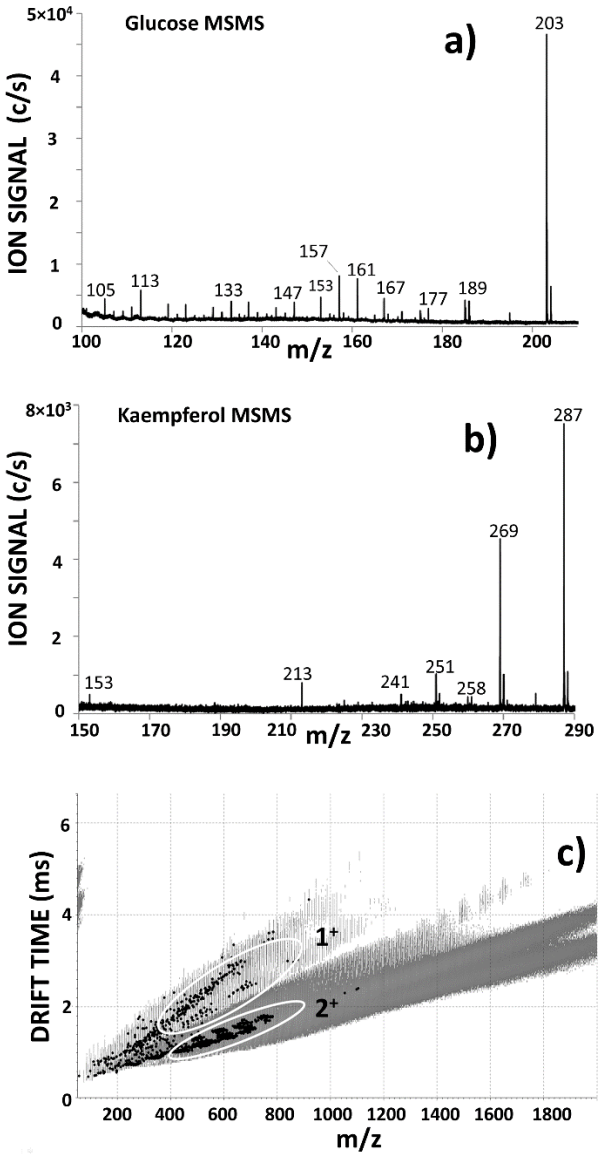

Figure 6. Typical tandem MS and IMS results for positive ions from geranium: a) tandem MS spectrum of glucose + Na^+, b) tandem MS spectrum of kaempferol + H^+, c) IMS plot of drift time vs. m/z values. Note separation of 2+ from 1+ ions, and diagonal swaths corresponding to different classes of compounds.

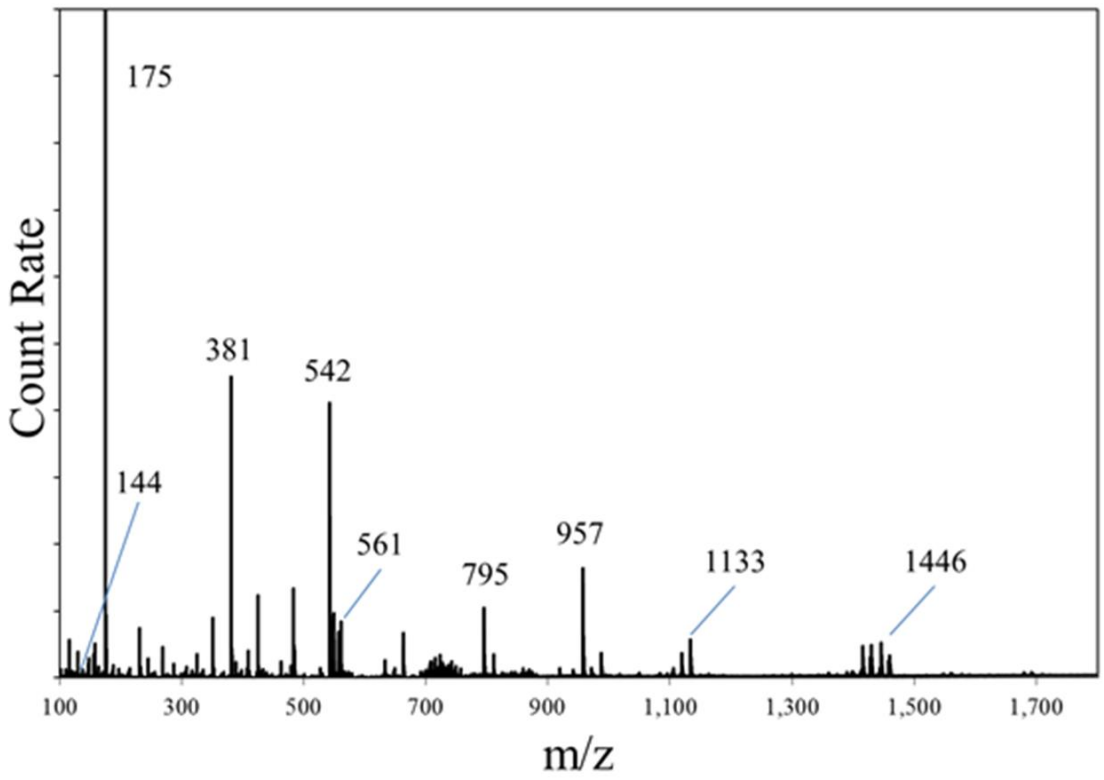

Figure 7. Integrated positive ion mass spectrum obtained from a hosta leaf acquired by atmospheric-pressure ELDI. The m/z 175 peak at m/z 175 (arginine + H^+) is much more intense and extends above the figure boundary. This mass spectrum is an average of both the yellow and green areas seen in Fig. 8 acquired in one ablation track. The ESI background has been subtracted from this ELDI spectrum.

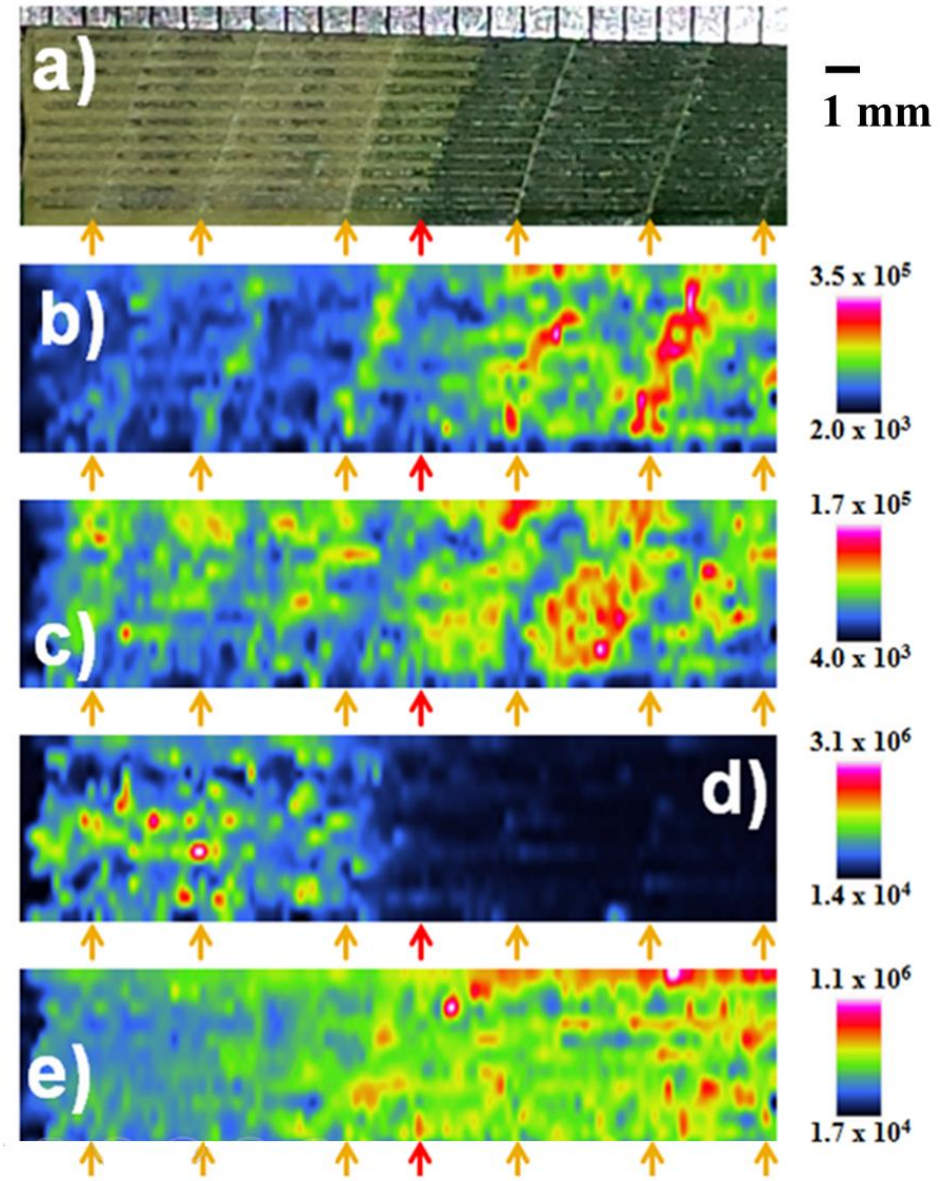

Figure 8. Images for positive ions from hosta leaf. a) Optical photograph long after ablation. The veins are ~ 3 mm apart. False color ion maps of hosta at b) m/z 561.171, assignment uncertain, c) m/z 663.126, kaempferol-methyl ether-galactoside-glucoside + $^{39}K^+$, d) m/z 175.117, arginine + H^+, and e) m/z 381.078, sucrose + $^{39}K^+$. The orange arrows at the bottom of each ion image corresponds to the observed veins in the photo in a). The red arrow corresponds to the position of the leaf where it distinctly changes from yellow to green.

CHAPTER 3.

LIGHT-DEPENDENT CHANGES IN THE SPATIAL LOCALIZATION OF METABOLITES IN SOLENOSTEMON SCUTELLARIOIDES (COLEUS HENNA) VISUALIZED BY MATRIX-FREE ATMOSPHERIC PRESSURE ELECTROSPRAY LASER DESORPTION IONIZATION MASS SPECTROMETRY IMAGING

A manuscript submitted to *Frontiers in Plant Science* (accepted, pending minor revisions)

Patrick A. McVey[1,2,3#], Liza E. Alexander[2,3,4#], Xinyu Fu[2,3,4], Bo Xie[2], Katherine-Jo Galayda[1,2,3,5], Basil J. Nikolau[2,3,4] and R.S. Houk[1,2,3*]

[1] *Department of Chemistry, Iowa State University, Ames, IA, USA*

[2] *Ames Laboratory-US DOE, Ames, IA, USA*

[3] *Center for Metabolic Biology, Iowa State University, Ames, IA, USA*

[4] *Roy J. Carver Department of Biochemistry, Biophysics and Molecular Biology, Iowa State University, Ames, IA, USA*

[5] *Kemin Industries Inc., 1900 Scott Ave, Des Moines, IA, USA*

[#]*These authors contributed equally to this article*

Abstract

The visualization of foliage color in plants provides immediate insight into some of the compounds that exist in the leaf. However, many non-colored compounds are also present; their cellular distributions are not readily identifiable optically. In this study we evaluate the applicability of mass spectrometry imaging (MSI) via electrospray

laser desorption ionization (ELDI) to reveal the spatial distribution of metabolites. ELDI-MSI is a matrix free, atmospheric pressure ionization method that utilizes a UV laser coupled with supplemental ionization by electrospray. We specifically applied ELDI-MSI to determine the spatial distribution of metabolites in Coleus Henna half leaves that were grown with half-sections either fully illuminated or shaded. We monitored dynamic changes in the spatial distribution of metabolites in response to the change of illumination every 7 days for a 28 day period. A novel source-sink relationship was observed between the 2 halves of the experimental leaf. Furthermore, Coleus Henna leaves present visually recognizable sectors associated with the differential accumulation of flavonoids. Thus, we correlated the effect of differential illumination and presence or absence of flavonoids with metabolic changes revealed by the accumulation of carbohydrates, amino acids, and organic acids. The results show the potential of ELDI-MSI to provide spatial information for a variety of plant metabolites with little sample preparation.

Introduction

Traditional mass spectrometry (MS) based methods of metabolite analysis require extraction of metabolites from biological samples, followed by chromatography. Spatial distribution data on metabolites are lost in these procedures. Recently, mass spectrometry imaging (MSI) has made a significant impact in filling this gap and has contributed to more refined understanding of many areas of biology (Amstalden van Hove et al., 2011; Lee et al., 2012; Nilsson et al., 2015; Shroff et al., 2015). Interrogating

the location of metabolites in multicellular organisms provides insight into the "sharing" of metabolic processes among different cell types.

Several ionization sources for MSI have been introduced. Each has its own unique advantages and limitations. Matrix assisted laser desorption ionization (MALDI) is the most widely used MSI technique in biology and can obtain spatial resolution as high as ~1 µm (Kompauer et al., 2017; Zavalin et al., 2015). MALDI performed in vacuum, coupled with different applied matrices, allows for the detection of a variety of metabolites (Klein et al., 2015; Shroff et al., 2015). However, the application of the matrix can complicate the use of MALDI especially for metabolites with low m/z values (Boughton et al., 2016) (<1000 Da), such as organic acids, sugars and amino acids. Laser ablation electrospray ionization (LAESI) generally uses an infrared laser to ablate particles from a biological surface, with water in the sample being the main IR absorber. The ablated plant particles undergo post-ionization via interaction with the ESI droplets before entering the mass spectrometer. As generally practiced, LAESI allows ~200 µm lateral resolution, while requiring little sample preparation because there is no applied matrix (Nemes & Vertes, 2007). Similar to the aforementioned methods, matrix assisted laser desorption electrospray ionization (MALDESI) utilizes an applied matrix to absorb radiation from an IR laser coupled with post-ionization via ESI; water ice is an effective matrix for MALDESI (Robichaud et al., 2014).

In the present study, electrospray laser desorption ionization (ELDI) with an ultraviolet laser (wavelength 355 nm) coupled with electrospray (Shiea et al., 2005), was used to analyze the spatial distribution of metabolites in plant samples. In this study, we

applied ELDI to Coleus (*Solenostemon scuttellarioides*) leaves that were grown with only half of the leaf surface illuminated. Coleus is a member of the *Labiatae* (mint) family, and different varieties are generally grown as ornamentals. The Coleus variety Henna is known for its serrated foliage. Its upper side is a unique uniform chartreuse to copper color. The underside is dark burgundy. These colors are primarily due to anthocyanin pigments that accumulate in these plants. The color intensity can be affected by illumination, temperature, and other environmental conditions (Lebowitz, 2011).

The present work evaluates ELDI-MSI to study the distribution of anthocyanins, flavonoids, and small metabolites (<1000 Da), including carbohydrates, organic acids and amino acids in Coleus leaves. The effects of different states of illumination during growth are assessed.

Material and Methods

Plant Growth, Maintenance and Light Conditions

Solenostemon scuttellarioides (Coleus Henna spp.) adult plants were obtained from Stam Greenhouse (Oskaloosa, IA). All plants were transferred to LC1 Sunshine Mix soil (Sun Gro Horticulture, Bellevue, WA), watered weekly, and grown in a growth room at 22° C under continuous illumination (2568 Lux or photosynthetic photon flux density 100 µmol of photons m^{-2} sec^{-1}).

For the light regulated experiments, half (through the leaf vein) of each leaf was covered length-wise with aluminum foil (shiny side up). The edges were sealed with scotch tape to ensure the covered region had limited light exposure. The leaves were

harvested from the same plant at one-week intervals for four weeks. Three biological replicates (one per plant per week) were used for each experimental platform (MS imaging, optical imaging and metabolic profiling for both anthocyanin and total metabolome).

Leaves for anthocyanin and total metabolic analysis were harvested each week, cut through the middle vein to separate the light-exposed surface from the shaded/dark-surface, and immediately flash-frozen using liquid nitrogen. The samples were then dried using a vacuum lyophilizer and pulverized using a Mixer Mill 301(Retsch GmbH, Germany) in 2 mL Eppendorf tubes prior to extraction.

For MS imaging, samples were gently cut from both the foil-covered and uncovered edge of the leaf. Sections measuring approximately 12 mm by 8 mm were immediately analyzed using ELDI. Leaf edges were also visualized under a light microscope.

Tissue Sectioning and Microscopy

For microscopy only, leaf edges were hand-sectioned using a vibratome (TPI-3000; www.tedpella.com) at 70 to 100 µm. The sections were mounted in water and visualized under bright-field using a BH40 compound microscope (Olympus, www.olympus-global.com) equipped with Axio Vision software (Carl Zeiss Inc., Thorwood, NY). Additionally, a fresh leaf was ablated and the depth of the ablation trenches were measured using a Keyence VHX-5000 Digital Microscope.

Anthocyanin Extraction

Compounds were extracted from 5 mg of lyophilized Henna leaf tissue using 300 µL of methanol/ water/ acetic acid (85:15:0.5; v/v/v) and sonicated for 1 hour. Samples were then incubated in dark at 4^{o}C for 2 hours (Wu, Gu, Prior, & McKay, 2004). The samples were centrifuged for 5 minutes at 13,000 rpm and the liquid phase was filtered twice using 13 mm x 0.45 µm Teflon Syringe filters (Supelco, PA) for HPLC MS analysis.

HPLC-MS and MS/MS Analysis of Anthocyanins

The chromatographic separations were performed with an Agilent Technologies 1100 series HPLC. This was coupled with an Agilent Technologies Mass Selective Trap SL detector, equipped with an electrospray ionization (ESI) source with an autosampler/injector and diode array detector (DAD) for LC-MS analysis. A silica-based reverse-phase C18 Atlantis T3 column (2.1 × 150 mm, 3 µm, Waters, Milford, MA) was used for separation. Elution was performed using mobile phases containing 5% formic acid in LC-MS grade water or methanol (MeOH). The flow rate was kept at 0.2 mL/min and the DAD detection was at UV Vis wavelength 520 nm. After 5 µL of sample injection, a gradient was used as follows: 0 to 6 min, 0 to 20% MeOH; 6 to 40 min, 20 to 50% MeOH; 40 to 44 min, 50 to 50% MeOH; 44 to 48 min, 50% to 100% MeOH 48 to 52 min, 100% MeOH; 52-56 min, 100 to 0% MeOH. The column effluent was then introduced via ESI into an Agilent 6210 MSD time-of- flight mass spectrometer operating in positive mode. The ESI capillary voltage was +3.0 kV, nitrogen gas temperature was set to 350 °C, drying gas flow rate was 11 L/min, nebulizer gas pressure was 35 psi, skimmer was

65 V, and OCT RF was 250 V. Mass spectra from *m/z* 100 to 2000 were collected and analyzed using Agilent ChemStation Data Analysis. Individual anthocyanin peak areas were generated by Quant Analysis and used to compare different levels of anthocyanins quantitatively. The structure for each anthocyanin was identified from detailed MS/MS analysis performed at various collision energies.

Total Metabolite Analysis by GC-MS

Total metabolite extractions were carried out as described previously (Schmidt et al., 2011). Extracts were prepared from 2 mg of lyophilized leaf tissue. The extracts were spiked with two internal standards: 10 µg of ribitol and 5 µg nonadecanoic acid for polar and non-polar fractions, respectively. To 5 mg of lyophilized tissue, 0.35 ml of hot methanol (60° C) was added. The sample was incubated at the same temperature for 10 min, followed by sonication for 10 min at full power. To this slurry, 0.35 ml of chloroform and 0.3 ml of water were added and the mixture was vortexed for 1 to 3 min. After centrifugation for 5 min at 13,000 g, 200 µl of the upper phase (polar fraction) and 200 µl of the lower phase (non-polar fraction) were separately removed into 2 ml GC-MS vials, and dried in a Speed-Vac concentrator (model SVC 100H, Savant, NY).

The samples were then methoximylated and silylated. For methoximation, 50 µl of 20 mg/mL methoxyamine hydrochloride dissolved in dry pyridine was added. The reaction mixture was shaken at 30°C for 1.5 hours. Silylation was performed by adding

70 μL of *N*, *O*-Bis (trimethylsilyl) trifluoroacetamide (BSTFA) with 1% trimethylchlorosilane (TMCS) and incubating at 65°C for 30 min.

One microliter of the derivatized samples was injected into the GC-MS in splitless mode. GC-MS analysis was performed using an Agilent 6890 GC interfaced to an Agilent 5973 quadrupole MS with a HP-5ms (5%-Phenyl)-methylpolysiloxane column (30 m x 0.25 mm x 0.25 μm, Agilent). The temperature was programmed from 70 to 320°C at 5°C/min with helium flow rate at 1.0 mL/min and inlet temperature at 280°C. EI-MS ionization energy was set to 70 eV and the interface temperature was 280°C.

The GC-MS data files were deconvoluted and searched against an in-house MS-library, the NIST 14 Mass Spectral Library using NIST AMDIS software (Stein, 1999) and the Golm Metabolome Database (Hummel et al., 2010). Total metabolite profiling data obtained by GC-MS analysis, and anthocyanin data obtained from LC-fluorescence are publicly available in the PMR database (http://metnetdb.org/PMR/; Hur et al., 2013).

ELDI-MS

A Waters Synapt G2-S quadrupole time-of-flight mass spectrometer was used for data collection for all MSI. The Waters ESI source was removed and a homemade open-air ESI source (Galayda et al. 2017) was used with samples at ambient pressure. Data were acquired in the mass range from *m/z* 50 to 1200, spectra were summed for 0.3 seconds. The time-of-flight reflectron operated in single-pass mode with a resolution of ~10,000 FWHM for MS images. The TOF was then operated in double-pass mode with a resolution of ~40,000 FWHM, or “high resolution mode”, to confirm compound

identifications by accurate m/z measurements. These confirmatory measurements were done on a different segment taken from the same leaf. Tandem MS quadrupole resolution varied from Δm = 5 to 12 depending on the analyte with a nominal collision energy of 20 eV. The Synapt was operated using Waters MassLynx V4.1 (SCN851) software.

Data Handling

Spectra were generated from total ion chromatograms (TIC) combined by the MassLynx software. The ".raw" Waters data files were converted to mzML files by Proteowizard Mass Converter Tool. The MzML files were then combined into an imzML file using imzML Converter. This combined image file was then viewed and images were generated from MSiReader V0.06 via the W.M. Keck FTMS Laboratory. All images made within MSiReader had Linear^2 interpolation for image clarity, and used the "Jet" colormap/false color appearance. Co-localization and 3D images were created with MSiReader V1.00.

ELDI Compound Identification Protocol

Compounds were identified from the ELDI spectra in a multiple step process to ensure confident assignments. Initial ELDI measurements were done in so-called "sensitivity" mode, m/Δm ~10,000 FWHM. Based on these results, high resolution spectra at ~40,000 were acquired on a different segment of the same leaf for accurate mass measurements. Next, if the compound was of high enough abundance and

without background interferences, tandem mass spectra were taken to provide a fragmentation pattern. These high resolution *m/z* values were then put into online metabolite databases to generate possible compound matches based on accurate mass and tandem MS (if available from both ELDI data and the online database). ELDI data were also compared to the corresponding GC-MS and LC-MS data acquired from Coleus Henna leaves for identity overlap. Every possible ID was given a Δppm value based on the experimental *m/z* value compared with the true *m/z* value of the compound. These Δppm values were generally below 5 ppm. Some compounds were given identifications with greater than 10 Δppm values based on matches with the GC-MS data and/or tandem MS matches with the online database. Some flavonoid peaks were assigned as cyanidin or apigenin derivatives despite no database matches due to highly abundant tandem MS product peaks at *m/z* 287.0585 or 271.0627, respectively.

Acquiring tandem MS data with ELDI was successful for most peaks of interest, but was not always possible. It was difficult to acquire tandem MS spectra for highly spatially localized compounds, labeled “localized signal” in subsequent data tables. Compounds with a relatively low abundance did not give a satisfactory fragmentation pattern for identification purposes (labeled “too low abun.” in subsequent data tables). Analyte peaks near major background peaks had interferences with their tandem MS spectra. The quadrupole resolution could sometimes be increased to eliminate these interferences, but a subsequent drop in peak intensity sometimes resulted in poor tandem MS results.

ELDI Source

The apparatus has been described (Galayda et al., 2017). Samples were ablated with a Nd:YAG laser (ULTRA, Big Sky Laser Tech, Inc. Bozeman, MT). The third harmonic was used at 355 nm. The laser was operated at a pulse repetition rate of 10 Hz, with a 5 ns pulse width, and an energy of ~250 µJ/pulse (before focusing). This pulse energy was just above the ablation threshold for these samples. The beam was focused onto the sample by a single plano-convex focusing lens (fused-silica, focal length 75 mm), with a nominal spot size of ~125 µm.

Samples were cut with a scalpel. Immediately after cutting, the sample segments were mounted on a glass slide using double sided tape. The laser did not penetrate completely through the sample; the underlying tape is not ablated. No matrix was applied, and leaves were pressed lightly to create an even surface. Plant samples were then placed 8 mm below the ESI-sample inlet axis on a computer-controlled translation stage (Z825B, Thorlabs, Inc. Newton, NJ). Samples were translated at 0.4 mm/sec beneath the 10 Hz laser beam down the surface of the leaf to insure fresh tissue was constantly being ablated. The distance between the centers of adjacent ablation tracks was 125 µm, providing a lateral resolution of 125 µm. The ablation trench was ~ 30 µm deep. The underlying tape was not ablated. Mass spectra were averaged over 0.3 second intervals. Thus, the ablated volume was 125 µm x 120 µm x 30 µm deep. The leaves were irradiated normal to the sample surface with the laser beam axis ~2 mm downstream from the ESI capillary. The ESI tip was ~10 mm from the sample inlet (Galayda et al., 2017).

A solution of 50% methanol with 0.1% formic acid (99.5% purity, Fisher Scientific) was pumped through a 53 µm ID polyimide coated capillary as the ESI solution (pump: model Z2, Harvard Apparatus, South Natick, MA). Leucine enkephalin was added at 0.1 ppm to the ESI solution for use as a mass calibrant. All data were acquired in positive ESI mode. The ESI voltage for ELDI was +2.5 kV applied to a stainless steel union in the liquid flow line, with the sample cone completing the ESI circuit. The sample inlet was kept at 100^{o} C with a N_2 curtain gas flow of 1 L/hr.

Results

Overview of Experimental Workflow

The mid-rib **(Figure 1)** was used as the boundary between the two halves of each Coleus leaf. One half of a leaf was covered with aluminum foil to generate leaf tissue that was grown under lower illumination conditions, and the uncovered half of the leaf was used as a control for normal levels of illumination. Each leaf was dissected transversely. Segments ~12 mm x 8 mm were collected from both the illuminated and shaded sides of the leaf. These segments were placed on a glass slide and used in ELDI imaging experiments.

Metabolite distribution maps were created for 77 chemically identified ions detected by ELDI-MS. Thirteen of these identified ions were observed to decrease in abundance in the shaded side of the leaf, while the abundances of eleven compounds increased in the shaded side. The relative abundances of the remaining 53 ions were unaffected by shading **(Tables 1-3)**. In-parallel, targeted anthocyanin analysis via LC-MS,

and non-targeted global metabolomic analysis via GC-MS was performed on separate leaf samples, which were sampled in triplicate.

Illumination Affects Foliage Color and Anthocyanin Abundances

Under normal illumination conditions both the adaxial (upper) and abaxial (lower) surfaces of the Coleus Henna leaf are a burgundy red-purple color. In the shaded condition, the foliage color changes from burgundy red-purple to chartreuse green **(Figure 2)**. Microscopic cross-sections of leaves reveal that the abaxial and adaxial epidermal cells are heavily red-pigmented, and the mesophyll and palisade layers are green pigmented with chlorophylls. Epidermal cells range from 20 to 50 µm deep with cross-sections in the range of 40 to 55 µm long. These cell dimensions are unaffected by shading. The red pigmentation was decreased in the adaxial epidermis, and unaltered in the abaxial epidermis. This loss of the red pigment from the adaxial epidermis revealed the underlying chlorophyll pigments, imparting the green color to the shaded half of the adaxial surface of the leaf **(Figure 3)**.

Effect of Shading on the Extractable Leaf Metabolome

The GC-MS analyses of metabolite extracts from leaf tissue detected 156 polar and non-polar analytes; 67 of these were identified chemically. These metabolites include alcohols, polyols, sugars, lipids, fatty acids, esters, sterols, hydrocarbons, organic acids, and nitrogenous metabolites. The abundances of most of the chemically identified metabolites remained unaltered irrespective of the illumination conditions **(Figure 4)**.

The abundances of a few metabolites, such as gluconic acid, fructose, arachidonic acid, 1-monopalmitin and a hexose sugar, increased in the shaded side of the leaf as time progressed. The abundance of fructose increased in the shaded side of the leaf and became higher than in the illuminated side by the 28th day of the experiment. Benzoic acid showed a unique profile, with abundance decreasing through the time-line of the experiment; its abundance was always higher in the shaded side of the leaf.

Targeted LC-MS analyses measured changes in anthocyanin concentrations during these experiments. Nine cyanidin-based anthocyanins **(Figure 5)** were identified. Two of these showed differential accumulation between the illuminated and shaded sides of the leaf: cyanidin-coumaroylglucoside-malonylglucoside at *m/z* 843.1970 and cyanidin-coumaroylglucoside-dimalonylglucoside at m/z 929.1966. The abundance of both these anthocyanins decreased significantly in the shaded side of the leaf after 21 days of the experiment. The accumulation of the other 7 anthocyanins was unaffected by the difference in illumination.

ELDI-MS Identification of Flavonoids

The pigmentation on the abaxial side of the leaf was unaffected by shading, whereas the pigmentation pattern was altered on the adaxial side of the leaf. Therefore, we focused on imaging the distribution of the metabolites on the adaxial surface using ELDI-MSI. Many of the ions detected in these ELDI spectra were attributed to flavonoids. Their chemical identity was confirmed by MS/MS experiments that generated fragment ions characteristic of the flavonoid backbones. The identities of

these fragment ions were confirmed by matching accurate mass measurements with entries in the Metlin database (Smith et al., 2005). This strategy identified two main classes of flavonoids, based on the aglycone cores: a) apigenin, a flavone **(Figure 6A)**, and b) cyanidin, an anthocyanin **(Figure 6B)**.

Apigenin was identified as its protonated ion $[M+H]^+$ at *m/z* 271.0627. All analytes that generated this fragment ion by tandem MS were inferred to be apigenin-based flavones. Cyanidin has a permanent +1 charge and was identified as an $[M]^+$ ion at *m/z* 287.0585. Cyanidin was distinguished from isobaric compounds (e.g., luteolin or kaempferol) based on MS/MS fragments derived from this $[M]^+$ ion **(Table 1).** Cyanidin-based anthocyanins were identified by cyanidin $[M]^+$ product ions at *m/z* 287.0585. The high intensities of the apigenin-aglycone (*m/z* 271.0627) and cyanidin-aglycone (*m/z* 287.0585) ions in the overall ELDI spectrum **(Figure 6C)** show that the aglycones have a high relative abundance compared to other low mass molecules observed.

The cyanidin-based anthocyanins are primarily glycosylated and further biochemically modified by malonylation or coumarylation **(Table 1)**. These anthocyanins generated common fragment ions at *m/z* 163.0620 and 147.0485, which were identified as the protonated water-loss ion $[M-H_2O+H]^+$ of a hexoglycoside, and the protonated water-loss ion $[M-H_2O+H]^+$ of coumaric acid, respectively. The glycone moiety was not identified directly. However, based on the METLIN and the KEGG pathway databases (Guijas et al., 2018; Smith et al., 2005), and prior characterization of these metabolites in other Coleus lines (Boldt, 2013), these glycosides are subsequently

referred to as glucosides. Collectively therefore, we identified 15 cyanidin-based anthocyanins **(Table 1)**.

Similar characterizations identified four apigenin-based flavones, including the apigenin aglycone. Tandem MS generated the apigenin backbone product ion but the specific chemical structures of these apigenin-based flavones were not determined. The ELDI experiments identified five apigenin-based flavones at *m/z* 447.0918*, m/z* 489.1057*, m/z* 619.2228, m/z 635.2041, and *m/z* 743.1454 **(Table 1)**.

Effect of Shading on the Spatial Distribution of Flavonoids

The 15 chemically identified cyanidin-derived anthocyanins can be categorized into three classes. Eight are less abundant in the shaded side of the leaves, one is more abundant in the shaded side, and six are not affected by the difference in illumination **(Table 1)**. This last category includes the cyanidin aglycone, whose abundance are unaffected by shading during the entire 28-day period of the study, same as the apigenin aglycone **(Figure 6D)**. Additional example images are presented in **Figure 7,** which shows the spatial distribution of five chemically identified cyanidin-based anthocyanins and three apigenin-based flavonoids. These include cyanidin-malonylglucoside (*m/z* 535.1069 $[M]^+$), cyanidin-coumaroyl glucoside (*m/z* 595.1447 $[M]^+$), cyanidin-coumaroylglucoside-glucoside (*m/z* 757.1965 $[M]^+$), cyanidin-coumaroylglucoside-malonylglucoside (*m/z* 843.1970 $[M]^+$), and cyanidin-coumaroylglucoside-dimalonylglucoside (*m/z* 929.1966 $[M]^+$); and the apigenin flavonoids at *m/z* 447.0918 $[M+H]^+$, *m/z* 619.2228 $[M+H]^+$, and *m/z* 743.1454 $[M+H]^+$.

The anthocyanin with the highest relative abundance, cyanidin-coumaroylglucoside-malonylglucoside (*m/z* 843.1970 $[M]^+$), is initially equally abundant in both illuminated and shaded sides of the leaf. However, starting at 14 days its abundance is reduced more rapidly in the shaded side of the leaf **(Figure 7)**. A similar distribution pattern after 28 days of shading is observed for the structurally related cyanidin-coumaroylglucoside (*m/z* 595.1447 $[M]^+$). In contrast, cyanidin-coumaroylglucoside-glucoside (*m/z* 757.1965 $[M]^+$) is equally abundant in both the illuminated and shaded sides after 28 days **(Figure 7).** This anthocyanin had the second highest relative abundance and may be the immediate metabolic precursor to cyanidin-coumaroylglucoside-malonylglucoside (Guijas et al., 2018). Three-dimensional temporal distribution patterns of these structurally related anthocyanins (*m/z* 843.1970 $[M]^+$, *m/z* 757.1965 $[M]^+$, *m/z* 595.1447 $[M]^+$ and *m/z* 287.0585 $[M]^+$) after 28-days of shading are presented in **Figure 8**.

Similar to cyanidin-coumaroylglucoside-glucoside, the abundance of the dimalonylated derivative, cyanidin-coumaroylglucoside-dimalonylglucoside (*m/z* 929.1966 $[M]^+$), is lower in the shaded side of the leaf **(Figure 7)**. A precursor to cyanidin-coumaroylglucoside-dimalonylglucoside, the cyanidin-malonylglucoside (*m/z* 535.1069 $[M]^+$) is equally abundant in both the illuminated and shaded sides until 28-days of shading, where its abundance is reduced in the illuminated side of the leaf **(Figure 7)**. All these changes in relative abundance of cyanidin-based anthocyanins, revealed by ELDI-MSI, were confirmed by LC-MS analysis of extracts from these leaves **(Figure 5)**.

The spatial redistribution of two apigenin-based metabolites was revealed by MSI. For example, the apigenin-based flavonoid at *m/z* 619.2228 occurs in both illuminated and shaded sides of the leaves and concentrates in the periphery of the shaded leaf-half **(Figure 7)**. Another apigenin-based flavonoid at *m/z* 743.1454 is initially located in the periphery of the shaded leaf-half. It redistributes temporally to become more evenly dispersed among the two halves of the leaf **(Figure 7)**.

MSI Profiles of Carbohydrates

Twelve sugars and sugar derivatives were chemically identified using three MS-based criteria: a) accurate mass determination with ELDI; b) ELDI-MS/MS fragmentation spectra; and c) integrated retention index and electron impact fragmentation patterns from GC-MS analysis. Most of the 12 sugars were observed as $^{39}K^+$ and/or Na^+ adducts by ELDI **(Table 2)**. Specifically, sucrose was identified by MS/MS fragmentation patterns upon ELDI, and also by GC-MS analysis of extracts. A hexose, possibly glucose, was identified as both Na^+ (*m/z* 203.0560) and $^{39}K^+$ (*m/z* 219.0310) adducts. The identity of a phosphorylated hexose (possibly glucose-phosphate) was inferred from accurate mass determination of the $^{39}K^+$ adduct (*m/z* 312.9720). An organic acid glucoside (possibly coumaroyl glucoside) was identified by MS/MS experiments as both the Na^+ (*m/z* 349.0923) and $^{39}K^+$ (365.0647) adducts. A heptose was identified by accurate mass determination and by MS/MS fragmentation spectra, but the particular isomer could not be determined.

The abundances of eight of these sugar metabolites were unaffected by the illumination status of the leaf **(Table 2).** The spatial distributions of six typical metabolites are shown in **Figure 9**. Three of these sugar metabolites (*m/z* 203.0560, *m/z* 312.9720, *m/z* 349.0923) become more abundant over time in the shaded side of the leaf. Finally, a sugar-derivative, believed to be hexose-glycerol phosphate (*m/z* 357.0586), as determined by accurate mass, became less abundant across the entire leaf after 28 days of shading **(Figure 9)**.

MSI Profiles of Organic and Amino Acids

Table 3 lists the carboxylic acids and amino acids that were observed by ELDI-MSI. Seven of these metabolites were identified as H^+ adducts, 15 as H^+ adducts accompanied by water loss, two as Na^+ adducts, and three as $^{39}K^+$ adducts. Several of these compounds were observed as multiple adducts; individual molecules of a given compound had one of either H^+, Na^+ or $^{39}K^+$ attached in the same spectrum.

Several analytical strategies were integrated to confirm the chemical identity of these organic acids, including accurate mass determination, MS/MS experiments, and GC-MS analysis of derivatized metabolite extracts. The latter strategy was also used to confirm the relative concentrations between the illuminated and shaded sides of the leaves. Collectively these analyses identified 23 organic acids. Eight were identified with ELDI-MS and the molecular images of these metabolites **(Figure 10)** indicate their abundances were unaffected by the shading of the leaf, except for glycolic acid seen only by GC-MS.

The locations of 12 proteogenic amino acids (alanine, arginine, asparagine, aspartic acid, glutamine, glycine, histidine, leucine, proline, serine, threonine, and valine) were determined by ELDI-MSI. The non-proteogenic amino acids were pyroglutamic acid and GABA **(Figure 11)**. Arginine, aspartic acid, and histidine were considerably more abundant in the shaded side of the leaf, although in the case of histidine this increase occurred after the half-leaf was shaded for 21 days. The spatial distribution of seven amino acids were unaffected by shading, but the relative abundance of four amino acids changed as time progressed. Specifically, leucine abundance increased at 28 days, whereas the abundance of alanine (decreased from day 14 to 28), glycine (peaked day 14 decreased from day 21 onwards), and proline (depleted by day 21) was reduced during this time period.

Discussion

Several MSI methods have been utilized to obtain spatial distribution data of metabolites in plant samples. Each offers unique advantages and drawbacks (Boughton et al., 2016; Lee et al., 2012). The present work demonstrates the potential of applying ELDI for MSI. ELDI is analogous to LAESI, with the exception that ELDI uses ultraviolet radiation for ablation (e.g., 355 nm laser), whereas LAESI generally uses infrared radiation, for example a 2940 nm mid-IR laser (e.g., Nemes & Vertes, 2007). Although ELDI has previously been reported with fungi (i.e., *Ganoderma lucidum* and *Antrodia camphorate*) (Huang et al., 2012), there is only one other moderately extensive plant application study using ELDI, LAESI, or MALDESI (Etalo et al., 2015). The spatial

resolution was limited to 500 µm in that work (Etalo et al., 2015). Many proof-of-concept experiments using LAESI-MSI on plants have been reported (Bartels & Svatoš, 2015).

Because plants accumulate large quantities of UV-absorbing molecules (e.g., flavonoids, chlorophylls, terpenes, phenolics) the plant leaf itself serves as a pseudo-matrix. Ablation of the plant pseudo-matrix enables ELDI-based observation of additional molecules that are not UV absorbers (e.g., sugars, amino acids and organic acids). In both ELDI and LAESI methods, particles undergo post-ionization via interaction with ESI droplets, and the resulting ions are then extracted into the mass spectrometer. Although LDI without post-ionization via ESI can achieve much higher spatial resolution, issues associated with ionization transfer still need to be addressed (Hölscher et al., 2009).

One concern about our ELDI method is possible spatial heterogeneity of the UV-absorbing pseudo-matrix. Coupling electrospray and ablation with a UV laser appears to minimize these issues. Both UV and non-UV absorbing compounds can be measured at atmospheric pressure. For example, **Figure 12** illustrates the localization of the UV-absorbing flavonoid cyanidin-coumaroylglucoside-glucoside (*m/z* 757.1965 [M^+]) and the localization of the non-UV absorbing metabolites, histidine, sucrose and glucose. Non-absorbing analytes can be observed readily in regions where the abundances of the pseudo-matrix flavonoids are relatively low **(Figure 12)**. These comparisons indicate that ELDI-based MSI can be used to localize the distribution of non-UV absorbing

metabolites despite large spatial changes in concentration of flavonoids or other possible pseudo-matrix compounds.

Coleus is convenient because its leaves are sectored visually. This reflects the spatial arrangement of the underlying flavonoids (Boldt, 2013; Nguyen & Cin, 2009; Nguyen et al., 2008). Moreover, in Coleus the sectoring of the adaxial surface is different from that of the abaxial surface. The adaxial surface is further modifiable by changes in the exposure to illumination (Nguyen & Cin, 2009; Logan et al., 2015). In addition, the depth of the leaf adaxial cells matches the penetration depth of the laser (~30 µm). Thus, the images presented herein reflect the abundance of metabolites in the epidermal cell layer of the leaf.

Correlated with the visible changes in the pigments of the leaf in response to shading, major metabolic changes in anthocyanins were visualized by ELDI-MS and quantitatively confirmed by LC-MS analysis of metabolite extracts. The cyanidin glycosides are the most abundant anthocyanins in the illuminated side of the leaves, which correlates with their photo-inhibitory potential (Steyn et al., 2002). Consistent with this photo-inhibitory attribute, the abundances of 17 of the 39 detected anthocyanins decreased upon shading of the leaf. Moreover, in response the illumination status of the leaf, there is a coordinated change in the differential abundance of the structurally related anthocyanins, cyanidin-coumaroylglucoside-glucoside, cyanidin-malonyl glucoside, and the aglycone cyanidin. The ability to visualize this coordination at a spatial level provides additional insights to their potential metabolic interconnections. Namely, the enhanced accumulation of cyanidin-

coumaroylglucoside-malonylglucoside, in response to illumination, may be associated with increased biosynthesis. The correlated changes in the levels of the potential precursors (i.e., cyanidin-malonyl glucoside) **(Figure 8)** support this hypothesis.

Multi-cellular photosynthetic plants are characterized by a series of source-sink tissues, that share the metabolic tasks of converting inorganic precursors, such as CO_2, ammonia, phosphate etc., to organic constituents that are normally stored in sink tissues, such as seeds, tubers etc. (Basu et al., 1999; Wardlaw, 2006; Lemoine et al., 2013; Osorio et al., 2014; Paul & Foyer, 2001; Roitsch, 1999; Turgeon, 1989). Source-sink relationships can be genetically programmed and are further modified by environmental abiotic or biotic stimuli that are mediated by small molecules (e.g., sugars and amino acids) (Krapp & Stitt, 1995; Lemoine et al., 2013; McCormick et al., 2008; Paul & Driscoll, 1997; Roitsch, 1999). ELDI-MSI can image metabolic changes associated with the induction of an artificial new source-sink relationship between two halves of a leaf. The fully illuminated half of the leaf serves as the source tissue that fixes carbon, primarily in the form of sugars. These compounds are exported to the shaded half of the leaf that serves as the new sink tissue, whose strength increases with increasing time of shading **(Figure 9).** (Bagnall et al., 1988; Islam et al., 2005; Paul et al., 1992; Steyn et al., 2002).

ELDI revealed that the distribution of sugars (tetroses, pentoses, heptoses, and sucrose) were not significantly affected by the difference in the illumination between the two halves of the leaves. Only the distributions of glucose and a hexose phosphate (presumably glucose-6-phosphate) were affected; they increased on the shaded side **(Figure 9)**. Therefore, the illuminated source-side of the leaf compensated for the

reduced photosynthesis that was imposed by shading the other half of the leaf. This sugar-based interrelationship between source-sink tissues often manifests coordinated changes in amino acid metabolism, associated with the affiliation between carbon and nitrogen metabolism (McCormick et al., 2006; Paul & Driscoll, 1997). These changes in amino acid metabolism are usually associated with photosynthetic source tissues, where changes in RUBISCO levels (the major sink for amino acids) can drastically affect free amino acid pools (Nielsen et al., 2002; McCormick et al., 2008; Paul & Driscoll, 1997). Thus, in our studies we visualized increasing levels of Arg, Asp, His in the shaded side of the leaf **(Figure 11)**, probably reflecting the turnover of RUBISCO as photosynthetic capacity was reduced in the dark, sink-side of the leaf.

Conclusion

This study demonstrates the capabilities of ELDI-MSI for identification and spatial characterization of a wide variety of compounds in plant tissues with minimal sample preparation requirement. The ability to generate spatial distribution data that are consistent with biological explanations provides confidence in the validity of the observations. Future experiments include a) separation of isobaric ions by ion mobility, and b) implementation of procedures for quantification with spatial resolution by ELDI.

Acknowledgements

This research was supported by funds from the U.S. Department of Energy, Office of Biological and Environmental Research through award DESC0014038 to Iowa State

University. B.J.N. and L.E.A. were partially supported by the Center for Metabolic Biology, Iowa State University (www.metabolicbiology.iastate.edu). The ELDI-MSI instrumentation was funded by the Office of Basic Energy Sciences, Separations and Analysis Program, U. S. Department of Energy. Metabolomics analyses were conducted at the Iowa State University's W. M. Keck Metabolomics Research Laboratory (metabolomics.biotech.iastate.edu), and we thank Dr. Lucas J. Showman and Dr. Ann M. Perera for their expert advice. Microscopic data were gathered at Iowa State University's Microscopy and NanoImaging Facility, and we thank Ms. Tracey Stewart and Dr. Harry T. Horner for their expert advice and assistance.

Conflict of Interest Statement

The authors declare that the research was conducted in the absence of any commercial or financial relationships that could be construed as a potential conflict of interest.

References

Amstalden van Hove, E. R., Smith, D. F., Fornai, L., Glunde, K., & Heeren, R. M. A. (2011). An Alternative Paper Based Tissue Washing Method for Mass Spectrometry Imaging: Localized Washing and Fragile Tissue Analysis. *Journal of the American Society for Mass Spectrometry*, *22*(10), 1885–1890. http://doi.org/10.1007/s13361-011-0203-z

Angel, P. M., & Caprioli, R. M. (2013). Matrix-Assisted Laser Desorption Ionization Imaging Mass Spectrometry: In Situ Molecular Mapping. *Biochemistry*, *52*(22), 10.1021/bi301519p. http://doi.org/10.1021/bi301519p

Bagnall, D. J., King, R. W., & Farquhar, G. D. (1988). Temperature-dependent feedback inhibition of photosynthesis in peanut. *Planta (Germany, F.R.)* 175:348. https://doi.org/10.1007/BF00396340

Bartels, B., & Svatoš, A. (2015). Spatially resolved in vivo plant metabolomics by laser ablation-based mass spectrometry imaging (MSI) techniques: LDI-MSI and LAESI. *Frontiers in Plant Science*, *6*, 471. http://doi.org/10.3389/fpls.2015.00471

Basu, P. S., Sharma, A., Garg, I. D., & Sukumaran, N. P. (1999). Tuber sink modifies photosynthetic response in potato under water stress1Publication No. 1408, CPRI, Shimla.1. *Environmental and Experimental Botany*, *42*(1), 25–39. https://doi.org/10.1016/S0098-8472(99)00017-9

Boldt, J. K. (2013). Foliar anthocyanins in coleus and ornamental grasses: accumulation, localization, and function. Retrieved from the University of Minnesota Digital Conservancy, http://hdl.handle.net/11299/150590.

Boughton, B. A., Thinagaran, D., Sarabia, D., Bacic, A., & Roessner, U. (2016). Mass spectrometry imaging for plant biology: a review. *Phytochemistry Reviews*, *15*(3), 445–488. http://doi.org/10.1007/s11101-015-9440-2

Etalo, D. W., De Vos, R. C. H., Joosten, M. H. A. J., Hall, R. D. (2015). Spatially Resolved Plant Metabolomics: Some Potentials and Limitations of Laser-Ablation Electrospray Ionization Mass Spectrometry Metabolite Imaging. *Plant Physiology*, 169(3), 1424-1435. https://doi.org/10.1104/pp.15.01176

Galayda, K. (2017). Use of ultraviolet laser ablation electrospray ionization mass spectrometry for plant metabolite imaging. *Graduate Theses and Dissertations. 15517.* Retrieved from https://lib.dr.iastate.edu/etd/15517

Guijas, C., Montenegro-Burke, J. R., Domingo-Almenara, X., Palermo, A., Warth, B., Hermann, G., Koellensperger, G., Huan, T., Uritboonthai, W., Aisporna, A. E., Wolan, D. W., Spilker, M. E., Benton, H. P., & Siuzdak, G. (2018). METLIN: A Technology Platform for Identifying Knowns and Unknowns. *Analytical Chemistry*, *90*(5), 3156–3164. http://doi.org/10.1021/acs.analchem.7b04424

Hölscher, D. , Shroff, R. , Knop, K. , Gottschaldt, M. , Crecelius, A. , Schneider, B. , Heckel, D. G., Schubert, U. S. and Svatoš, A. (2009). Matrix-free UV-laser desorption/ionization (LDI) mass spectrometric imaging at the single-cell level: distribution of secondary metabolites of Arabidopsis thaliana and Hypericum species. *The Plant Journal*, *60*(5), 907–918. http://doi.org/10.1111/j.1365-313X.2009.04012.x

Huang, M.-Z., Cheng, S.-C., Jhang, S.-S., Chou, C.-C., Cheng, C.-N., Shiea, J., Popov, I.A., Nikolaev, E. N. (2012). Ambient molecular imaging of dry fungus surface by electrospray laser desorption ionization mass spectrometry. *International Journal of Mass Spectrometry*, *325–327*, 172–182. https://doi.org/10.1016/j.ijms.2012.06.015

Hummel, J., Strehmel, N., Selbig, J., Walther, D., & Kopka, J. (2010). Decision tree supported substructure prediction of metabolites from GC-MS profiles.

Metabolomics, *6*(2), 322–333. http://doi.org/10.1007/s11306-010-0198-7

Hur, M., Campbell, A. A., Almeida-de-Macedo, M., Li, L., Ransom, N., Jose, A., Crispin, M., Nikolau, B. J., Wurtele, E. S. (2013). A global approach to analysis and interpretation of metabolic data for plant natural product discovery. *Natural Product Reports*, *30*(4), 565–583. http://doi.org/10.1039/c3np20111b

Islam, M. S., Jalaluddin, M., Garner, J. O., Yoshimoto, M., & Yamakawa, O. (2005). Artificial shading and temperature influence on anthocyanin compositions in sweetpotato leaves. *HortScience*, *40*(1), 176–180.

Klein, A. T., Yagnik, G. B., Hohenstein, J. D., Ji, Z., Zi, J., Reichert, M. D., MacIntosh, G. C., Yang, B., Peters, R. J., Vela, J., Lee, Y. J. (2015). Investigation of the Chemical Interface in the Soybean–Aphid and Rice–Bacteria Interactions Using MALDI-Mass Spectrometry Imaging. *Analytical Chemistry*, *87*(10), 5294–5301. http://doi.org/10.1021/acs.analchem.5b00459

Kompauer, M., Heiles, S., & Spengler, B. (2017). Atmospheric pressure MALDI mass spectrometry imaging of tissues and cells at 1.4-mum lateral resolution. *Nature Methods*, *14*(1), 90–96. http://doi.org/10.1038/nmeth.4071

Krapp, A., & Stitt, M. (1995). An evaluation of direct and indirect mechanisms for the “sink-regulation” of photosynthesis in spinach: Changes in gas exchange, carbohydrates, metabolites, enzyme activities and steady-state transcript levels after cold-girdling source leaves. *Planta*, *195*(3), 313–323. Retrieved from http://www.jstor.org/stable/23383277

Lebowitz, R. J. (2011, February 9). The Genetics and Breeding of Coleus. *Plant Breeding Reviews*. http://doi.org/doi:10.1002/9781118061008.ch9

Lee, Y. J., Perdian, D. C., Song, Z., Yeung, E. S., & Nikolau, B. J. (2012). Use of mass spectrometry for imaging metabolites in plants. *Plant Journal*, *70*(1), 81–95. http://doi.org/10.1111/j.1365-313X.2012.04899.x

Lemoine, R., Camera, S. La, Atanassova, R., Dédaldéchamp, F., Allario, T., Pourtau, N., Bonnemain, J.-L., Laloi, M., Coutos-Thévenot, P., Maurousset, L., Faucher, M., Girousse, C., Lemonnier, P., Parrilla, J., & Durand, M. (2013). Source-to-sink transport of sugar and regulation by environmental factors. *Frontiers in Plant Science*, *4*(July), 1–21. http://doi.org/10.3389/fpls.2013.00272

Logan, B. A., Stafstrom, W. C., Walsh, M. J. L., Reblin, J. S., & Gould, K. S. (2015). Examining the photoprotection hypothesis for adaxial foliar anthocyanin accumulation by revisiting comparisons of green- and red-leafed varieties of coleus (Solenostemon scutellarioides). *Photosynthesis Research*, *124*(3), 267-274. http://dx.doi.org/10.1007/s11120-015-0130-0

McCormick, A. J., Cramer, M. D., Watt, D. A. (2006). Sink strength regulates

photosynthesis in sugarcane. *New Phytologist*, *171*(4), 759–770. http://doi.org/10.1111/j.1469-8137.2006.01785.x

McCormick, A. J., Cramer, M. D., Watt, D. A. (2008). Changes in photosynthetic rates and gene expression of leaves during a source-sink perturbation in sugarcane. *Annals of Botany*, *101*(1), 89–102. http://doi.org/10.1093/aob/mcm258

Nemes, P., & Vertes, A. (2007). Laser Ablation Electrospray Ionization for Atmospheric Pressure, in Vivo, and Imaging Mass Spectrometry. *Analytical Chemistry*, *79*(21), 8098–8106. http://doi.org/10.1021/ac071181r

Nielsen, T.H., Krapp, A., Röper-Schwarz, U., Stitt, M. (2002). The sugar-mediated regulation of genes encoding the small subunit of Rubisco and the regulatory subunit of ADP glucose pyrophosphorylase is modified by phosphate and nitrogen. *Plant, Cell & Environment*, *21*(5), 443–454. http://doi.org/10.1046/j.1365-3040.1998.00295.x

Nilsson, A., Goodwin, R. J. A., Shariatgorji, M., Vallianatou, T., Webborn, P. J. H., Andrén, P. E. (2015). Mass Spectrometry Imaging in Drug Development. *Analytical Chemistry*, *87*(3), 1437-1455. http://doi.org/10.1021/ac504734s

Nguyen, P., & Cin, V. D. (2009). The role of light on foliage colour development in coleus (Solenostemon scutellarioides (L.) Codd). *Plant Physiology and Biochemistry*, *47*(10), 934–945. http://doi.org/10.1016/j.plaphy.2009.06.006

Nguyen, P., Quesenberry, K., & Clark, D. (2008). Genetics of growth habit and development of new coleus (Solenostemon scutellarioides (L.) Codd) varieties with trailing habit and bright color. *Journal of Heredity*, *99*(6), 573–580. http://doi.org/10.1093/jhered/esn054

Osorio, S., Ruan, Y.-L., & Fernie, A. R. (2014). An update on source-to-sink carbon partitioning in tomato. *Frontiers in Plant Science*, *5*(October), 1–11. http://doi.org/10.3389/fpls.2014.00516

Paul, M. J., & Driscoll, S. P. (1997). Sugar repression of photosynthesis: the role of carbohydrates in signalling nitrogen deficiency through source:sink imbalance. *Plant, Cell and Environment*, *20*(1), 110–116. http://doi.org/10.1046/j.1365-3040.1997.d01-17.x

Paul, M. J., Driscoll, S. P., & Lawlor, D. W. (1992). Sink-Regulation of Photosynthesis in Relation to Temperature in Sunflower and Rape. *Journal of Experimental Botany*, *43*(2), 147–153. Retrieved from http://dx.doi.org/10.1093/jxb/43.2.147

Paul, M. J., & Foyer, C. H. (2001). Sink regulation of photosynthesis. *Journal of Experimental Botany*, *52*(360), 1383–1400. Retrieved from http://dx.doi.org/10.1093/jexbot/52.360.1383

Robichaud, G., Barry, J. A., & Muddiman, D. C. (2014). IR-MALDESI Mass Spectrometry Imaging of Biological Tissue Sections Using Ice as a Matrix. *Journal of The American Society for Mass Spectrometry*, *25*(3), 319–328. http://doi.org/10.1007/s13361-013-0787-6

Roitsch, T. (1999). Source-sink regulation by sugar and stress. *Current Opinion in Plant Biology*, *2*(3), 198–206. https://doi.org/10.1016/S1369-5266(99)80036-3

Schmidt, M. A., Barbazuk, W. B., Sandford, M., May, G., Song, Z., Zhou, W., Nikolau, B.J., Herman, E. M. (2011). Silencing of Soybean Seed Storage Proteins Results in a Rebalanced Protein Composition Preserving Seed Protein Content without Major Collateral Changes in the Metabolome and Transcriptome. *Plant Physiology*, *156*(1), 330 LP-345. https://doi.org/10.1104/pp.111.173807

Shiea, J., Huang, M. Z., Lee, C.Y., Yuan, C.H., Beech, I., Sunner, J. (2005). Electrospray-assisted laser desorption/ionization mass spectrometry for direct ambient analysis of solids. Rapid Commun. Mass Spectrom., 19: 3701-3704. https://doi.org/10.1002/rcm.2243

Shroff, R., Schramm, K., Jeschke, V., Nemes, P., Vertes, A., Gershenzon, J., & Svatoš, A. (2015). Quantification of plant surface metabolites by matrix-assisted laser desorption-ionization mass spectrometry imaging: Glucosinolates on Arabidopsis thaliana leaves. *Plant Journal*, *81*(6), 961–972. http://doi.org/10.1111/tpj.12760

Smith, C. A., O'Maille, G., Want, E. J., Qin, C., Trauger, S. A., Brandon, T. R., Custodio, D. E., Abagyan, R., Siuzdak, G. (2005). METLIN: a metabolite mass spectral database. *Ther Drug Monit*. Retrieved from http://www.ncbi.nlm.nih.gov/pubmed/16404815

Stein, S. E. (1999). An integrated method for spectrum extraction and compound identification from gas chromatography/mass spectrometry data. *Journal of the American Society for Mass Spectrometry*, *10*(8), 770–781. http://doi.org/10.1016/S1044-0305(99)00047-1

Steyn, W. J., Wand, S. J. E., Holcroft, D. M., & Jacobs, G. (2002). in vegetative tissues : Anthocyanins in unified function a proposed photoprotection. *New Phytologist*, *155*(3), 349–361. http://doi.org/10.1046/j.1469-8137.2002.00482.x

Turgeon, R. (1989). The Sink-Source Transition in Leaves. *Annual Review of Plant Physiology and Plant Molecular Biology*, *40*(1), 119–138. http://doi.org/10.1146/annurev.pp.40.060189.001003

Wardlaw, I. F. (2006). Tansley Review No. 27 The control of carbon partitioning in plants. *New Phytologist*, *116*(3), 341–381. http://doi.org/10.1111/j.1469-8137.1990.tb00524.x

Wu, X., Gu, L., Prior, R. L., & McKay, S. (2004). Characterization of Anthocyanins and Proanthocyanidins in Some Cultivars of Ribes, Aronia, and Sambucus and Their Antioxidant Capacity. *Journal of Agricultural and Food Chemistry*, *52*(26), 7846–7856. http://doi.org/10.1021/jf0486850

Zavalin, A., Yang, J., Hayden, K., Vestal, M., & Caprioli, R. M. (2015). Tissue protein imaging at 1 µm laser spot diameter for high spatial resolution and high imaging speed using transmission geometry MALDI TOF MS. *Analytical and Bioanalytical Chemistry*, *407*(8), 2337–2342. http://doi.org/10.1007/s00216-015-8532-6

Figures

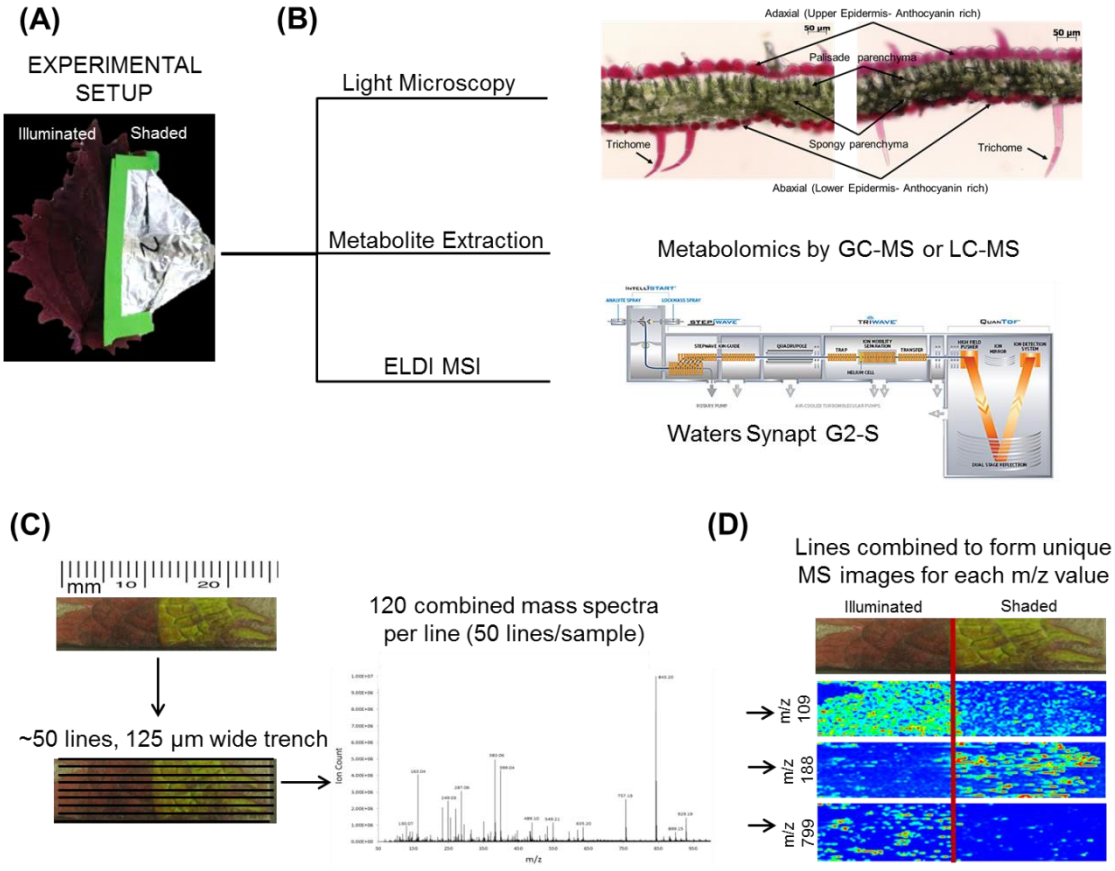

Figure 1. ELDI-MSI experimental workflow. **A)** Individual Coleus leaves were treated for a period of 28 days by shading half the leaf and leaving the other half fully illuminated. **B)** Leaf samples were selected for light microscopy, metabolite extraction and metabolomics analysis, and ELDI-MSI analyses with a Waters Synapt G2-S mass spectrometer. **C)** ELDI-MSI data were generated and validated by metabolite profiling of extracts by GC-MS or LC-MS analysis. **D)** Mass spectrometric images were generated for individual ions and aligned with visual images of leaves.

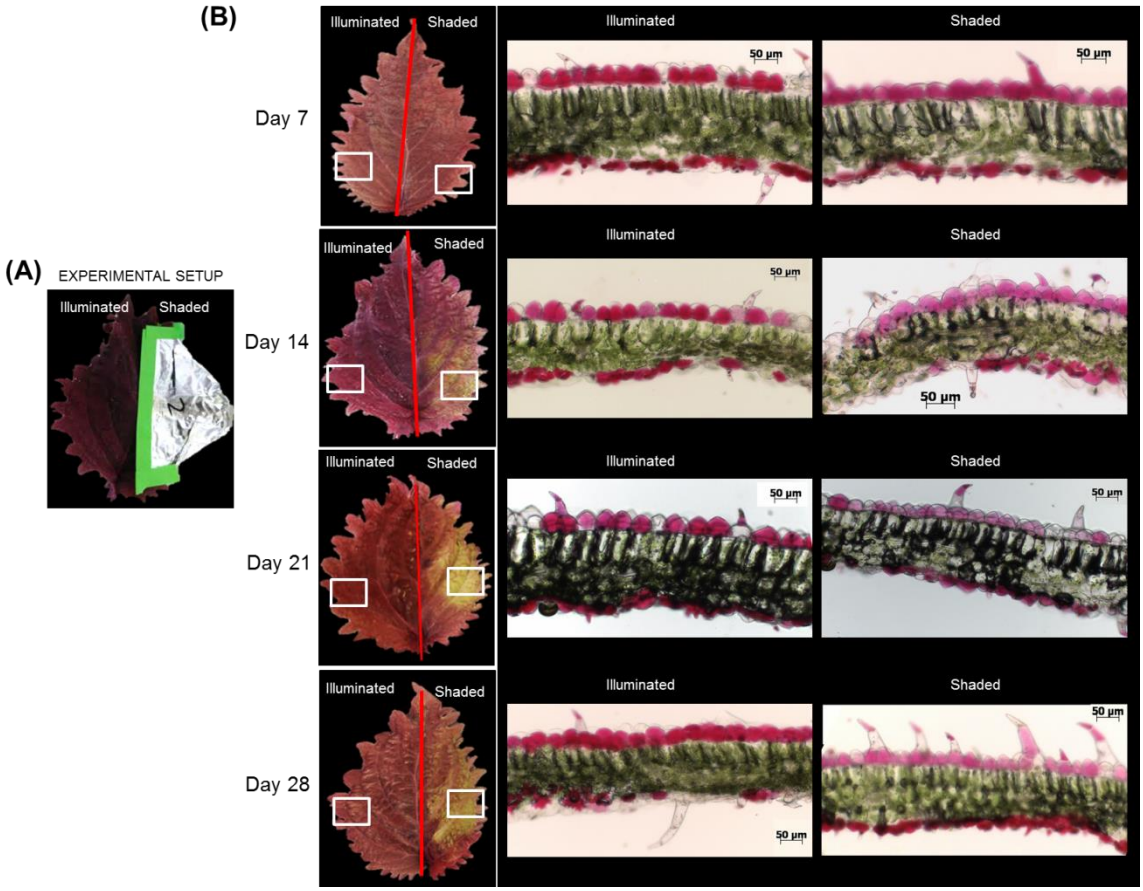

Figure 2. Optical images of Coleus Henna leaves over a 28 day period. **A)** The right-side of each leaf was shaded by wrapping with aluminum foil, whereas the left side was fully illuminated. White boxes denote areas of the leaves that were sectioned for optical microscopic examination in cross section **(B)**. Scale bar = 50 µm

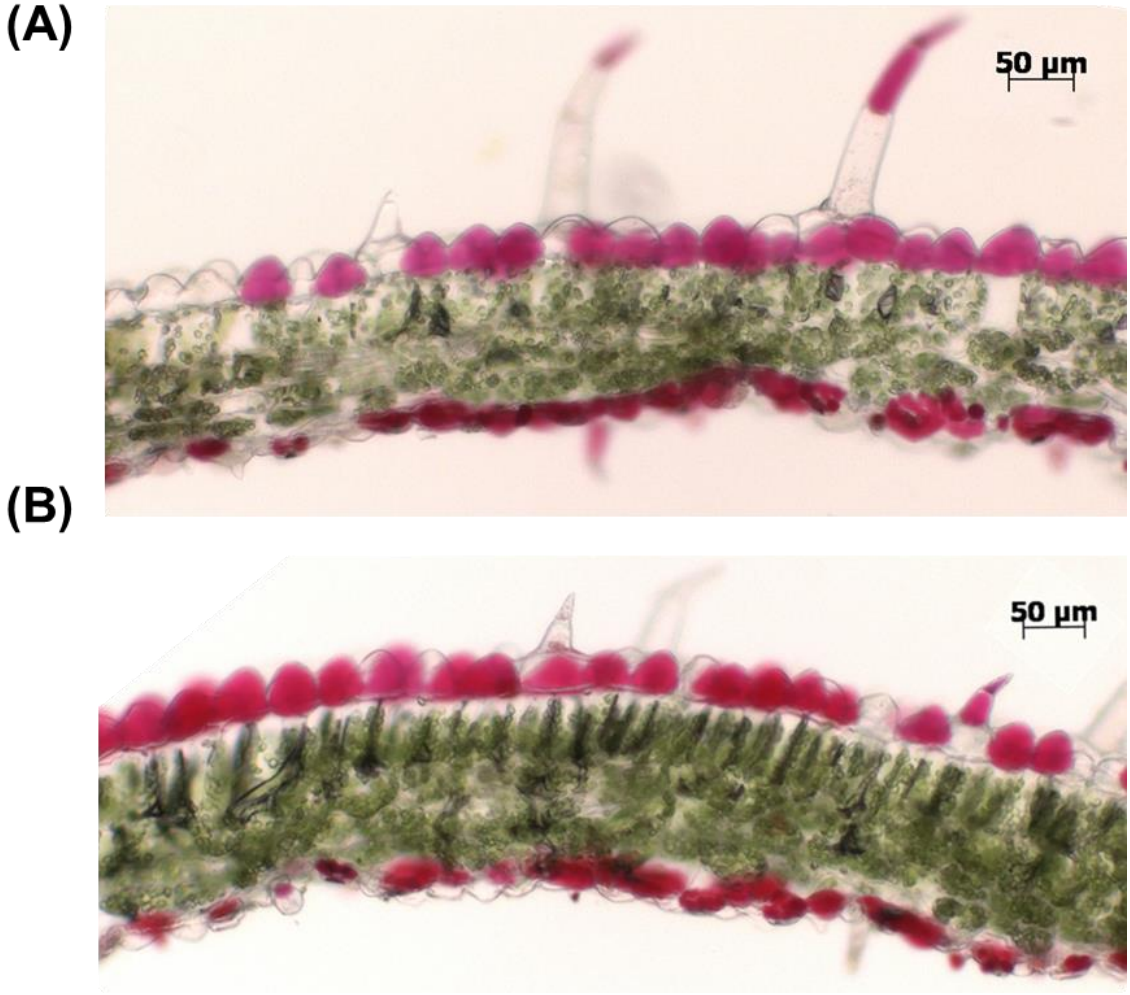

Figure 3. Optical microscopic images of leaf cross sections from the shaded **(A)** and illuminated **(B)** side of a leaf after 7-days of shade treatment. Scale bar = 50 µm

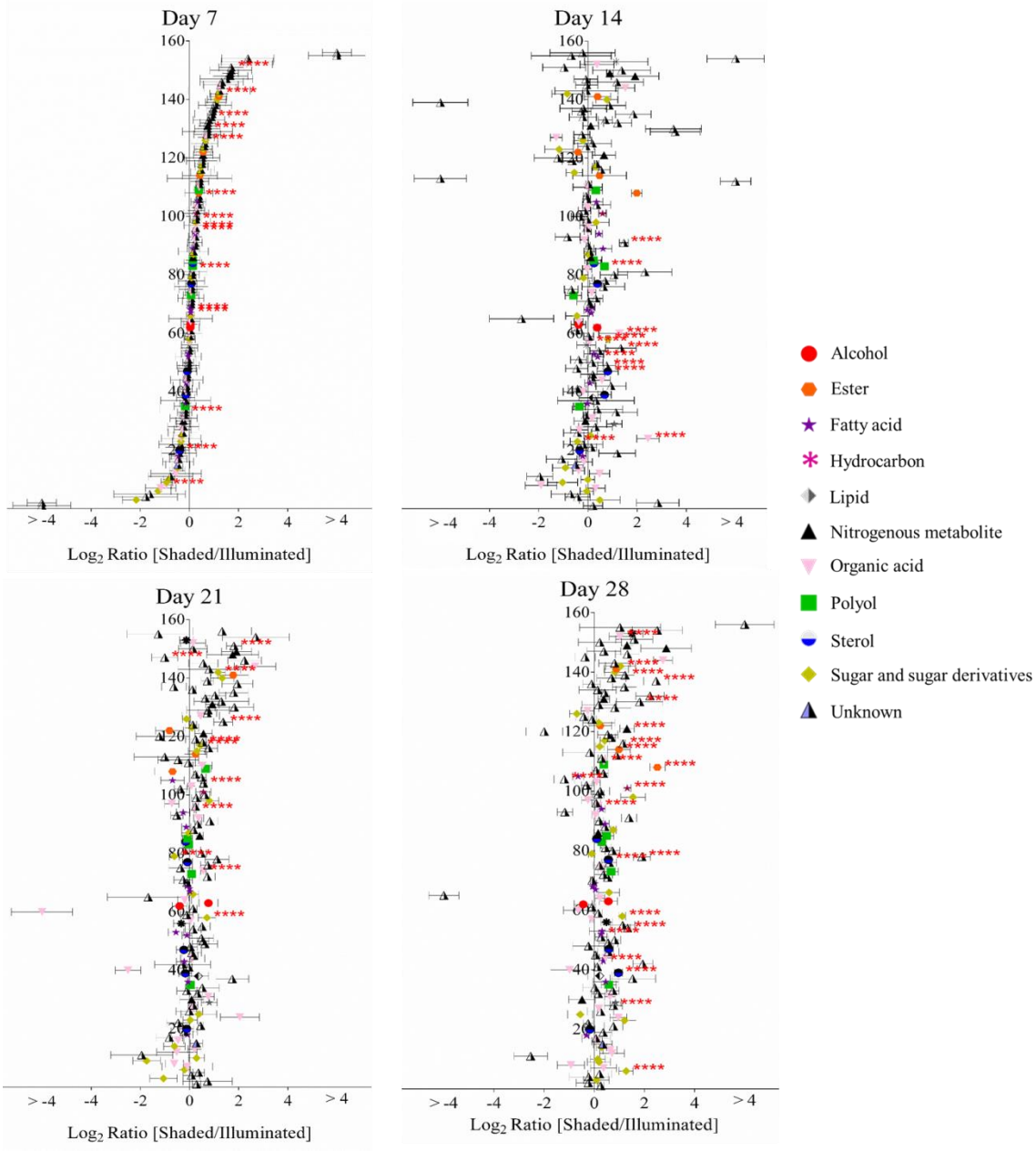

Figure 4. Log-ratio comparison of the differential metabolomes between illuminated and shaded sides of the leaf. The x-axis plots the log-transformed relative abundance ratio of each metabolite in illuminated versus shaded sides. The order of the metabolites (156 analytes, 67 chemically identified) on the y-axis is identical in all four plots, and they are ordered from the lowest to highest value on the x-axis as determined for the 7-day time-point. **** denote p-value <0.05.

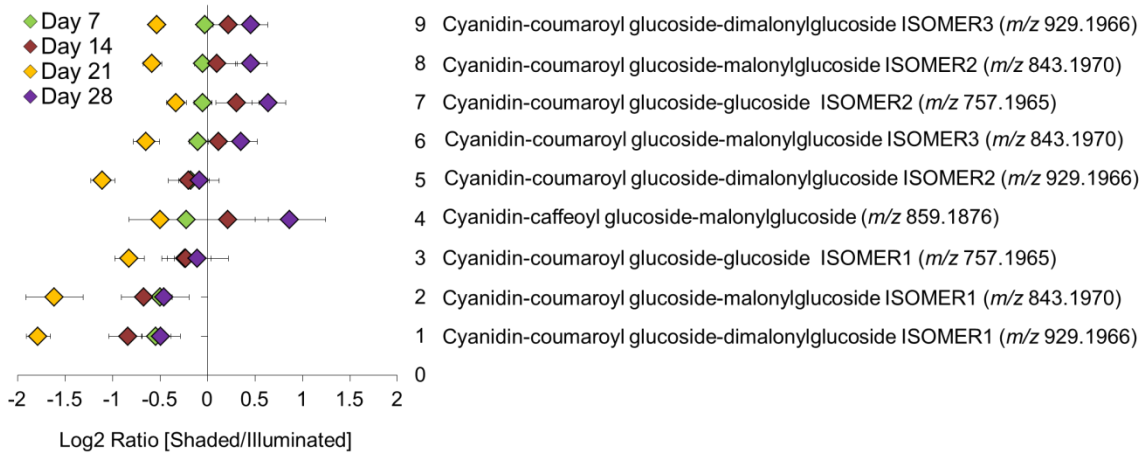

Figure 5. Log-ratio comparison of the differential accumulation of anthocyanins in Coleus half-leaves maintained under full-illumination or shaded for the indicated time-periods. The table names each of the 9 anthocyanins that were identified by LC-MS analysis of extracts prepared from the two leaf halves. The order of the metabolites on the y-axis of the plot is from the lowest to the highest log-ratio values as determined for the 7-day time point.

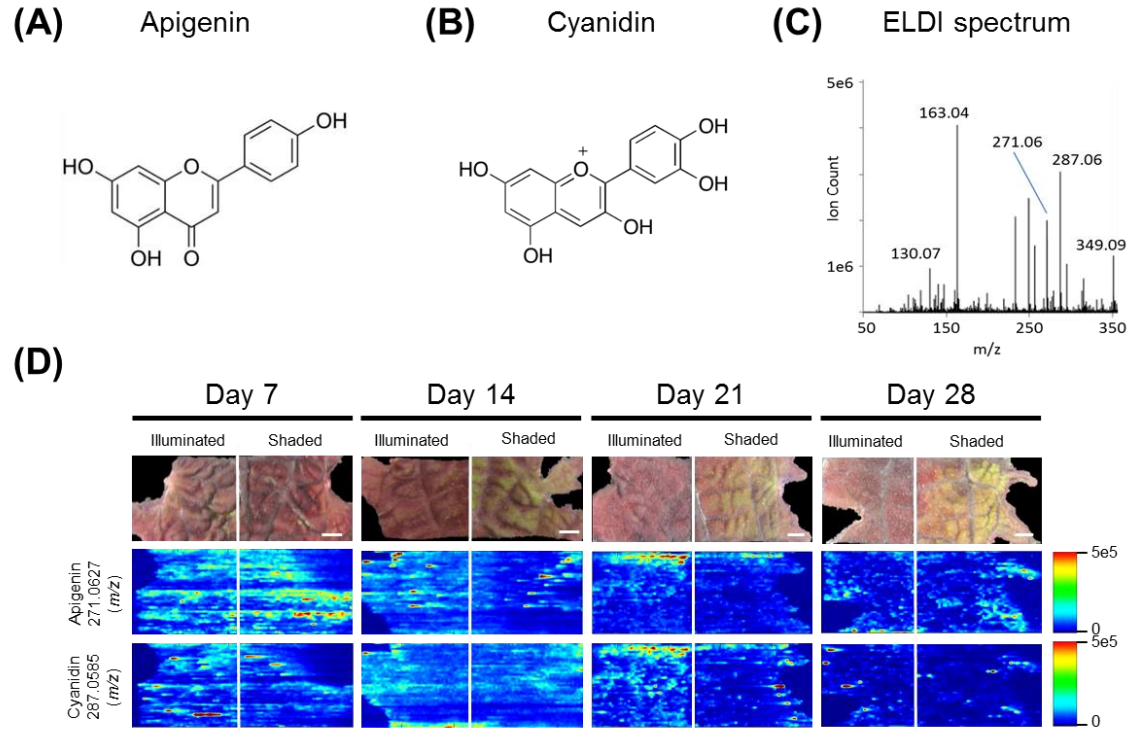

Figure 6. ELDI-MSI analysis of flavonoid backbones. Molecular structure of two aglycone flavonoids: **A)** apigenin; and **B)** cyanidin. **C)** ELDI mass spectrum showing the relative abundance of apigenin ($[M+H]^+$ at *m/z* 271.0627) and cyanidin ($[M]^+$ at *m/z* 287.0585) ions. **D)** Spatial distribution of apigenin and cyanidin in shaded or fully illuminated leaf-halves, at different time-points after initiation of the shading treatment. Scale bar = 2 mm. The MSI intensity scale bar is color coded: red is maximum signal and blue is minimum signal, in this and subsequent figures.

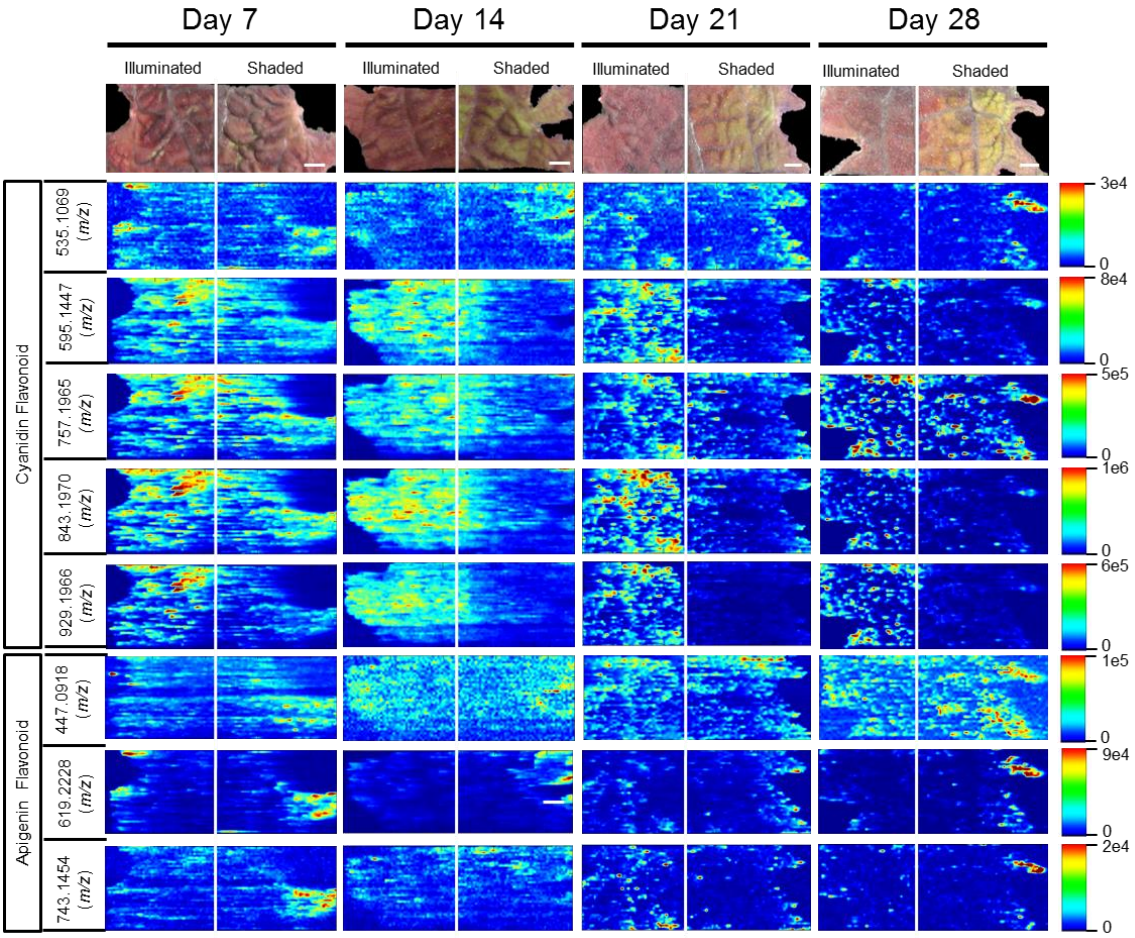

Figure 7. Spatial distribution between shaded and illuminated halves of leaves of cyanidin and apigenin-based flavonoids as affected by up to 28 days of shading. The cyanidin-based flavonoids were detected as $[M]^+$ ions, and apigenin-based flavonoids were detected as either $[M+H]^+$ ions. Scale bar = 2 mm.

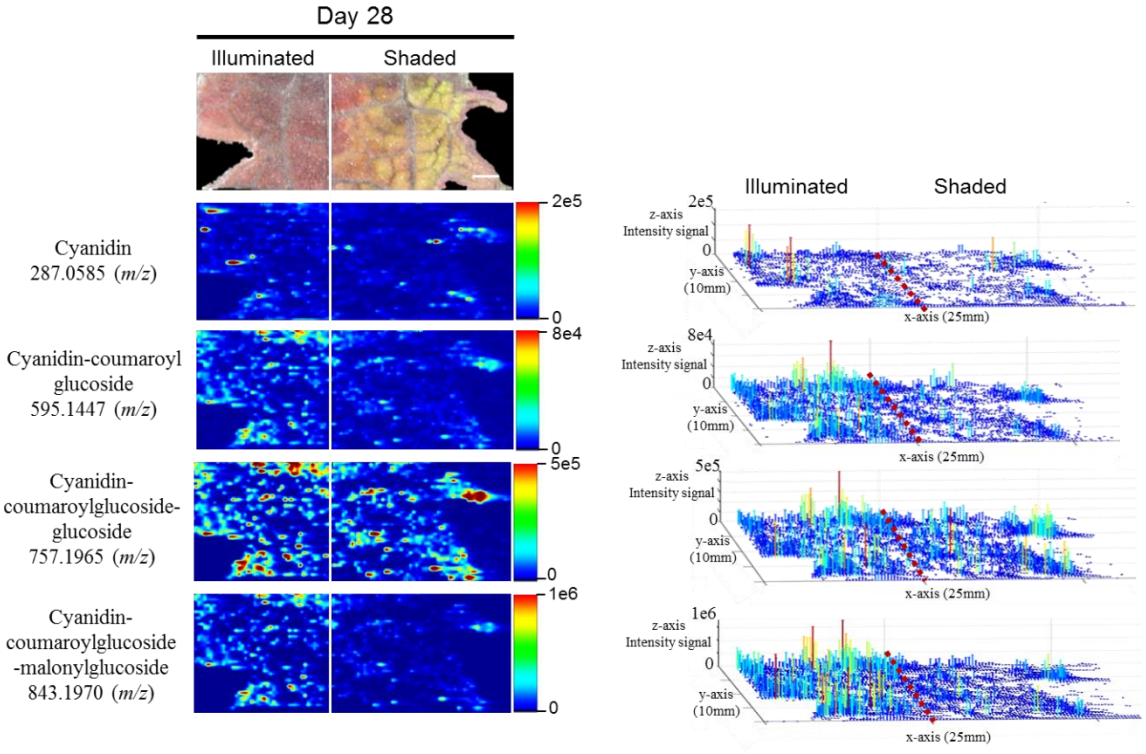

Figure 8. Spatial distributions of cyanidin-coumaroylglucoside-malonylglucoside and its metabolically related species determined by ELDI-MSI analysis of leaf-halves subjected to either full illumination or shaded for up to 28 days. Right panel represents the 3D representations of the abundance of these metabolically related ions. The x- and y-axes represent spatial coordinates (mm), and the z-axis maps ion intensity. Scale bar = 2 mm.

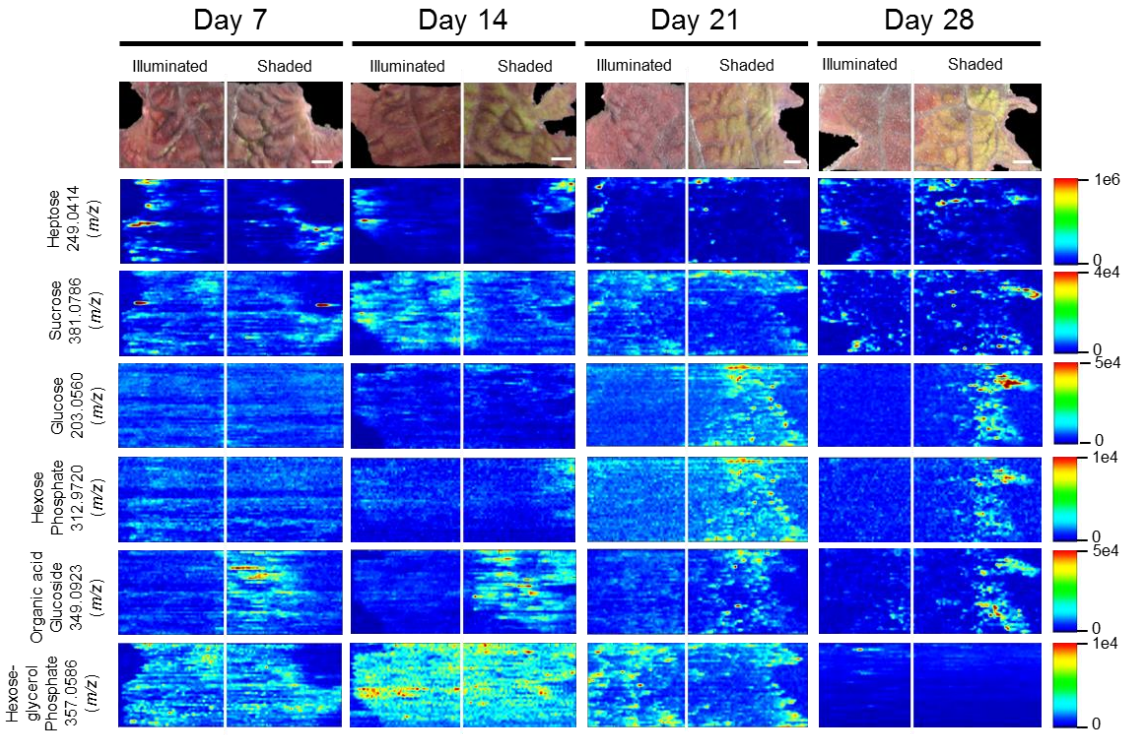

Figure 9. Spatial distributions of sugars determined by ELDI-MSI analysis of leaf-halves subjected to either full illumination or shading for up to 28 days. Each sugar was detected as $[M+Na]^+$ or $[M+K]^+$ adducts. Scale bar = 2 mm.

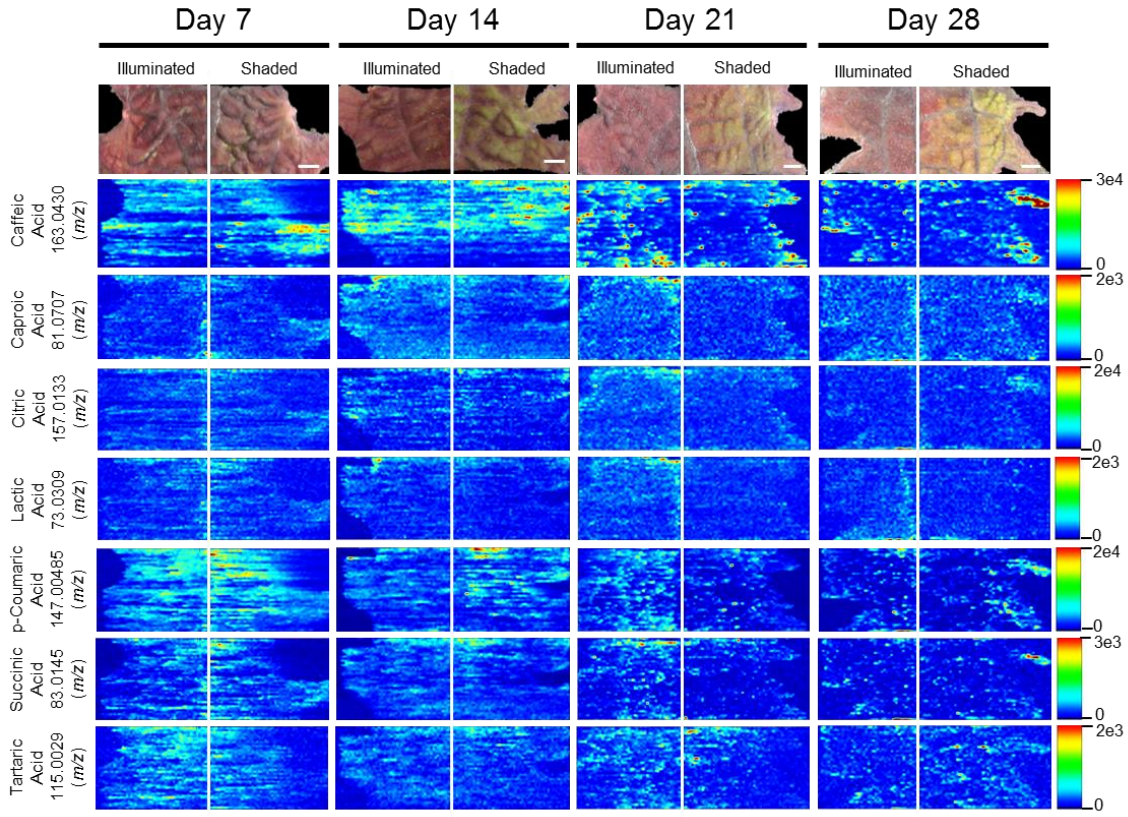

Figure 10. Spatial distributions of organic acids determined by ELDI-MSI analysis of leaf-halves subjected to either full illumination or shading for up to 28 days. Scale bars = 2 mm.

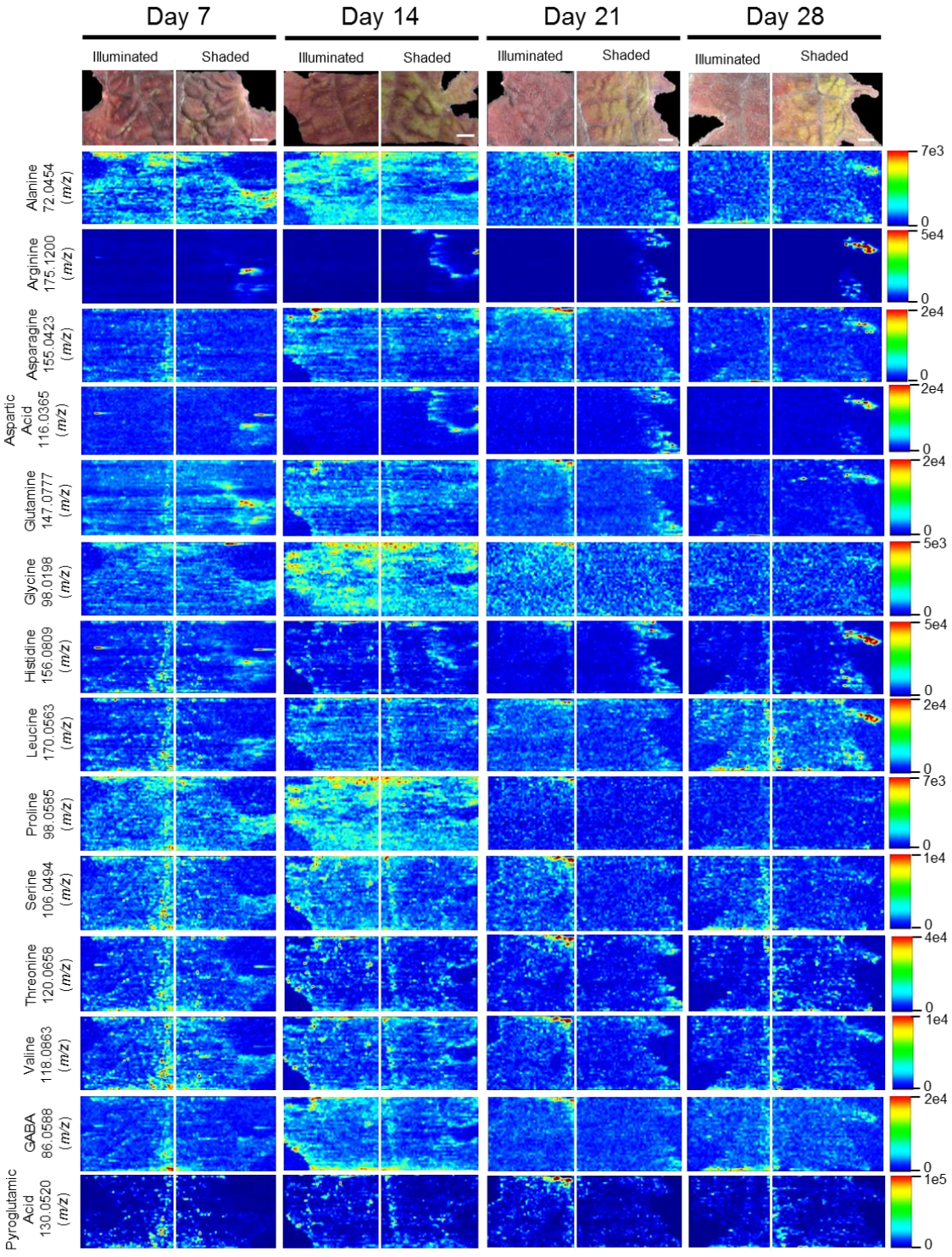

Figure 11. Spatial distribution of amino acids determined by ELDI-MSI analysis of leaf-halves subjected to either full illumination or shading for up to 28 days. Scale bar = 2 mm.

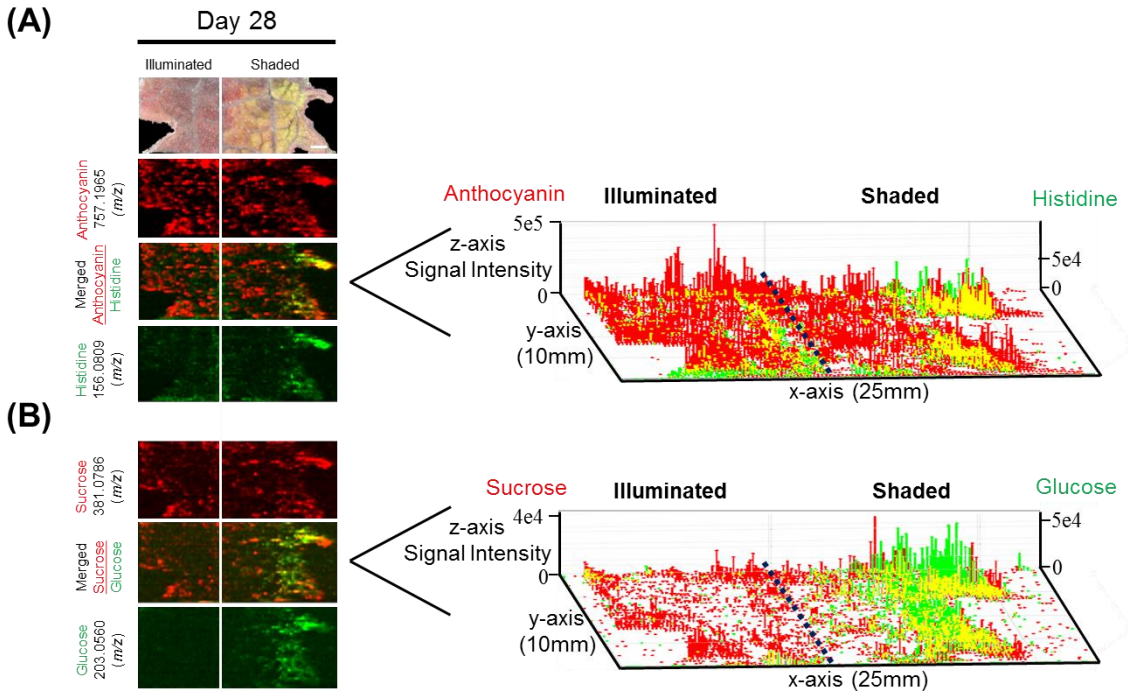

Figure 12. 3D representation of the localization of UV-absorbing and non-UV absorbing metabolites. Distributions of **A)** anthocyanin 757.1965 (*m/z*) (red) along with histidine 156.0809 (*m/z*) (green) and **B)** sucrose 381.0786 (*m/z*) (red) along with glucose 203.0560 (*m/z*) (green) are shown. Scale bar = 2 mm. Right panel represents the 3D representations of the abundances of these metabolically related ions. The x- and y-axes represent spatial coordinates (mm), and the z-axis maps ion intensity.

Table 1. Flavonoids identified by ELDI-MS. Peak assignments were based on matches with entries in the METLIN Database (Smith et al., 2005).

High Res. *m/z*	Assigned ID	Δppm of ID	Response to Shading	Major Fragment Ions	Signal Intensity
255.0679	Catechine + H^+ -$2H_2O$	6	None	Background interferences	5e4
271.0627	Apigenin + H^+	9	None	243, 229, 225, 156, 145, 119	1e6
287.0585	Cyanidin (M^+)	12	None	269, 241, 213, 185, 157, 137	7e5
291.0899	Catechine + H^+	12	None	Too low abun.	2e4
399.0434	Flavone + K^+	10	None	381, 371, 353, 337, 287, 219, 201, 175	1e6
441.0725	Cyanidin Flavonoid + (M^+) +H^+	3	None days 7-14, decreased days 21-28	287	2e5
447.0918	Apigenin Glucuronide + H^+	0.4	None	271, 163	7e5
458.0823	Flavone + $2H^{2+}$	4	None	399, 371, 353, 219, 163, 147	8e4
476.0907	Cyanidin-coumaroyl glucoside-dimalonylglucoside (M^+) + Na^+	6	Decreased	287	7e4
483.0781	Cyanidin Flavonoid (M^+)		None	287, 203, 163, 147	8e5
489.1057	Apigenin Flavonoid + H^+ OR + H^+ - H_2O	4	None days 7-21, decreased day 28	471, 399, 271, 163	5e5
505.1016	Flavone Glucoside + H^+– H_2O	6	None		5e4
511.0744	Cyanidin Flavonoid (M^+)		Decreased	437, 353, 313, 287, 271, 179	7e4
527.0515	Cyanidin Flavonoid (M^+)	3	Decreased	369, 309, 287, 163	1e5
533.2350	Flavonoid		None	287, 271, 219, 201, 163, 147	2e5
535.1069	Cyanidin malonylglucoside (M^+)	2	None days 7-21, decreased day 28	287, 163	6e4
549.2095	Cyanidin Flavonoid (M^+)		None	369, 331, 287, 271, 219, 201, 163, 147	2e5
557.0940	Flavonoid + Na^+	6	None	Interference from mass lock	8e4
593.1339	Flavonoid + H^+– H_2O	7	None	Too low abun.	2e4
595.1447	Cyanidin coumaroylglucoside (M^+)	0.1	Decreased	549, 287, 163, 147	3e5
619.2228	Apigenin Flavonoid + H^+		Increased	575, 533, 271, 163	2e5
635.2041	Apigenin Flavonoid + H^+		Increased	591, 549, 271, 163	4e5
697.1607	Flavonoid + H^+	0.4	Decreased	Too low abun.	1e4

Table 1. Continued

743.1454	Apigenin Flavonoid + H^+		None	271, 163, 147	4e4
757.1965	Cyanidin-coumaroylglucoside-glucoside (M^+)	1	None	595, 449, 399, 287, 271, 163, 147	8e5
773.1890	Flavonoid + H^+	4	None	Too low abun.	1e4
787.2041	Flavonoid + H^+	4	None	Too low abun.	2e4
799.2031	Cyanidin Flavonoid $M^+ - H_2O$ or $M^+ - 2H_2O$	0.1-6	Decreased	621, 595, 535, 527, 441, 287, 163, 147	7e4
813.1613	Cyanidin Flavonoid (M^+)		None	795, 287, 163	7e4
827.1994	Flavonoid + H^+	4-5	Decreased	Too low abun.	2e4
829.1490	Cyanidin Flavonoid (M^+)		None	595, 287, 271, 163, 147	5e4
843.1970	Cyanidin-coumaroyl glucoside-malonylglucoside (M^+)	0.4	Decreased	799, 595, 535, 287, 163, 147	4e6
859.1876	Cyanidin-caffeoylglucoside-malonylglucoside (M^+)	5	Decreased	843, 489, 287, 271, 163	7e4
865.1617	Flavonoid + $H^+ - H_2O$	0.1-7	Decreased	839, 821, 677, 635, 617, 575, 531, 513	1e5
873.2090	Cyanidin Flavonoid (M^+)	0.6+	None	843, 693, 595, 535, 489, 287, 163, 147	5e4
883.1759	Dicatechine Flavonoid + H^+	4	None	865, 839, 821, 677, 635, 617, 575, 531, 513	2e5
885.2034	Flavonoid		Decreased	867, 595, 577, 287, 271, 163, 147	9e4
899.1660	Dicatechine Flavonoid + H^+	0.5	None	881, 855, 837, 813, 693, 651, 633, 591, 547	3e5
929.1966	Cyanidin-coumaroyl glucoside-dimalonylglucoside (M^+)	1	Decreased	843, 621, 595, 489, 287, 163, 147	1e6
951.1619	Cyanidin Flavonoid (M^+)		Decreased	865, 843, 741, 635, 549, 489, 447, 399, 287	5e4

Table 2. Carbohydrates identified by ELDI-MS. Peak assignments were based on matches with entries in the METLIN Database (Smith et al., 2005).

High Res. m/z	Assigned ID	Δppm of ID	Response to Shading	Major Fragment Ions	Signal Intensity
159.0021	Tetrose + K^+	20	None	Localized Signal	8e4
189.0158	Pentose + K^+	0.1	None	Localized Signal	3e4
197.0433	Organic Acid Glucoside + H^+ + Na^+	0.01	None	161, 145, 119, 101	1e6
203.0560	Hexose (glucose) + Na^+	16	No abundance day 7, increased days 14-28	185, 167, 157, 137, 123, 111	1e3 - 5e5
219.0310	Hexose (glucose) + K^+	20	No abundance day 7, increased days 14-28	201, 183, 151, 123, 111	5e3 - 6e5
233.0671	Heptose + Na^+	16	None	215, 205, 179	5e5
249.0414	Heptose + K^+	17	None	231, 213, 195, 125	4e5
255.1064	Hexose-glycerol + H^+	4	None	Too low abun.	1e4
277.0901	Hexose-glycerol + Na^+	0.1	None	Background interferences	5e4
312.9720	Hexose-Phosphate + K^+	0.01	Low abundance day 7, increased days 14-28		3e3 – 9e4
337.0585	Caffeoylglucarate + H^+ - $2H_2O$	5	None	319, 185, 163	7e4
349.0923	Organic Acid Glucoside + Na^+	8	Increased	331, 313, 267, 163, 149	9e4
357.0586	Hexose-glycerol Phosphate + Na^+	8	None, decreased in abundance day 28		4e3 – 1e5
365.0647	Organic Acid Glucoside + K^+	3	Increased	347, 333, 329, 163	1e5
365.1064	Sucrose + Na^+	2	None	347, 337, 319, 203	5e4
371.0475	Galloylglucose + K^+	26	None	353, 327, 237, 219	1e5
381.0786	Sucrose + K^+	2	None	363, 345, 335, 219, 163, 147	7e4

Table 3. Amino acids and organic acids identified by ELDI-MS. Peak assignments were based on matches with entries in the METLIN Database (Smith et al., 2005).

High Res. m/z	Assigned ID	Δppm of ID	Response to Shading	Major Fragment Ions	Signal Intensity
72.0454	Alanine + H^+ - H_2O	6	None	Too low m/z	7e3
73.0309	Lactic Acid + H^+ – H_2O	26	None	Too low m/z	1e4
81.0707	Caproic Acid + H^+ – $2H_2O$	3	None	Too low m/z	1e4
83.0145	Succinic Acid + H^+ -$2H_2O$	7	None	Too low m/z	8e3
86.0588	GABA + H^+ - H_2O	20	None	Too low m/z	3e4
98.0198	Glycine + Na^+	14	None	Too low abun.	6e3
98.0585	Proline H^+ - H_2O	21	None	Too low abun.	9e3
106.0494	Serine + H^+	4	None	88	1e4
114.0907	Leucine + H^+ – H_2O	10	None	Background interferences	1e3 – 2e5
115.0029	Tartaric Acid + H^+ – $2H_2O$	6	None	Localized Signal	2e4
116.0365	Aspartic Acid + H^+ – H_2O	14	Increased	88	3e4
118.0863	Valine + H^+	~0	None	100, 72	3e4
120.0658	Threonine + H^+	2	None	102	6e4
129.0346	p-Coumaric Acid + H^+-$2H_2O$	~0	None	119, 91	2e4
130.0520	Pyroglutamic Acid + H^+	16	None	84	4e5
145.0322	Caffeic Acid + H^+ - $2H_2O$	18	None	135, 117, 107, 89, 79	1e5
147.0485	p-Coumaric Acid + H^+-H_2O	26	None	119, 91	4e5
147.0777	Glutamine + H^+	8	None days 7-21, Increased day 28	130, 84	2e4
155.0423	Asparagine + Na^+	2	None	109	2e4
156.0809	Histidine + H^+	26	None days 7-14, Increased days 21-28	110, 93, 83	5e4
157.0133	Citric Acid + H^+ – $2H_2O$	6	None	Too low abun.	9e3
163.0430	Caffeic Acid + H^+-H_2O	20	None	145, 135, 117, 107, 89, 79	8e5
170.0563	Leucine + K^+	8	None	124	5e4
175.1200	Arginine + H^+	5	Increased	158, 130, 116, 112, 70	1e5
219.0019	Caffeic Acid + K^+	16	None	201, 183, 173, 161, 129	3e5
230.9883	Citric Acid + K^+	6	None	213, 195	2e4

CHAPTER 4.

LOCALIZING AMINO ACID KINETICS IN PLANTS USING MASS SPECTROMETRY IMAGING OF STABLE ISOTOPES

Patrick A. McVey[1,2], Xinyu Fu[3,4], Basil J. Nikolau[3,4], R.S. Houk[1,2]

[1] *Department of Chemistry, Iowa State University, Ames, IA, USA*

[2] *Ames Laboratory-US DOE, Ames, IA, USA*

[3] *Center for Metabolic Biology, Iowa State University, Ames, IA, USA*

[4] *Roy J. Carver Department of Biochemistry, Biophysics and Molecular Biology, Iowa State University, Ames, IA, USA*

Abstract

Mass spectrometry imaging (MSI) of plants has shown its worth to the field of metabolomics. Many methods have been introduced for MSI of plants, each with their own advantages and drawbacks. In the current work, we present electrospray laser desorption ionization (ELDI) MSI as an ionization source to study distributions of amino acids in Arabidopsis plants. ELDI does not require sample preparation and operates at atmospheric pressure, which is ideal for analysis of biological tissues. The spatial resolution of ELDI-MSI was improved to 50 µm for higher resolution MS-images. Arabidopsis plants grown in a 10 mM ^{13}C glucose solution were analyzed via ELDI-MSI.

Thirteen amino acids were detected and imaged in Arabidopsis plants, with their isotopic morphologies interrogated.

Introduction

Electrospray laser desorption ionization (ELDI) is an atmospheric pressure ionization source requiring little to no sample preparation.[1] This makes ELDI a desirable method to analyze plants in their native environment without any alterations to the sample surface.[2,3] One drawback of ELDI is its relatively low spatial resolution reported for mass spectrometry imaging (MSI) compared with similar methods.[4] The well-established matrix-assisted laser desorption ionization (MALDI) MSI is effective in analyzing plants, even at high resolutions of <5 µm, but requires extensive sample preparation and usually operates under vacuum.[5,6,7]

Another laser-based MSI method known as laser ablation electrospray ionization (LAESI) has been shown at near sub-cellular resolutions.[8,9] However, LAESI requires a modified system for these higher resolutions and was limited to very large cells (>50 µm). A commercial LAESI source (Protea) is available with 200 µm lateral resolution. LAESI has been shown to provide information on biological processes but has not been demonstrated at high spatial resolution.[10,11]

Previous studies have shown ELDI-MSI at spatial resolutions of 125 µm for plants while detecting carbohydrates, amino acids, and flavonoids.[12] In the current work, the lateral resolution was improved to 50 µm for ELDI-MSI on Arabidopsis plants. Since the cotyledon of the Arabidopsis was less than 1 mm in diameter, higher resolution MSI was

needed than currently demonstrated with LAESI or ELDI. With a 50 µm resolution via ELDI-MSI the spatial distributions of amino acids in Arabidopsis plants were interrogated. To show the sensitivity of ELDI-MSI at higher resolution and its applicability to study biological processes, Arabidopsis plants were grown in a ^{13}C isotopically labeled glucose solution. The isotopically labeled carbons were observed in all detected amino acids and their distributions were shown via ELDI-MSI. Plants from each batch were also analyzed via GCMS polar extractions and compared to ELDI-MSI data. Both methods were adept at detecting isotopically labeled amino acids.

Experimental

Plant Growth

Arabidopsis thaliana seeds of the wild-type (ecotype Col-0) were obtained from the Arabidopsis Biological Resource Center (http://abrc.osu.edu/). Arabidopsis seeds were sterilized with 50% bleach solution containing 0.1% Tween 20 for 7 minutes, followed by extensive washes with sterile water before sowing. Seeds were germinated in 125 mL sterile Erlenmeyer glass flask containing 50 mL half-strength Murashige and Skoog (1/2 MS) liquid media supplemented with10 mM glucose (pH 5.7, adjusted with 1M KOH). Liquid-culture flasks were arranged in a randomized complete block design on a platform shaker (120 rpm) under constant light and temperature (23°C). After 14 days, seedlings were switched rapidly from unlabeled to carbon-13-labeled media (1/2 MS liquid media containing 10 mM [U-$^{13}C_6$] glucose) at multiple time points. Seedlings were incubated in the labeled media for various time intervals (0, 7, and 14 days) after the

isotope switch. Subsequently, seedlings were collected from the culture flasks and washed three times using 1/2 MS liquid media before analysis.

Metabolite Extraction

Intracellular metabolites were extracted using the methanol:chloroform:water extraction protocol described previously.[13] The lyophilized tissue samples were homogenized in pre-chilled Eppendorf tubes using a Retsch MM301 5 mm ball mill mixer at a frequency of 30 Hz for 1 min. Two mg of dry weight of powdered samples spiked with internal standards (10 µg of norleucine and 5 µg nonadecanoic acid) was extracted using 0.35 ml of hot methanol and incubated at 60 °C for 10 min. The methanol extract was vortexed for 10 sec and sonicated for 10 min at full output power. Liquid-phase extraction was performed by 0.35 ml of chloroform and 0.3 ml of water. Aliquots of 200 µl upper methanol-water layer (polar fraction) and 200 µl bottom chloroform layer (non-polar fraction) were obtained after centrifugation for 5 min at 13,000 g. The aliquots were separately transferred to glass vials, dried by vacuum concentration (Speed-Vac concentrator SVC 100H, Savant, NY), and stored − 80 °C until GCMS analysis.

GCMS conditions

Amino acids were derivatized by N-(tert-butyldimethylsilyl)-N-methyltrifluoroacetamide (TBDMS) before separation by gas chromatography (GC) following the protocols adapted from Young.[14] The dried polar fraction samples were

dissolved in 50 µL anhydrous pyridine and 70 µL TBDMS derivatization reagent. Each sample then was sonicated for 5 min and incubated at 60 °C for 30 min. The derivatized samples were analyzed by a Agilent 6890 series gas chromatograph equipped with a HP-5ms column (30 m x 0.25 mm x 0.25 µm, Agilent) and coupled to an Agilent 5973 quadrupole mass detector. All analyses were run in split mode (1:2 or 1:5 split ratio), with an injection volume of 1 µL. Helium was used as a carrier gas with the flow rate of 1 mL min^{-1} and the inlet temperature was 280°C. The oven temperature was programmed as follows: 140°C for 2 min, ramped at a 10 °C/min to 280 °C, followed by a 20 °C/min ramp to 320 °C, and finally held at this temperature for 2 min. The MS quadrupole temperature was 150°C, and the source temperature set at 230°C. Positive electron ionization mass spectra at 70 eV were recorded using the scan mode for mass to charge ratio (m/z) between 200 and 500. GCMS peak integration was done using ChemStation, and isotope correction was done using Isocor.

ELDI-MS

A Waters Synapt G2-S quadrupole time-of-flight mass spectrometer was used for data collection for all ELDI-MSI. The Waters ESI source was removed and a homemade open-air ESI source was used with samples at atmospheric pressure. Data were acquired in the mass range from *m/z* 50 to 600, spectra were summed for 0.25 seconds. The time-of-flight reflectron operated in single-pass mode with a resolution of ~10,000 FWHM for MS images. The TOF was then operated in double-pass mode with a resolution of ~40,000 FWHM, or “high resolution mode”, to confirm compound

identifications by accurate m/z measurements. These confirmatory measurements were done on different plants from the same treatment batch. The Synapt was operated using Waters MassLynx V4.1 (SCN851) software.

Data Handling

Spectra were generated from total ion chromatograms (TIC) combined by the MassLynx software. The ".raw" Waters data files were converted to mzML files by Proteowizard Mass Converter Tool. The MzML files were then combined into an imzML file using imzML Converter. This combined image file was then viewed and images were generated from MSiReader V0.06 via the W.M. Keck FTMS Laboratory. All images made within MSiReader had Linear2 interpolation for image clarity, and used the "Jet" colormap/false color appearance.

ELDI Source

The ELDI ion source setup has been described.[12] Samples were ablated with a Nd:YAG laser (ULTRA, Big Sky Laser Tech, Inc. Bozeman, MT). The third harmonic was used at 355 nm. The laser was operated at a pulse repetition rate of 10 Hz, with a 5 ns pulse width, and an energy of ~250 µJ/pulse (before focusing). The beam was focused onto the sample by a beam expander followed by a single plano-convex focusing lens (fused-silica focal length 75 mm), with a nominal spot size of ~50 µm.

Entire Arabidopsis plant samples were mounted on a glass slide using double sided tape. The laser did not penetrate completely through the sample; the underlying

tape is not ablated. No matrix was applied, and leaves were pressed lightly to create an even surface. Plant samples were then placed 8 mm below the ESI-sample inlet axis on a computer-controlled translation stage (Z825B, Thorlabs, Inc. Newton, NJ). Samples were translated at 0.4 mm/sec beneath the 10 Hz laser beam down the surface of the leaf to ensure fresh tissue was constantly being ablated. The distance between the centers of adjacent ablation tracks was 50 µm, providing a lateral resolution of 50 µm. The leaves were irradiated normal to the sample surface with the laser beam axis ~2 mm downstream from the ESI capillary. The ESI tip was ~10 mm from the sample inlet.[12]

A solution of 50% methanol with 0.1% formic acid (99.5% purity, Fisher Scientific) was pumped through a 53 µm ID polyimide coated capillary as the ESI solution (pump: model Z2, Harvard Apparatus, South Natick, MA). Leucine enkephalin was added at 0.1 ppm to the ESI solution for use as a mass calibrant. All data were acquired in positive ESI mode. The ESI voltage for ELDI was +2.5 kV applied to a stainless steel union in the liquid flow line, with the sample cone completing the ESI circuit. The sample inlet was kept at 100^{o} C with a N_2 curtain gas flow of 1 L/hr.

Results and Discussion

GCMS Profiles of Amino Acid Isotopologues

Arabidopsis plants grown in ^{13}C glucose solution were analyzed by a total metabolite analysis with GCMS. Plant samples were collected after 7 days and 14 days in the isotopically labeled glucose solution. The GCMS profiles of eleven amino acids and their isotopes can be seen in **Figure 1**. These include Alanine, Aspartate, GABA,

Glutamate, Glutamine, Glycine, Leucine, Proline, Pyroglutamic Acid, Serine, and Valine. For most of the amino acids detected there was substantial isotopic enrichment from the ^{13}C glucose. Two additional amino acids (Arginine and Threonine) were detected by ELDI-MSI but GCMS profiles weren't detected.

The GCMS profiles of the eleven amino acids shown in **Figure 1** are discussed below in alphabetical order. Alanine was observed from M+0 to M+2, with the greatest increase in the M+2 isotope after 7 days, nearly in equal abundance with the M+0 peak. After 14 days, the enrichment of the M+2 peak was much less compared to the 7-day sample. The Aspartate isotopic profile was nearly identical between the 7-day and 14-day samples, with the M+1 isotope about one-third the intensity of the M+0 peak. The abundance steadily dropped as the isotopes increased in m/z. GABA had a very similar profile to Aspartate. Glutamate had a slight increase in the M+1 and M+2 isotopes after 14-days as compared to the 7-day samples. Overall, however, it had a similar profile to both Aspartate and GABA.

Glutamine had substantial enrichment, with the M+0 peak only accounting for about half the overall Glutamine signal. The 7-day samples had a similar abundance across all five isotopes, but the 14-day samples had a slight decrease as more ^{13}C was added. Glycine had the opposite outcome, as the 7-day samples showed more enrichment of the M+1 peak compared to the 14-day samples. However, as the error bars indicate in **Figure 1**, this varied across the 7-day samples.

Leucine had about twice the enrichment after 14-days compared with the 7-day samples. However, the M+5 isotope was similar in abundance for both. Proline had a

similar relative abundance for the M+0 peaks. While the 14-day samples had more enrichment of the M+1 and M+2 isotopes the 7-day samples had a greater enrichment for the M+3 and M+4 isotopes, although this effect was slight. A similar pattern is seen for the Pyroglutamic Acid isotopes, with the 14-day samples having greater M+1 enrichment, but the 7-day samples having greater M+5 enrichment. However, this also varied across samples.

Serine had substantial enrichment, with the M+1 isotope approximately half as intense as the M+0 peak for the 7-day samples. The M+2 isotope was only slightly less abundant than the M+1 isotope. Valine had a similar pattern to Leucine, with slight isotopic enrichment from the M+1 to M+4 isotopes.

ELDI-MSI of Amino Acids

Concurrent with the GCMS, plant samples from the same batches were taken for MSI analysis. Thirteen amino acids were imaged by ELDI-MSI with their detected m/z values shown in **Table 1**. For all MS-images (**Figure 2**) the first two plants in the optical images (from left to right) were grown in a ^{12}C glucose solution, so no isotopic enrichment should be observed. The two plants on the right were grown in the ^{13}C-labeled glucose solution for 7 days (left) or 14 days (right).

Alanine (**Figure 2**) was mostly observed spread throughout the cotyledon of the plants. There was a slightly higher relative isotopic abundance in the 7-day samples. Also, there is more abundance in the hypocotyl and roots in the isotopically labeled plants. Signal from the root was greatest from the M+2 isotope for 7-day plants and was

much higher compared with the M+1 isotope. Arginine (**Figure 2**) had a very concentrated abundance in all plants. However, it seemed to become more pronounced throughout the cotyledon in the isotopically labeled samples, especially after 14 days of enrichment. The control plants had more abundance in the roots as compared with the labeled plants. The relative intensity of the M+0 through the M+3 isotopes were nearly equal in the 7-day samples and dropped only slightly in the M+4 and M+5 isotopes. The day-14 samples did not have a high signal from the M+0 peak, and the M+1 through M+5 isotopes were all very close in abundance. Arginine was not observed by GCMS.

Aspartate (**Figure 3**) was only observed up to M+2 for the isotopically labeled samples. The abundance was mostly observed in the cotyledon, although some Aspartate was seen in the hypocotyl and root. The maximum relative abundance for the M+1 isotope in the labeled plants was nearly equal to the M+0 signal from the control plants. GABA (**Figure 3**) was observed throughout the plant but was also concentrated mostly in the cotyledon. The M+1 through M+3 isotopes were all observed in similar abundance for both the 7-day and 14-day samples, while the M+4 isotope had a slight drop in abundance.

Glutamate (**Figure 4**) was observed throughout the plant, mostly concentrated in the cotyledon. However, some highly localized Glutamate signal was seen in the hypocotyl and root in the 7-day samples. The 7-day plants had the greatest signal intensity observed for the M+5 isotope. This differs from the GCMS data. The 14-day plants had an increasing relative signal as the isotopic enrichment increased, with a slight drop for the M+5 isotope.

Glutamine (**Figure 5**) was very localized in the control plants and was observed more in the root than the hypocotyl, with some abundant localized spots in the cotyledon. Glutamine was much more abundant and spread throughout the cotyledon in the isotopically labeled plants. There was a similar abundance for both the 7-day and 14-day plants for the M+2 through M+5 isotopes. This observation is similar to the GCMS profile.

Glycine (**Figure 6**) was most abundant in the cotyledon, though some signal was observed in the hypocotyl and root. The maximum relative abundance of the control M+0 peak was similar to that of the labeled plants. Leucine (**Figure 6**) (or isoleucine) was observed from the M+0 peak through the M+5 peak, same as the GCMS. The Leucine signal was mostly concentrated in the cotyledon and was very similar in distribution to Glycine. The relative intensities of the isotopes M+2 through M+5 were of similar value. This observation was identical with the GCMS data.

Proline (**Figure 7**) had a very concentrated abundance and was mostly in the hypocotyl and root for the control plants. The isotopically labeled plants had more abundance in the cotyledon, similar to Glutamine. Little to no signal for the M+2 and M+3 isotopes was observed for the 7-day samples. However, the M+4 isotope was observed. In both the 7-day and 14-day labeled samples the M+1 peak had the highest signal. Pyroglutamic Acid (**Figure 7**) was observed mostly in the cotyledon, although some concentrated signal was seen in the hypocotyl and root (e.g. 7-day labeled M+2 isotope). All five isotopes were observed in the labeled plants and had similar distribution to the GCMS data.

Serine (**Figure 8**) was only observed to the M+1 isotope. The M+0 peak is barely seen in both datasets and was especially intense in the 7-day labeled M+1 isotope. Serine was mostly concentrated in the cotyledon with lower signals seen throughout the plant. Threonine (**Figure 8**) was not observed by GCMS, but its enrichment was readily seen by MSI. Threonine was mostly in the cotyledon, but signal was also seen in the hypocotyl and root. The M+1 and M+2 isotopes were of pretty similar abundance in both isotopically labeled samples. Valine (**Figure 8**) was seen as only the M+0 peak due to a background ion covering the isotopes. Signal from Valine was observed throughout the plant, but especially in the cotyledon. The relative signal from the control plants was much greater than that from the labeled plants.

Conclusion

ELDI-MSI was successful in imaging thirteen amino acids and was sensitive enough to detect most of the isotopes observed in the GCMS total metabolite extraction. The MSI data was mostly similar to the GCMS, however one major difference was the isotopic abundance of the M+1 through M+5 peaks were much greater for all amino acids in the isotopically labeled plants in the MSI for the M+0 peak as compared to the GCMS.

This study showed the effectiveness of ELDI-MSI to monitor uptake and localization of amino acid in Arabidopsis plants. This was the first study to use ELDI with a 50 µm lateral resolution. This spot size was needed to successfully analyze Arabidopsis plants, due to their small size (cotyledon are only ~1 mm in diameter). Typical ELDI or

LAESI spatial resolutions of 200+ µm would not be high enough to obtain spatial localization information on these plants. Reported in this study are more amino acids than have been previously reported by similar MSI methods, showing ELDI-MSI as a useful tool for amino acid localization studies.[1,11]

Future work will include increasing the spatial resolution by cutting the spot size in half to 25 µm. This will allow for greater interrogation of the hypocotyl and root since they are much smaller than the cotyledon. Removing background interferences that covered the Valine isotopes is also needed. Increased sensitivity to see additional isotopes by ELDI that are observed in the GCMS will also be explored. This may be accomplished by pneumatically assisted ESI or an environmental chamber around the ELDI-ion source.

Acknowledgements

This research was supported by funds from the U.S. Department of Energy, Office of Biological and Environmental Research through award DESC0014038 to Iowa State University. The ELDI-MSI instrumentation was funded by the Office of Basic Energy Sciences, Separations and Analysis Program, U. S. Department of Energy. Metabolomics analyses were conducted at the Iowa State University's W.M. Keck Metabolomics Research Laboratory.

References

1) Shiea, J., Huang, M., HSu, H., Lee, C., Yuan, C., Beech, I., and Sunner, J., Electrospray-assisted laser desorption/ionization mass spectrometry for direct ambient analysis of solids. Rapid Commun. Mass Spectrom., **2005**, 19: 3701-3704.

2) Huang M.Z., Jhang S.S., Shiea J., Electrospray Laser Desorption Ionization (ELDI) Mass Spectrometry for Molecular Imaging of Small Molecules on Tissues. In: He, L. (eds) Mass Spectrometry Imaging of Small Molecules. Methods in Molecular Biology (Methods and Protocols), **2015**, vol 1203. Humana Press, New York, NY.

3) Huang, M-Z., Cheng, S-C., Jhang, S-S., Chou, C-C., Cheng, C-N., Shiea, J., Popov, I.A., Nikolaev, E.N., Ambient molecular imaging of dry fungus surface by electrospray laser desorption ionization mass spectrometry. International Journal of Mass Spectrometry, **2012**, 325–327: 172-182.

4) Cheng, S-C., Shiea, C., Huang, Y-L., Wang, C-H., Cho, Y-T., and Shiea, J., Laser-based ambient mass spectrometry (Minireview). Anal. Methods, **2017**, 9: 4924-4935.

5) Feenstra, A.D., Dueñas, M.E., & Lee, Y.J., Five micron high resolution MALDI mass spectrometry imaging with simple, interchangeable, multi-resolution optical system. J. Am. Soc. Mass Spectrom., **2017**, 28: 434-442.

6) Lee, Y. J., Perdian, D. C., Song, Z. , Yeung, E. S. and Nikolau, B. J., Use of mass spectrometry for imaging metabolites in plants. The Plant Journal, **2012**, 70: 81-95.

7) Boughton, B.A., Thinagaran, D., Sarabia, D., Bacic, A., Roessner, U., Mass spectrometry imaging for plant biology: a review. Phytochem. Rev., **2015**, 15: 445-488.

8) Stolee, J. A., Shrestha, B., Mengistu, G., and Vertes, A., Observation of Subcellular Metabolite Gradients in Single Cells by Laser Ablation Electrospray Ionization Mass Spectrometry. Angew. Chem. Int. Ed., **2012**, 51: 10386-10389.

9) Shrestha, B., Patt, J.M., and Vertes, A., In Situ Cell-by-Cell Imaging and Analysis of Small Cell Populations by Mass Spectrometry. Analytical Chemistry, **2011**, 83(8): 2947-2955.

10) Bartels, B., & Svatoš, A., Spatially resolved in vivo plant metabolomics by laser ablation-based mass spectrometry imaging (MSI) techniques: LDI-MSI and LAESI. Frontiers in Plant Science, **2015**, 6: 471.

11) Nemes, P., Barton, A. A., and Vertes, A., Three-dimensional imaging of metabolites in tissues under native conditions by laser ablation electrospray ionization mass spectrometry. Anal. Chem., **2009**, 81: 6668–6675.

12) Galayda, K.J., Use of ultraviolet laser ablation electrospray ionization mass spectrometry for plant metabolite imaging. Iowa State University Graduate Theses and Dissertations, **2017**, 15517.

13) Schmidt, M. A., Barbazuk, W. B., Sandford, M., May, G., Song, Z., Zhou, W., … Herman, E. M., Silencing of soybean seed storage proteins results in a rebalanced protein composition preserving seed protein content without major collateral changes in the metabolome and transcriptome. Plant Physiology, 2011, 156(1): 330–45.

14) Young, J. D., Allen, D. K., & Morgan, J. A., Isotopomer Measurement Techniques in Metabolic Flux Analysis II: Mass Spectrometry. In Methods in molecular biology (Clifton, N.J.), 2014, 1083: 85–108.

Table 1. List of Amino acids and each isotope at the detected m/z values by ELDI.

Amino Acid	Adduct	Isotope	m/z	Δppm
Alanine	$[M+H-H_2O]^+$	M	72.0450	1.4
		M+1	73.0454	
		M+2	74.0451	
Arginine	$[M+H]^+$	M	175.1200	2.9
		M+1	176.1186	
		M+2	177.1209	
		M+3	178.1217	
		M+4	179.1196	
		M+5	180.1203	
Aspartate	$[M+K]^+$	M	171.9997	8.8
		M+1	173.0007	
		M+2	174.0027	
GABA	$[M+H-H_2O]^+$	M	86.0610	4.8
		M+1	87.0603	
		M+2	88.0572	
		M+3	89.0579	
		M+4	90.0597	
Glutamate	$[M+H-H_2O]^+$	M	130.0492	9.2
		M+1	131.0470	
		M+2	132.0485	
		M+3	133.0489	
		M+4	134.0531	
		M+5	135.0509	
Glutamine	$[M+H]^+$	M	147.0762	5.2
		M+1	148.0737	
		M+2	149.0768	
		M+3	150.0800	
		M+4	151.0779	
		M+5	152.0809	
Glycine	$[M+Na]^+$	M	98.0210	8.2
		M+1	99.0235	
Leucine	$[M+Na]^+$	M	154.0841	1.9
		M+1	155.0855	
		M+2	156.0876	
		M+3	157.0820	
		M+4	158.0850	
		M+5	159.0886	

Table 1. Continued

Amino Acid	Adduct	Isotope	m/z	Δppm
Proline	$[M+Na]^+$	M	138.0529	1.4
		M+1	139.0529	
		M+2	140.0536	
		M+3	141.0565	
		M+4	142.0550	
Pyroglutamic Acid	$[M+H-H_2O]^+$	M	112.0396	2.3
		M+1	113.0387	
		M+2	114.0428	
		M+3	115.0390	
		M+4	116.0423	
Serine	$[M+H]^+$	M	106.0513	8.3
		M+1	107.0523	
Threonine	$[M+H]^+$	M	120.0664	2.8
		M+1	121.0705	
		M+2	122.0691	
Valine	$[M+H-H_2O]^+$	M	118.0861	6.0

Figures

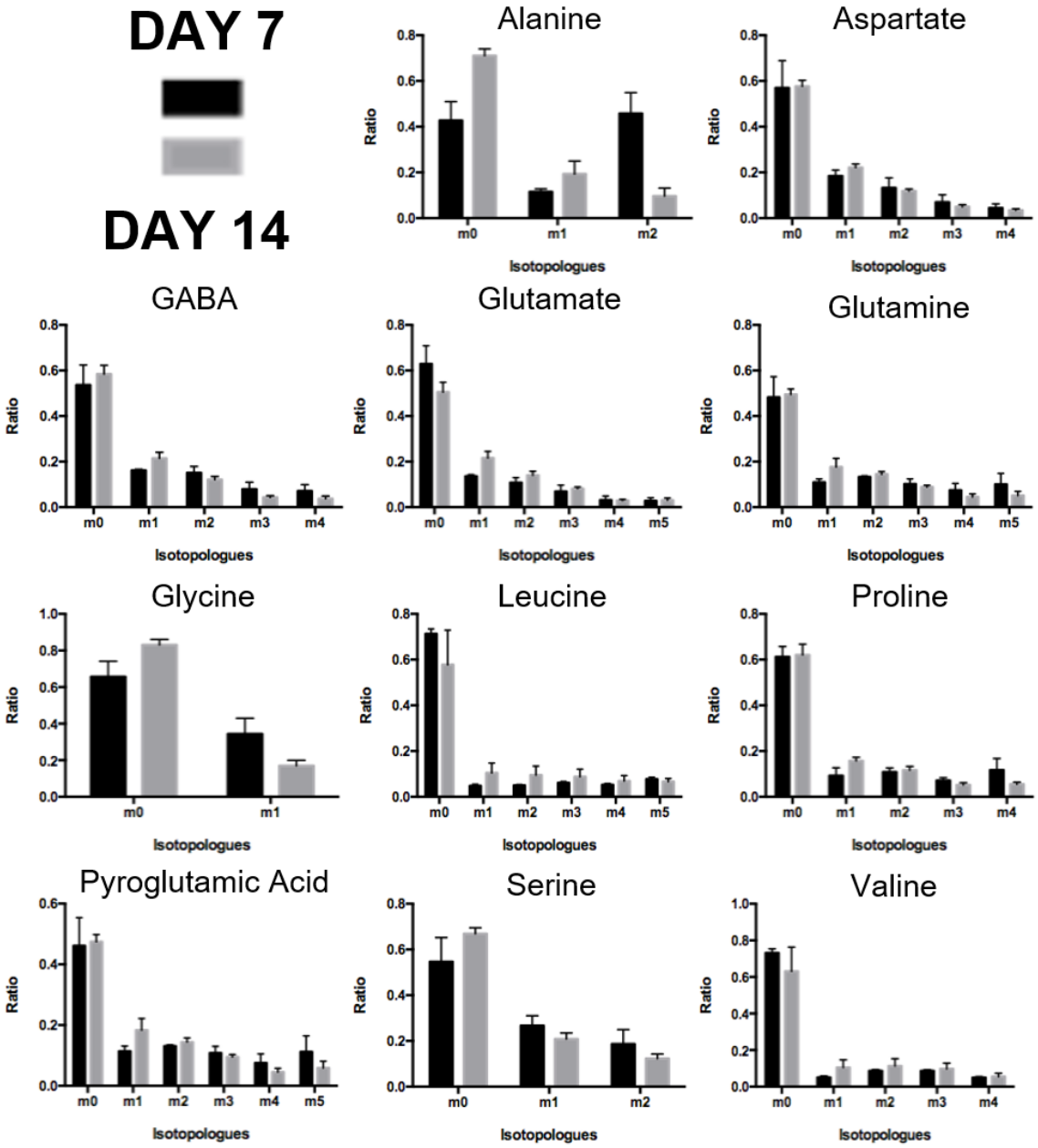

Figure 1. Observed GCMS profiles of 11 amino acids and their isotopic distributions after 7-days (black) or 14-days (gray) of growth in an isotopically labeled glucose solution. M_0 is the molecular ion peak, while M_1 through M_5 refer to the M+1 through M+5 isotopes respectively.

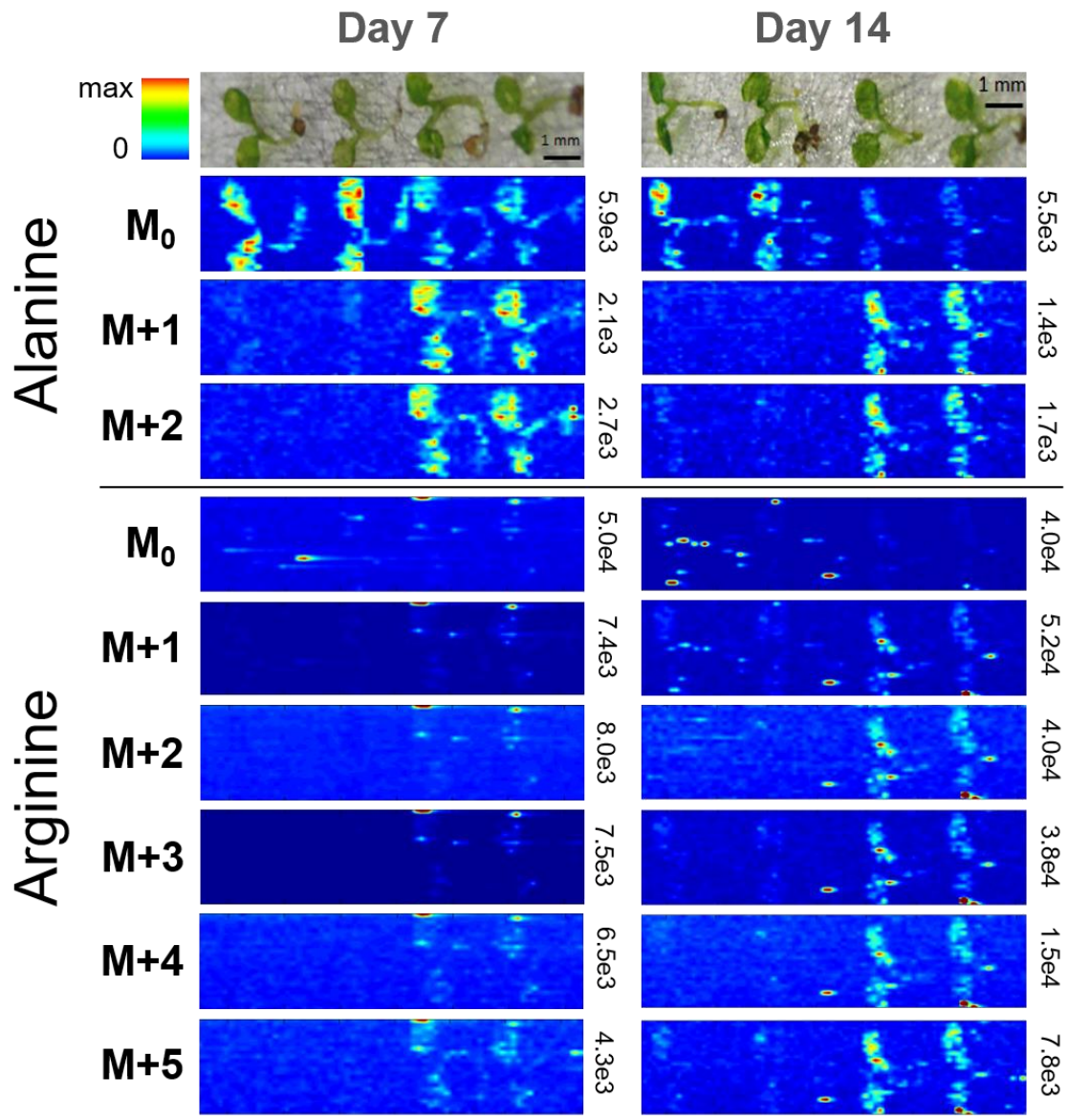

Figure 2. MS-images of alanine and arginine isotopes after 7-days (MS-images on left) and 14-days (MS-images on right). The first two plants in both optical images were grown in a ^{12}C glucose solution as the control. The next two plants in both optical images were grown in a ^{13}C glucose solution, and isotopic enrichment is expected in these plants. The optical images are the same for all MSI figures, and thus the plant positioning is the same. The max signal for each MS-image is located to the right of the image, with the MSI intensity scale bar in the top left of the figure. The scale bar is color coded: red is maximum signal and blue is minimum signal, in this and subsequent figures.

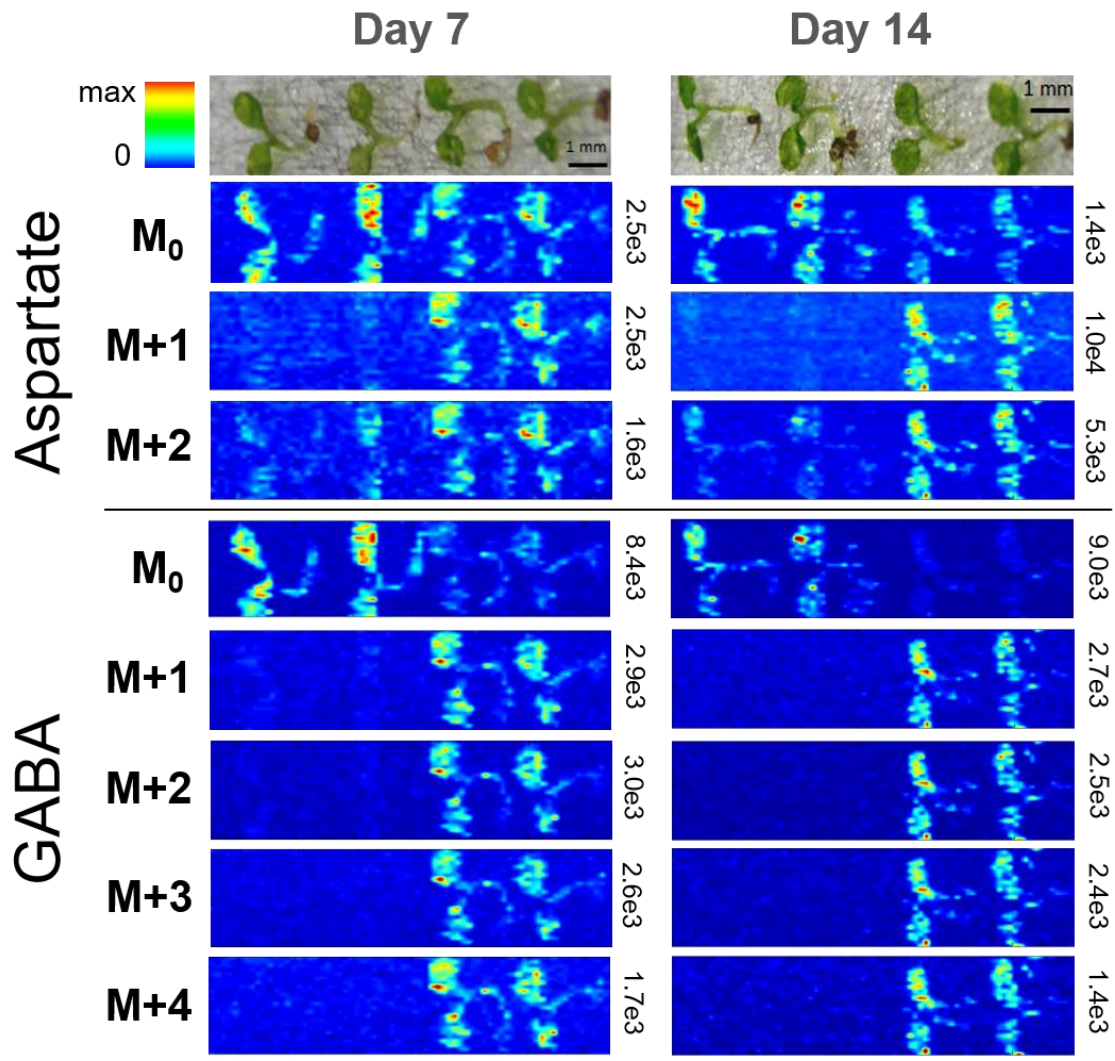

Figure 3. MS-images of aspartate and GABA isotopes after 7-days (MS-images on left) and 14-days (MS-images on right). The max signal for each MS-image is located to the right of the image, with the MSI intensity scale bar in the top left of the figure.

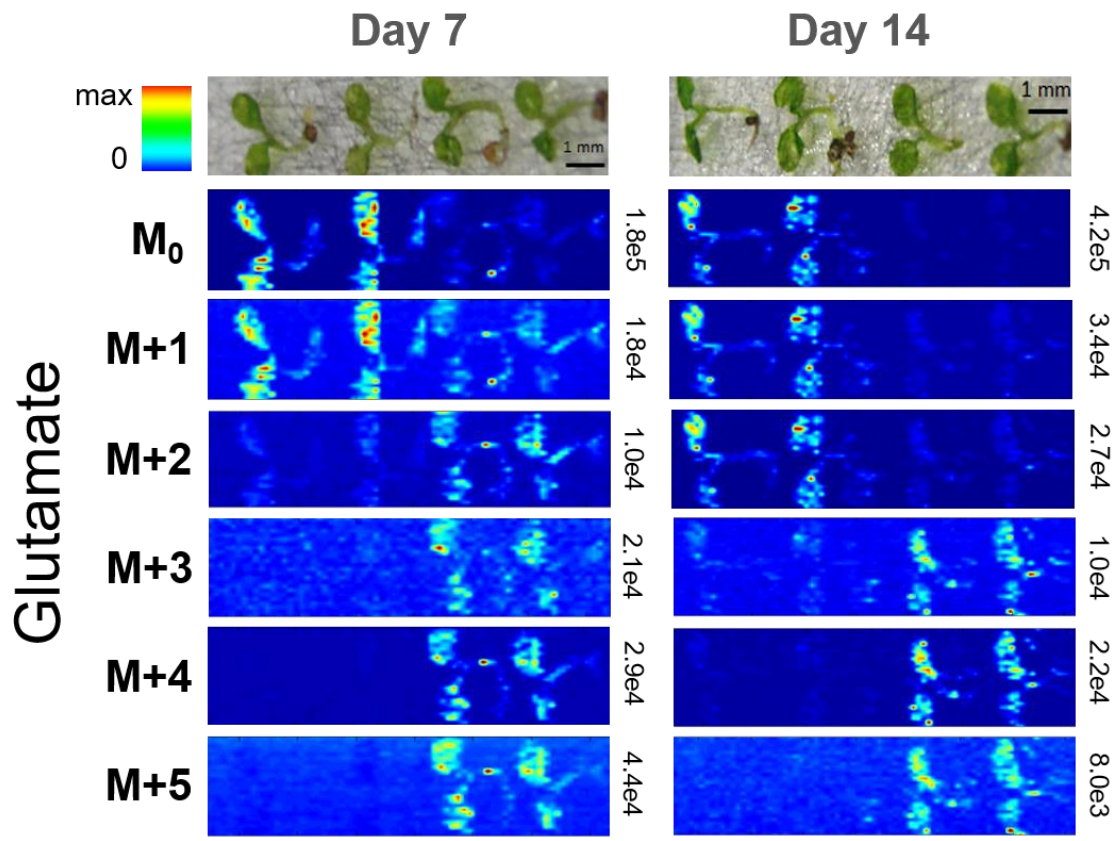

Figure 4. MS-images of glutamate isotopes after 7-days (MS-images on left) and 14-days (MS-images on right). The max signal for each MS-image is located to the right of the image, with the MSI intensity scale bar in the top left of the figure.

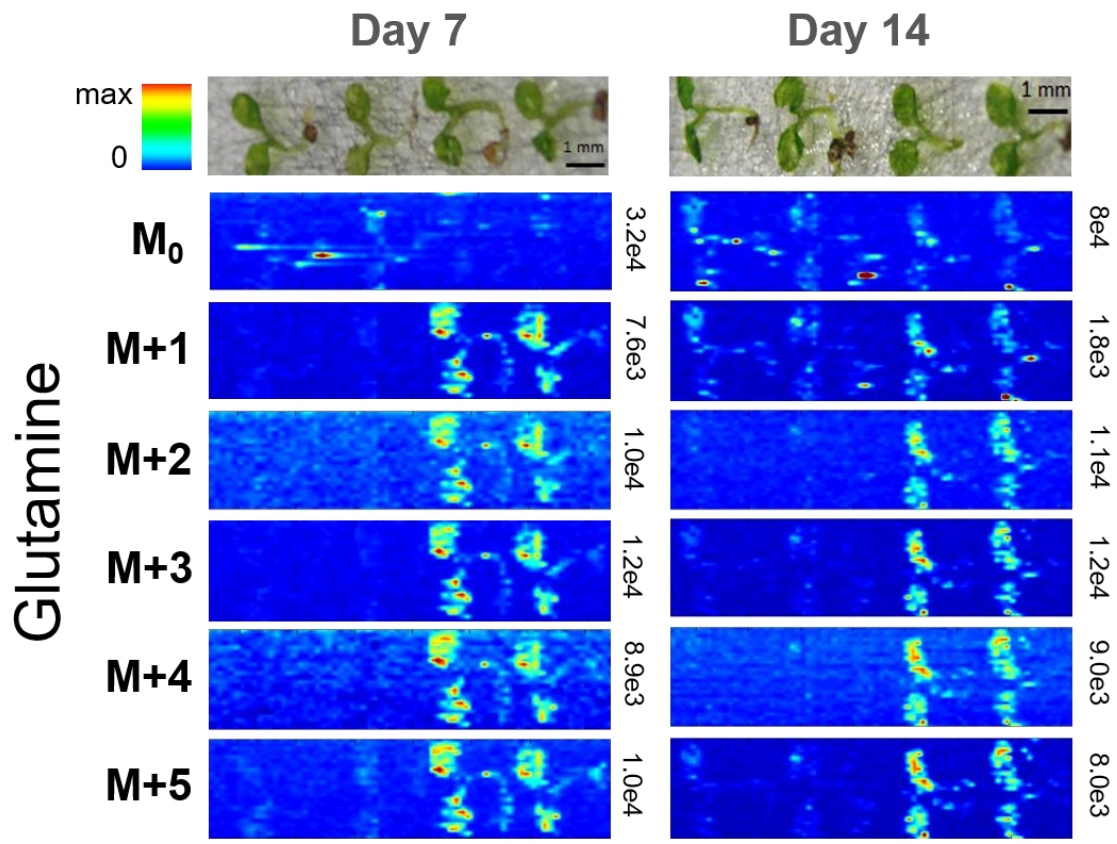

Figure 5. MS-images of glutamine isotopes after 7-days (MS-images on left) and 14-days (MS-images on right). The max signal for each MS-image is located to the right of the image, with the MSI intensity scale bar in the top left of the figure.

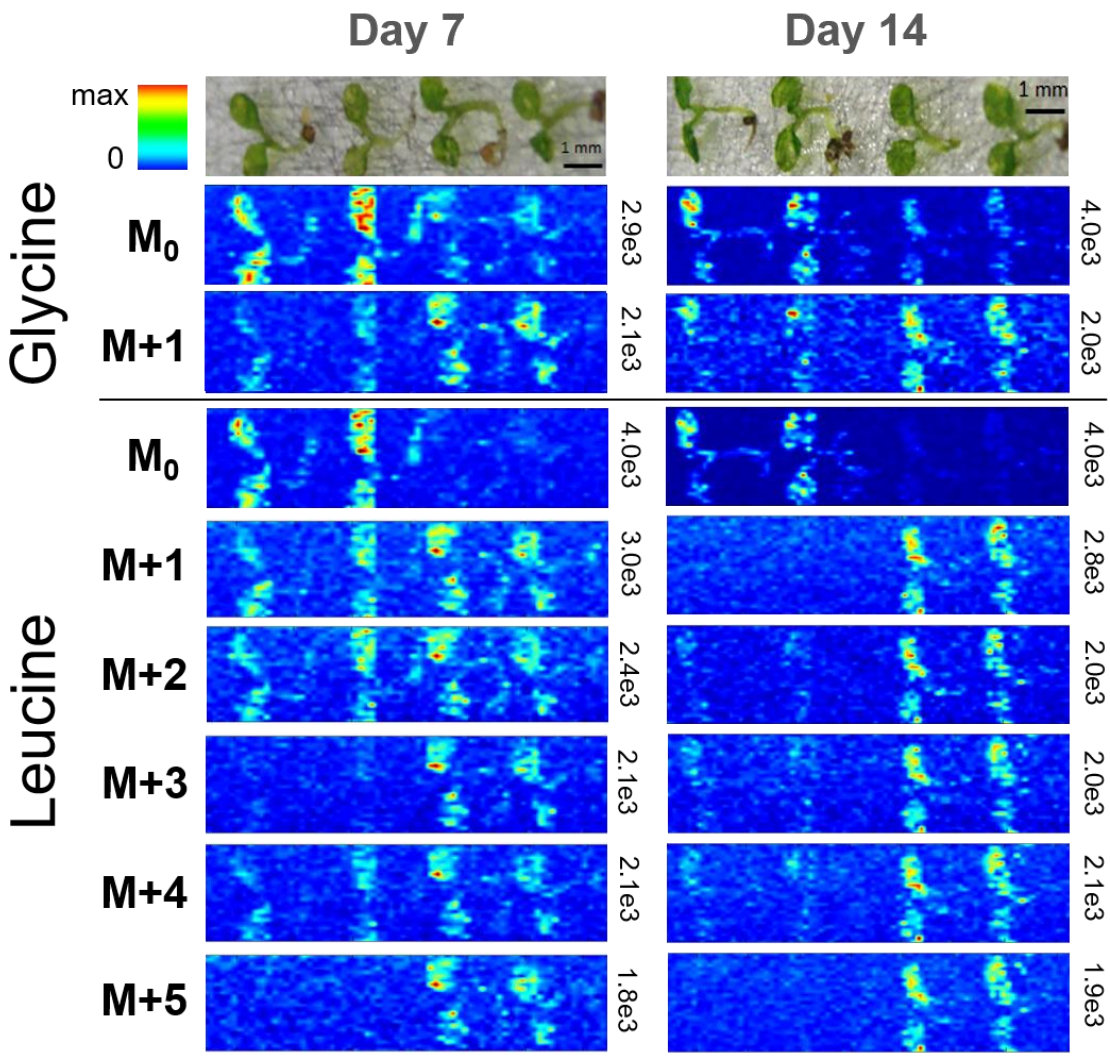

Figure 6. MS-images of glycine and Leucine isotopes after 7-days (MS-images on left) and 14-days (MS-images on right). The max signal for each MS-image is located to the right of the image, with the MSI intensity scale bar in the top left of the figure.

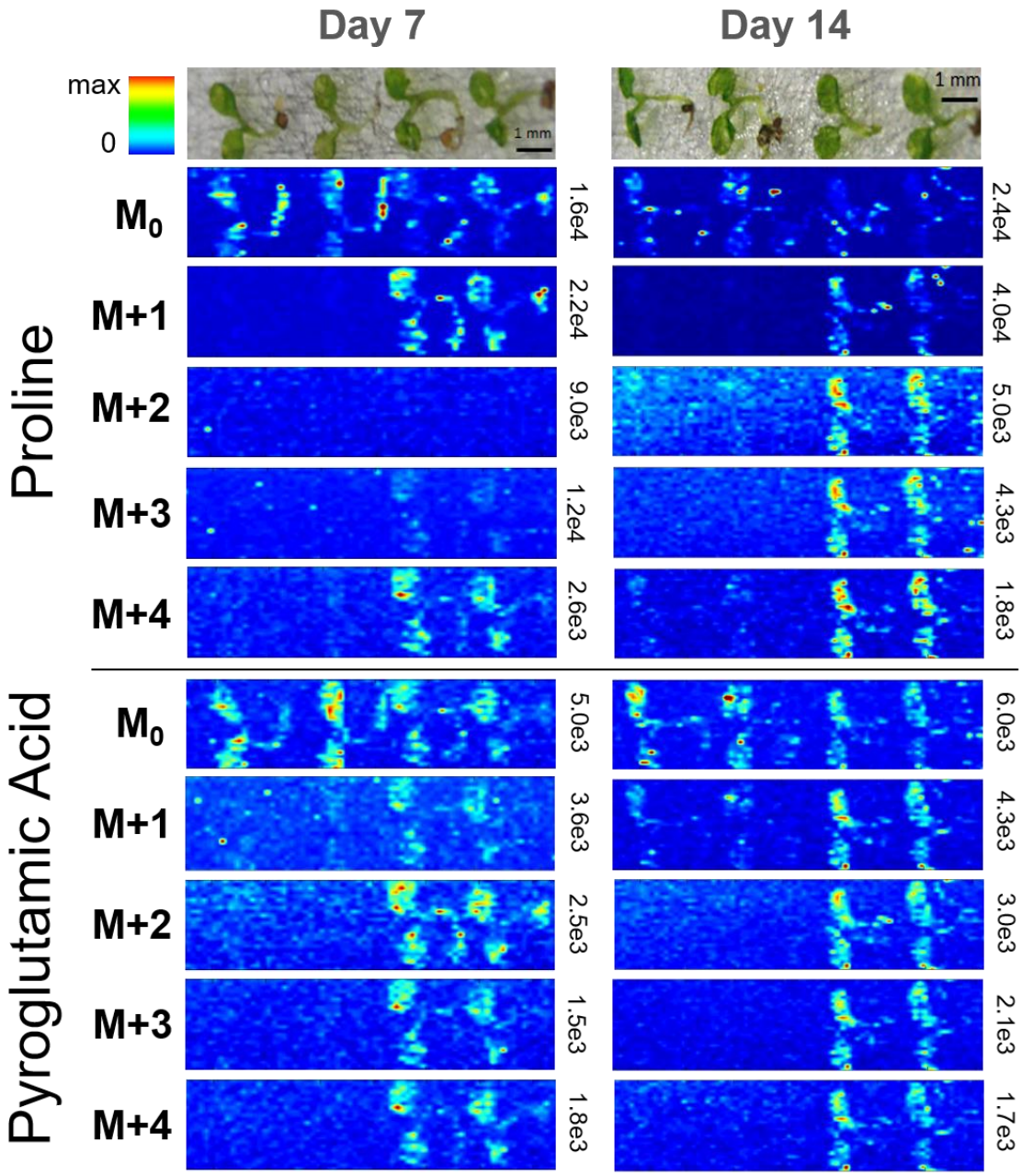

Figure 7. MS-images of glutamate isotopes after 7-days (MS-images on left) and 14-days (MS-images on right). The max signal for each MS-image is located to the right of the image, with the MSI intensity scale bar in the top left of the figure.

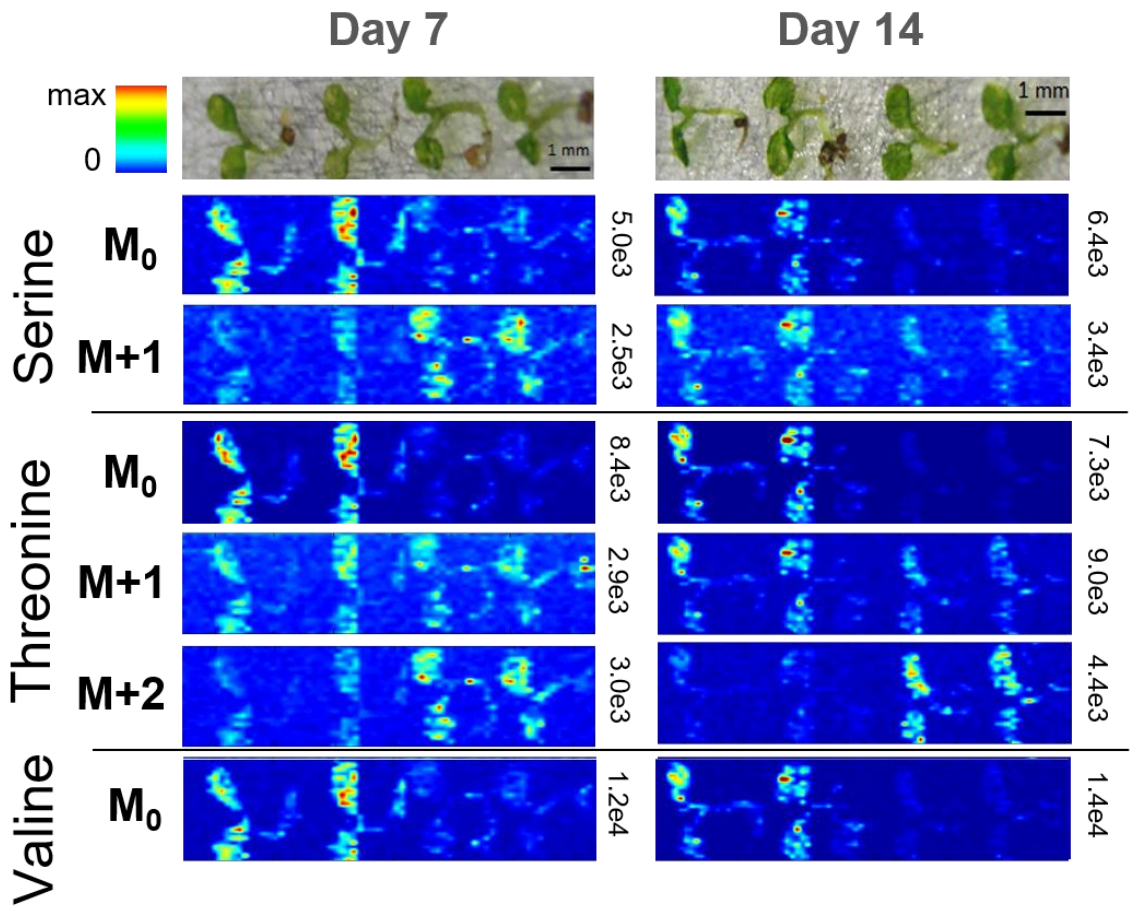

Figure 8. MS-images of serine, threonine, and valine isotopes after 7-days (MS-images on left) and 14-days (MS-images on right). The max signal for each MS-image is located to the right of the image, with the MSI intensity scale bar in the top left of the figure. Note, no isotopes were observed for Valine due to background interferences from electrospray ionization source.

CHAPTER 5.

RAPID DIAGNOSIS OF DRUG AGGLOMERATION AND CRYSTALLINITY IN PHARMACEUTICAL PREPARATIONS BY ELECTROSPRAY LASER DESORPTION IONIZATION MASS SPECTROMETRY IMAGING

A manuscript to be submitted to Analytical Chemistry Letters

Patrick A. McVey[1,2], Gregory K. Webster[3], Katherine-Jo Galayda[1,2,4], R.S. Houk[1,2]

[1] *Department of Chemistry, Iowa State University, Ames, IA, USA*

[2] *Ames Laboratory-US DOE, Ames, IA, USA*

[3] *AbbVie Inc., North Chicago, IL, USA*

[4] *Kemin Industries Inc., Des Moines, IA, USA*

Abstract

In this study we evaluate the applicability of electrospray laser desorption ionization mass spectrometry imaging (ELDI-MSI) to interrogate tablet formulations for the spatial distributions of ingredients. Tablet formulations with varying amounts of crystalline acetaminophen were analyzed to determine if crystallinity could be detected via ELDI-MSI. Tablets with 0%, 2.5%, 5%, 10%, and 20% API crystallinity were successfully imaged. ELDI-MSI concurrently imaged the active pharmaceutical ingredient (API), binders, and surfactants. The spatial distributions of API identified as amorphous were very similar to that of the surfactants. Identified crystalline API was believed to have different spatial locations when compared to the surfactants. The higher the

crystallinity in the tablet formulation, the more agglomeration of the active ingredient was observed by ELDI-MSI. This study shows the capability of ELDI-MSI to diagnose agglomeration and crystallinity content in pharmaceutical preparations with little to no sample preparation. The ability to concurrently image APIs with other components provides valuable information as to their form in the tablet.

Introduction

The bioavailability of the active pharmaceutical ingredient (API) in tablets is critical for the pharmaceutical industry and its consumers. Many drugs are more soluble in the amorphous form compared to their crystalline state, ultimately increasing the bioavailability of the API.[1,2,3] Also, the crystalline form of the API can be unstable.[3,4] Therefore, it is important for the pharmaceutical industry to be able to determine the amount of crystalline API in tablet formulations.[5]

Several analytical techniques are utilized currently for this task. Raman and NIR spectroscopy has been successfully used to monitor crystallization of APIs.[6,7,8] Raman imaging on pharmaceutical tablets can observe crystallinity[9], and other spectroscopic techniques have been extensively used to image tablets.[10] While these have proven effective, spectroscopic methods have level of detection and selectivity drawbacks due to other crystalline species in the drug formulation matrix (e.g. excipients, multiple APIs).

Mass spectrometry imaging (MSI) has been utilized extensively to analyze drug uptake in animal tissues.[11] However, it has not been widely used to study the same APIs

in the initial tablet.[12] Desorption electrospray ionization (DESI) has been used quite a bit for pharmaceuticals[13-18], but little DESI-MSI has been reported. One study used DESI-MSI in tandem with other analytical methods for identification of counterfeit drugs.[19] A study by Cooks' lab showed the applicability of fiducial markers for MSI on tablets.[20] Another method successfully applied for MSI on tablets was infrared laser ablation metastable-induced chemical ionization (IR-LAMICI), which was also used for counterfeit pill identification.[21]

MSI could be advantageous compared to other chemical imaging techniques due to its potential to image multiple APIs in the same formulation, as well as other chemical components (e.g. surfactants, binders, etc.) with the inherent sensitivity and selectivity advantages of mass spectrometry. The spatial information provided by MSI could be useful to diagnose agglomeration due to crystalline API in an amorphous formulation. High mass resolution data would also mean little overlap in multiple API signals, a significant issue with Raman and IR spectroscopy methods.

Electrospray Laser Desorption Ionization (ELDI) has been shown to effectively analyze drug tablets with different active ingredients.[22] However, ELDI-MSI has not been explored with pharmaceutical tablets. Matrix-assisted laser desorption ionization (MALDI) has been used to image tablets[23,24] but not extensively. ELDI differs from MALDI in that it is a matrix-free method that requires no sample preparation.[25] ELDI also operates at atmospheric pressure, while MALDI is typically done under vacuum. The fact that ELDI requires no sample preparation and operates at ambient pressure makes it an advantageous MSI method for analysis of pharmaceutical tablets.

In the present study, ELDI-MSI was used to determine differences in API spatial distributions between formulations of differing amorphous-to-crystalline API ratios. Agglomeration of the active ingredient, acetaminophen, was diagnosed as crystalline API content increased. Crystalline API locations were determined by overlaying of API and surfactant MS-images.

Experimental

ELDI-MS

A Waters Synapt G2-S quadrupole time-of-flight mass spectrometer was used for data collection. The Waters (ESI) source was removed and a homemade open-air ESI source <KJ Thesis REF> was used with samples at ambient pressure. Data were acquired in the mass range from m/z 50 to 1200. The time-of-flight reflectron operated in single-pass mode with a mass spectral resolution of ~10,000 FWHM for MS images. Tandem MS quadrupole resolution was set at Δm=5. The collision energy was 20 eV nominally for the API. The Synapt was operated using Waters MassLynx V4.1 (SCN851) software.

ELDI Source

Samples were ablated with a Nd:YAG laser (ULTRA, Big Sky Laser Tech, Inc., Bozeman, MT). The third harmonic was used at 355 nm. The laser was operated at a pulse repetition rate of 10 Hz, with a 5 ns pulse width, and an energy of ~250 μJ/pulse (before focusing). This pulse energy was just above the ablation threshold for these samples. The beam was focused onto the sample by a beam expander followed by a

single plano-convex focusing lens (fused-silica focal length 75 mm), with a nominal spot size of ~50 µm.

Flat pill samples were mounted on a glass slide using double sided tape. No matrix was applied. Samples were then placed 8 mm below the ESI-sample inlet axis on a computer-controlled translation stage (Z825B, Thorlabs, Inc. Newton, NJ). Samples were translated at 0.4 mm/sec beneath the 10 Hz laser beam down the surface of the tablet. The middle 7.5 mm of a 10 mm wide pill was imaged. The distance between the centers of adjacent ablation tracks was 100 µm, providing a lateral resolution of 100 µm. The ablation trench was ~30 µm deep, much less than the pill thickness. Mass spectra were averaged over 0.25 second intervals. Thus, the ablated volume was 50 µm by 100 µm by 30 µm deep per pixel. The tablets were irradiated normal to the sample surface with the laser beam axis ~2 mm downstream from the ESI capillary. The ESI tip was ~10 mm from the sample inlet.

A solution of 50% methanol with 0.1% formic acid (99.5% purity, Fisher Scientific) was pumped through a 53 µm ID polyimide coated capillary as the ESI solution (pump: model Z2, Harvard Apparatus, South Natick, MA). Leucine enkephalin was added at 0.1 ppm to the ESI solution for use as a mass calibrant. All data were acquired in positive ESI mode. The ESI voltage was +2.5 kV applied to a stainless steel union in the liquid flow line, with the sample cone completing the ESI circuit. The sample inlet was kept at 100^{o}C with a N_2 curtain gas flow of 1 L/hr.

Data Handling

Spectra were generated from total ion chromatograms (TIC) combined by the MassLynx software. The ".raw" Waters data files were converted to mzML files by Proteowizard Mass Converter Tool. The MzML files were then combined into an imzML file using imzMLconverter. This combined image file was then viewed and images were generated from MSiReader V1.00 via the W.M. Keck FTMS Laboratory. All images made within MSiReader had Linear^2 interpolation for image clarity, and used the "Jet" colormap/false color appearance. Co-localization and 3D images were created with MSiReader V1.00.

LCMS Surfactant Identification

LCMS spectra were taken of surfactant standards for identity confirmation in the ELDI spectrum. LCMS work was done on an Agilent QTOF 6540 high resolution quadrupole time-of-flight mass spectrometer operated using electrospray ionization. The Agilent MassHunter software was used for data collection and processing. The surfactant standards were lauroglycol (L90) (Sigma) and tween-80 (T80) (Sigma).

Tablet Formulation

Acetaminophen tablets (100 mg API) were created by AbbVie at 0, 2.5, 5, 10, and 20% crystallinity. The acetaminophen (Sigma, USP grade) was initially crystalline. The hot melt extrusion (HME) process dissolved the drug into the tablet filler copovidone (Plasdone S-630 polymer, Ashland, Columbus, OH) to become an amorphous solid

dispersion (ASD). Lauroglycol (7%) and tween-80 (3%) surfactants were used to bind the amorphous acetaminophen into tablet form. The ASD amorphous acetaminophen was then blended with the crystalline acetaminophen to get the various crystalline spiked percentages, with additional copovidone added to act as filler. The pills were then doped with titanium dioxide (Sigma, exp 21 Dec 2018) to enhance laser absorption for ablation. All blends were extruded on a Thermo Process 11 Hygienic TSE using a gravimetric twin screw feeder. The extrusion process was kept the same for all blends.

Safety Considerations

Appropriate laser safety goggles were worn during ELDI experiments. Breathing masks were worn when ablating pills to avoid inhalation of ablated particles.

Results and Discussion

ELDI of Acetaminophen Tablets

Sample pills prepped at 0, 2.5, 5, 10, and 20% crystallinity were imaged using ELDI-MSI. Acetaminophen was concurrently observed as $[M+H]^+$ at m/z 152.0717 (Δm = 3.6 ppm), $[M+Na]^+$ at m/z 174.0540 (Δm = 5.2 ppm), and $[M+K]^+$ at m/z 190.0271 (Δm = 0.33 ppm) (**Figure 1**). The spatial distributions for each adduct were identical in all pills. The surfactant L90 was observed at m/z 241.2178, 458.4211 and 903.7629. The surfactant T80 was observed as a series of peaks approximately 44 m/z apart and ranging from m/z 657.4307 to 965.6449 (**Figure 1 inset**). The three L90 peaks and the

distribution from T80 were identified as L90 and T80 by standard samples run via LCMS to confirm their identity in the ELDI spectrum.

Filler compounds were observed throughout each pill (**Figure 2A**). These compounds are expected as they make up the bulk of the formulation. A relatively low signal intensity from acetaminophen was observed throughout the surface of every pill and at each crystallinity composition. Pills consisting of 0% crystalline acetaminophen had a consistent spatial distribution for the API (**Figure 2B**). Signals from acetaminophen were observed throughout the pill surface in nearly equal abundance. Pills consisting of 2.5% crystalline acetaminophen had a fairly consistent spatial distribution for the API, but some agglomeration was observed (**Figure 2C**). Pills consisting of 5% crystalline acetaminophen had much more intense agglomeration (**Figure 2D**). Several intense API spots were observed. Pills with 10% (**Figure 2E**) or 20% (data not shown) crystalline acetaminophen had fewer agglomerates, but more at a higher intensity as compared to the 5% crystalline pills.

Surfactants (L90 and T80) used to "gel" the amorphous form of acetaminophen had very similar spatial distributions to the acetaminophen MSI (e.g. **Figure 3**). It is expected that wherever a high surfactant signal is observed in the MSI, a corresponding signal will be observed for amorphous acetaminophen. Acetaminophen signal observed without any surfactant signal is expected to be from crystalline acetaminophen. This is due to the surfactant binding only amorphous acetaminophen into the tablet during the hot melt extrusion process.

The 0% crystalline acetaminophen tablets had similar spatial distributions between the API and the L90 surfactant. This can be seen in **Figure 3**, the co-localization MS image of a 100% amorphous acetaminophen tablet comparing the API and L90 spatial distributions. However, when comparing the 5% crystalline acetaminophen tablet's API and L90 surfactant signals the spatial distributions do not match perfectly, as seen in **Figure 4**. Any signal from acetaminophen that does not have a corresponding spatial match with the L90 surfactant is expected to be crystalline acetaminophen. The same result is shown for the 20% crystalline acetaminophen tablet in **Figure 5**. In this case, a large acetaminophen crystal is observed in the upper right corner of the MS image, where no corresponding surfactant signal is observed. Other smaller crystalline acetaminophen agglomerations are visible throughout the co-localization image.

Since the majority of the API is amorphous in these formulations most of the API signal has an overlapping surfactant signal. There is a relatively low (~2e4) API signal observed throughout the tablet in all formulations. Under the intensity scale used in Figures 2-5, only the large agglomerates are observed. Therefore, acetaminophen is still spread throughout the tablet; however its bioavailability would likely be lowered due to this agglomeration and crystalline content.

Conclusion

This study was the first application of ELDI-MSI applied to a tablet. This was also the first study to use MSI to detect crystallinity in a pharmaceutical preparation. Agglomeration of the API was shown to occur in samples with higher crystalline content.

Matching the spatial distribution from the acetaminophen signal with that from the surfactants helps distinguish amorphous API from crystalline API. This is an effective marker for crystalline identification as the acetaminophen and surfactant signal almost perfectly overlap in the 100% amorphous sample. However, this is not the case at formulations with crystalline API introduced. Agglomeration of acetaminophen in high intensity spots occurs more extensively in highly crystalline tablet formulations. This agglomeration occurs for both crystalline and amorphous API, as seen in the co-localization images.

One desirable feature of ELDI-MSI on tablets is its ability to concurrently image many ingredients. This can be done with little or no sample preparation, without an applied matrix and at ambient pressure. Without the need for sample preparation, ELDI-MSI analysis could be performed in-line at the point of manufacturing. Since sample preparation can potentially change the crystal structure of the API, this is an important factor.[7]

Due to the laser wavelength available (355 nm) TiO_2 dopant was needed for laser ablation to occur. At a more universal wavelength, such as 214 nm, this doping mechanism should no longer be needed. Laser ablation at 214 or 266 nm should allow for ELDI-MSI to analyze any commercial formulation. Images with small spot size and higher spatial resolution would allow for interrogation of individual API crystals, and will be explored in future experiments. Additional tablet formulations of multiple APIs will also be explored.

Acknowledgements

The authors would like to thank AbbVie for the financial support to do this project.

Instrument was provided by the Ames Lab DOE. The LCMS was done by Dr. Kamel Harrata of Instrument Services at ISU.

References

1) Yu, L., Amorphous pharmaceutical solids: preparation, characterization and stabilization. Adv. Drug Deliv., **2001**, Rev., 48: 27-42.

2) Craig, D.Q.M., Royall, P.G., Kett, V.L., Hopton, M.L., The relevance of the amorphous state to pharmaceutical dosage forms: glassy drugs and freeze dried systems. Int. J. Pharm., **1999**, 179: 179-207.

3) Bernstein, J., Polymorphism in Molecular Crystals; **2002**, Clarendon Press: Oxford.

4) Willart, J.F., and Descamps, M., Solid state amorphization of pharmaceuticals. Mol. Pharm., **2008**, 5: 905-920.

5) Jacob, S., Nair, A.B., Patil, P. N., and Panda, B. P., Solid state crystallinity, amorphous state, and its implications in the pharmaceutical process. Int. Journal of Pharmaceutical Sciences, **2011**, 2(3): 472-482.

6) Widjaja, E., Kanaujia, P., Lau, G., Ng, W.K., Garland, M., Saal, C., Hanefeld, A., Fischbach, M., Maio, M., Tan, R.B.H., Detection of trace crystallinity in an amorphous system using Raman microscopy and chemometric analysis. European J. Pharmaceutical Sciences, **2011**, 42(1-2): 45-54.

7) Pataki, H., Markovits, I., Vajna, B., Nagy, Z.K., Marosi, G., In-Line Monitoring of Carvedilol Crystallization Using Raman Spectroscopy. Crystal Growth & Design, **2012**, 12(11): 5621-5628.

8) Sakamoto, T., Nakayama, K., Fujimaki, Y., Sasakura, D., Kawanishi, T., Hiyama, Y., Application of NIR spectroscopy/macroscopic mapping as a quality evaluation tool of crystal reservoir-type TDDS tapes, and an approach to high-precision qualitative prediction of API by NIR spectroscopy. Iyakuhin Iryo Kiki Regyuratori Saiensu, **2010**, 41(12): 971-982.

9) Shinzawa, H., Awa, K., Okumura, T., Morita, S-I., Otsuka, M., Ozaki, Y., Sato, H., Raman imaging analysis of pharmaceutical tablets by two-dimensional (2D) correlation spectroscopy, Vibrational Spectroscopy, **2009**, 51(1): 125-131.

10) Fraser-Miller, S.J., Saarinen, J., Strachan, C.J., Vibrational Spectroscopic Imaging. In: Müllertz A., Perrie Y., Rades T. (eds) Analytical Techniques in the Pharmaceutical Sciences. Advances in Delivery Science and Technology, **2016**, Springer, New York, NY.

11) Swales, J. G., Hamm, G., Clench, M. R., Goodwin, R. J. A., Mass spectrometry imaging and its application in pharmaceutical research and development: A concise review. International Journal of Mass Spectrometry, **2018**, In Press.

12) Kempson, I.M., Prestidge, C.A., Mass Spectrometry Imaging of Pharmaceuticals: From Tablets to Tissues. In: Müllertz A., Perrie Y., Rades T. (eds) Analytical Techniques in the Pharmaceutical Sciences. Advances in Delivery Science and Technology, **2016**, Springer, New York, NY.

13) Chen, H., Talaty, N.N., Takáts, Z., and Cooks, R. G., Desorption Electrospray Ionization Mass Spectrometry for High-Throughput Analysis of Pharmaceutical Samples in the Ambient Environment. Anal. Chem., **2005**, 77(21): 6915-6927.

14) Weston, D.J., Bateman, R., Wilson, I.D., Wood, T.R., Creaser, C.S., Direct Analysis of Pharmaceutical Drug Formulations Using Ion Mobility Spectrometry/Quadrupole-Time-of-Flight Mass Spectrometry Combined with Desorption Electrospray Ionization. Anal. Chem., **2005**, 77(23): 7572–7580.

15) Williams, J. P. and Scrivens, J. H., Rapid accurate mass desorption electrospray ionisation tandem mass spectrometry of pharmaceutical samples. Rapid Commun. Mass Spectrom., **2005**, 19: 3643-3650.

16) Leuthold, L. A., Mandscheff, J. , Fathi, M. , Giroud, C. , Augsburger, M. , Varesio, E. and Hopfgartner, G., Desorption electrospray ionization mass spectrometry: direct toxicological screening and analysis of illicit Ecstasy tablets. Rapid Commun. Mass Spectrom., **2006**, 20: 103-110.

17) Roscioli, K.M., Tufariello, J.A., Zhang, X., Li, S.X., Goetz, G.H., Cheng, G., Siems, W.F., Hill, H.H. Jr., Desorption electrospray ionization (DESI) with atmospheric pressure ion mobility spectrometry for drug detection. Analyst, **2014**, 139(7): 1740-50.

18) Nyadong, L., Green, M.D., De Jesus, V.R., Newton, P.N., and Fernández, F.M., Reactive Desorption Electrospray Ionization Linear Ion Trap Mass Spectrometry of Latest-Generation Counterfeit Antimalarials via Noncovalent Complex Formation. Anal. Chem., **2007**, 79(5): 2150–2157.

19) Nyadong, L., Harris, G.A., Balayssac, S., Galhena, A.S., Malet-Martino, M., Martino, R., Parry, R.M., Wang, M.D., Fernández, F.M., and Gilard, V., Combining Two-Dimensional Diffusion-Ordered Nuclear Magnetic Resonance Spectroscopy, Imaging Desorption Electrospray Ionization Mass Spectrometry, and Direct Analysis in Real-Time Mass Spectrometry for the Integral Investigation of Counterfeit Pharmaceuticals. Analytical Chemistry, **2009**, 81: 4803-4812.

20) Ferreira, C.R., Wu, L., Vogt, F.G., Bornancini, E.R., & Cooks, R.G., Fiducial Markers for Distribution of Drug and Excipient on Tablet Surfaces by Multimodal Desorption Electrospray Ionization–Mass Spectrometry (DESI–MS) Imaging. Analytical Letters, **2013**, 47(1): 91-101.

21) Galhena, A.S., Harris, G.A., Nyadong, L., Murray, K.K., and Fernandez, F.M., Small Molecule Ambient Mass Spectrometry Imaging by Infrared Laser Ablation Metastable-Induced Chemical Ionization. Anal. Chem., **2010**, 82: 2178–2181.

22) Huang, M., Hsu, H., Wu, C., Lin, S., Ma, Y., Cheng, T. and Shiea, J., Characterization of the chemical components on the surface of different solids with electrospray-assisted laser desorption ionization mass spectrometry. Rapid Commun. Mass Spectrom., **2007**, 21: 1767-1775.

23) Earnshaw, C. J., Carolan, V. A., Richards, D. S. and Clench, M. R., Direct analysis of pharmaceutical tablet formulations using matrix-assisted laser desorption/ionisation mass spectrometry imaging. Rapid Commun. Mass Spectrom., **2010**, 24: 1665-1672.

24) Gut, Y., Boiret, M., Bultel, L., Renaud, T., Chetouani, A., Hafiane, A., Ginot, Y-M., Jennane, R., Application of chemometric algorithms to MALDI mass spectrometry imaging of pharmaceutical tablets. Journal of Pharmaceutical and Biomedical Analysis, **2015**, 105: 91-100.

25) Cheng, S-C., Shiea, C., Huang, Y-L., Wang, C-H., Cho, Y-T., and Shiea, J., Laser-based ambient mass spectrometry (Minireview). Anal. Methods, **2017**, 9: 4924-4935.

Figures

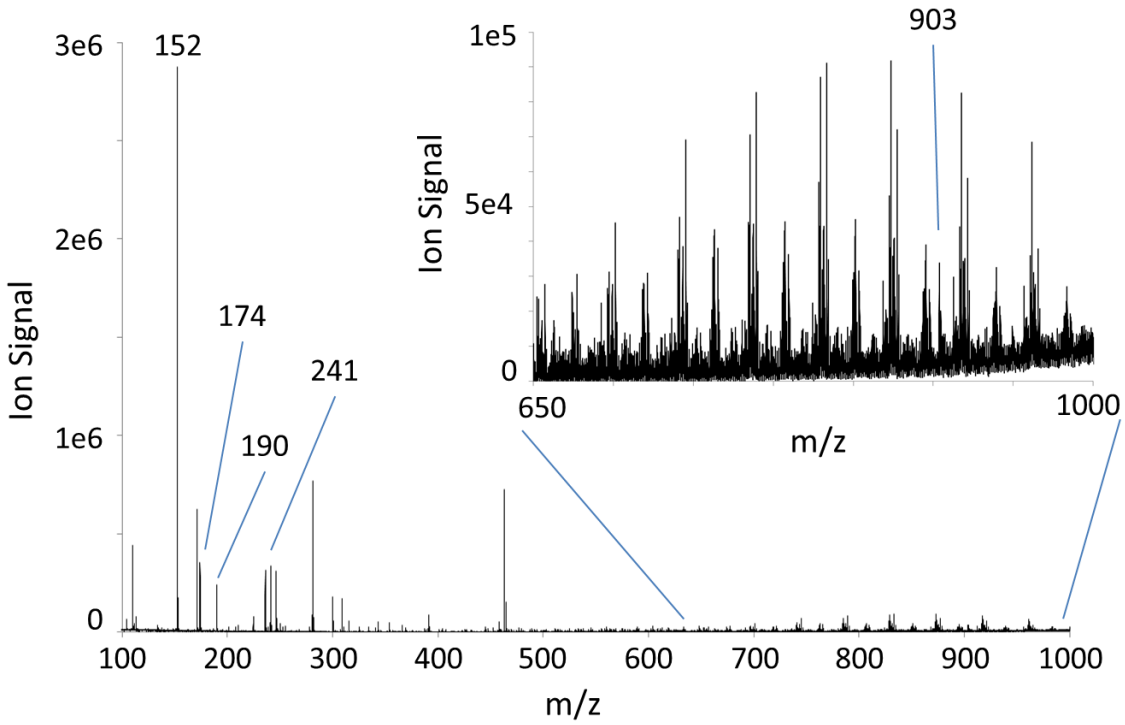

Figure 1. Overall background subtracted ELDI mass spectrum of an ablation track in the 100% amorphous acetaminophen tablet. The labeled peaks at m/z 152, 174, and 190 are from acetaminophen $[M+H]^+$, $[M+Na]^+$, and $[M+K]^+$, respectively. The labeled peaks at m/z 241 and 903 are from the L90 surfactant. The series of peaks shown in the inset mass spectrum are from the T80 surfactant (with the exception of m/z 903).

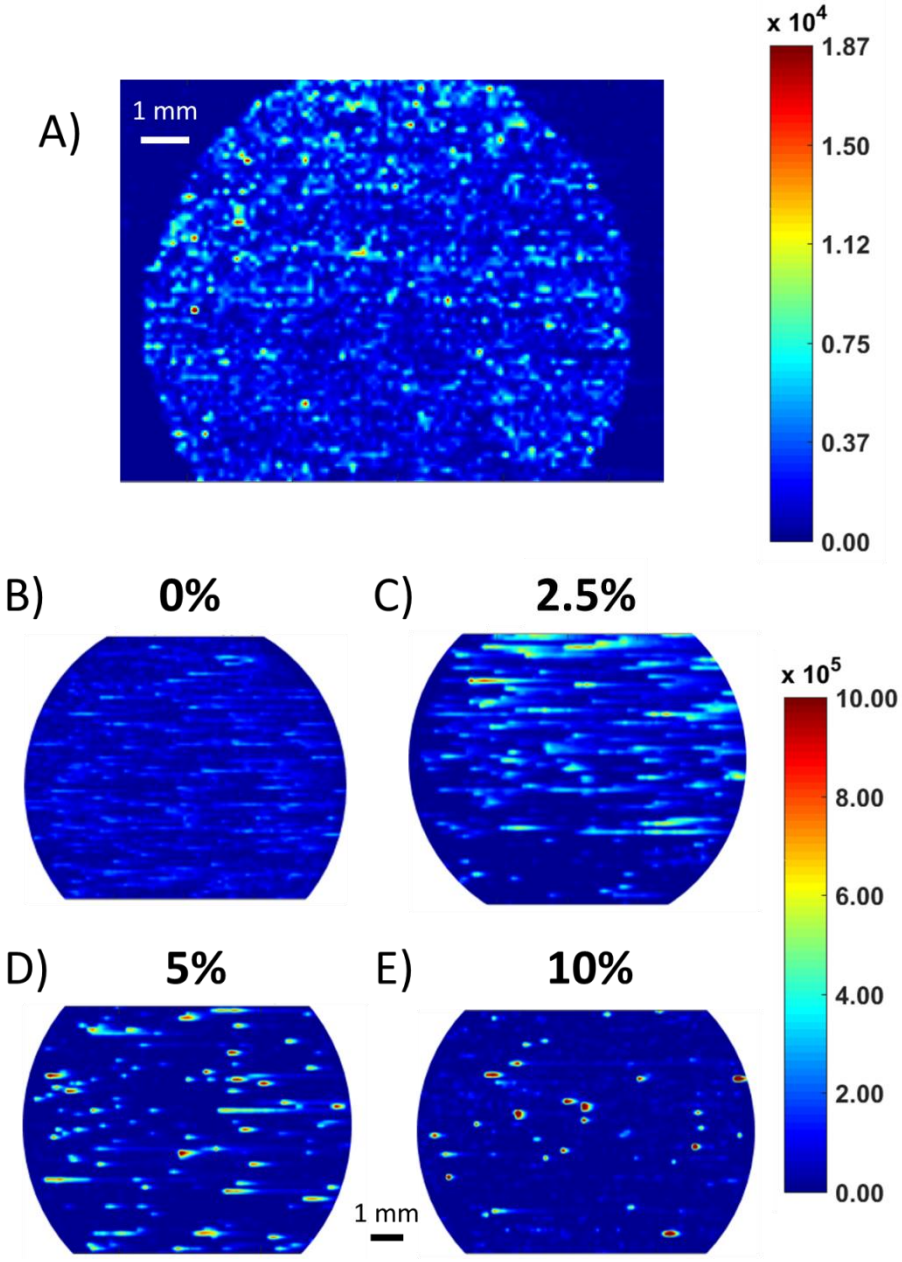

Figure 2. ELDI-MSI of acetaminophen tablets. A) "Filler" compound at m/z 112.0844. A steady signal across the entire tablet surface was observed for multiple of these filler compounds. The MS-images in B, C, D, and E show the spatial distributions of acetaminophen $[M+H]^+$ at different crystallinity percentages, and are set to the same normalized heat map intensity scale.

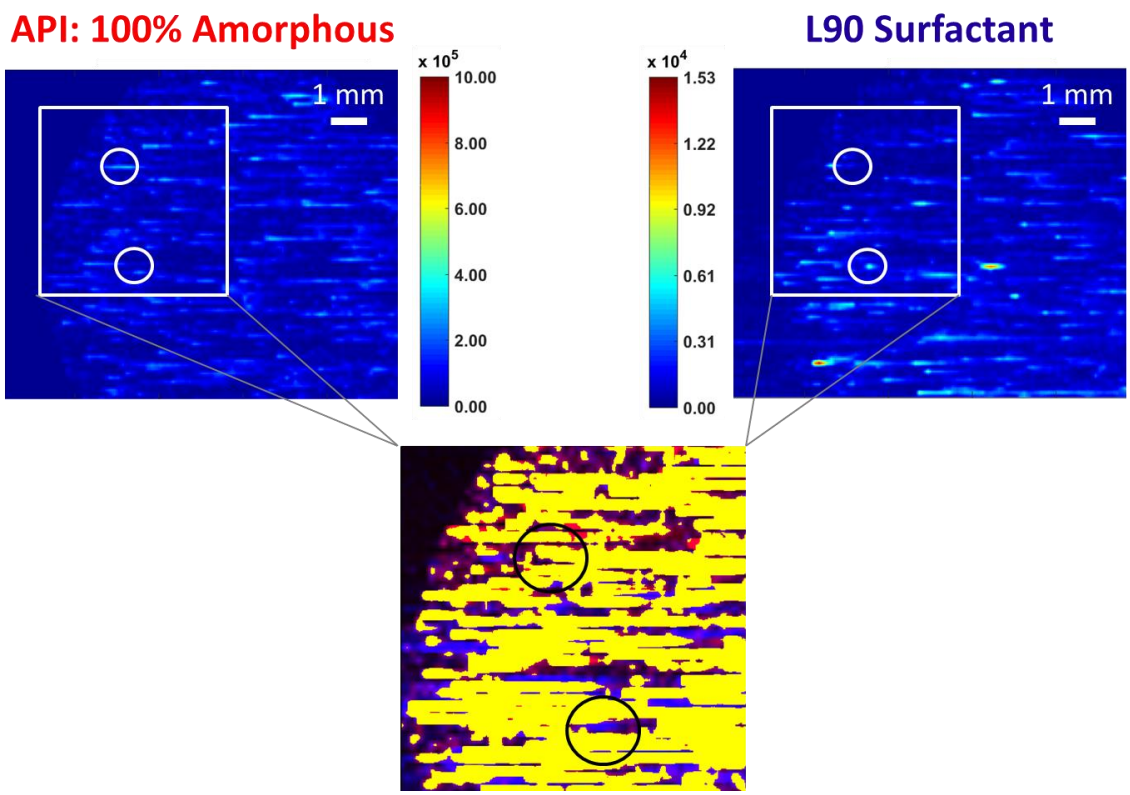

Figure 3. Co-localization MSI (bottom image) of 100% amorphous acetaminophen (APAP, top-left) and the L90 surfactant (top-right). The red represents signal from acetaminophen only, while the blue represents signal from L90 only. The yellow shows where the acetaminophen and L90 signals overlap in the two MS-images.

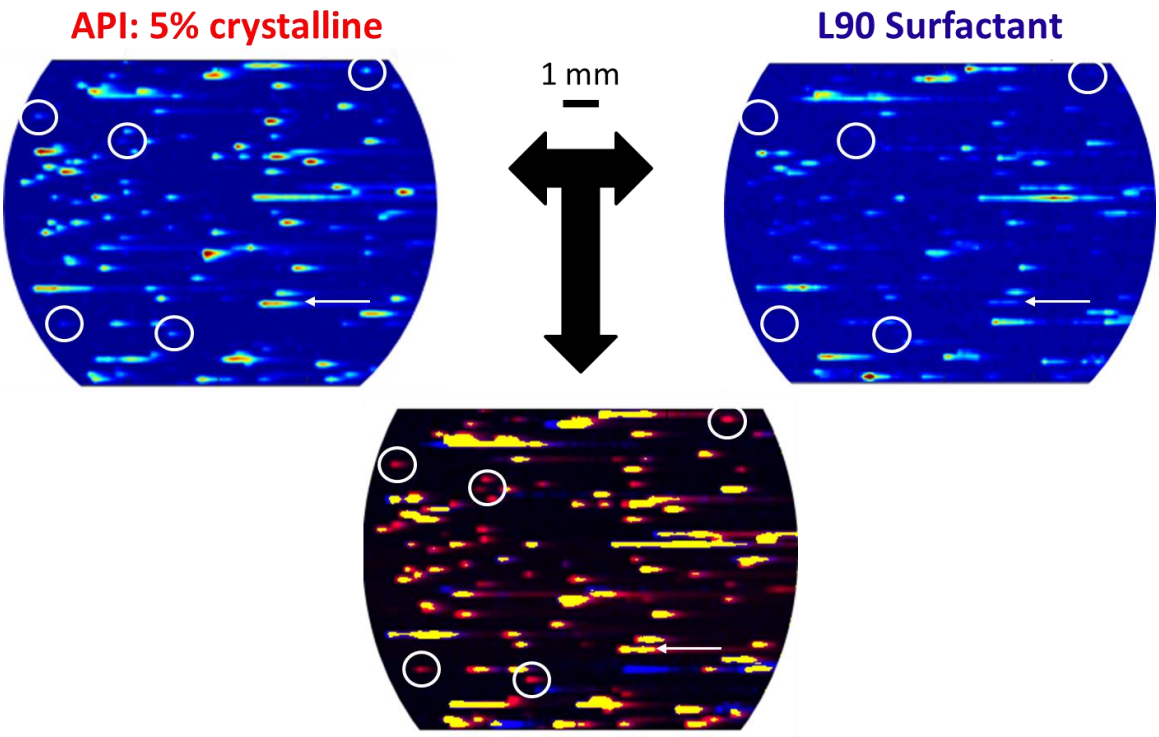

Figure 4. Co-localization MSI (bottom image) of 5% crystalline acetaminophen (APAP, top-left) and the L90 surfactant (top-right). The red represents signal from acetaminophen only, while the blue represents signal from only L90. The yellow shows where the acetaminophen and L90 signals overlap in the two MS-images. Areas circled show examples of identified crystalline acetaminophen.

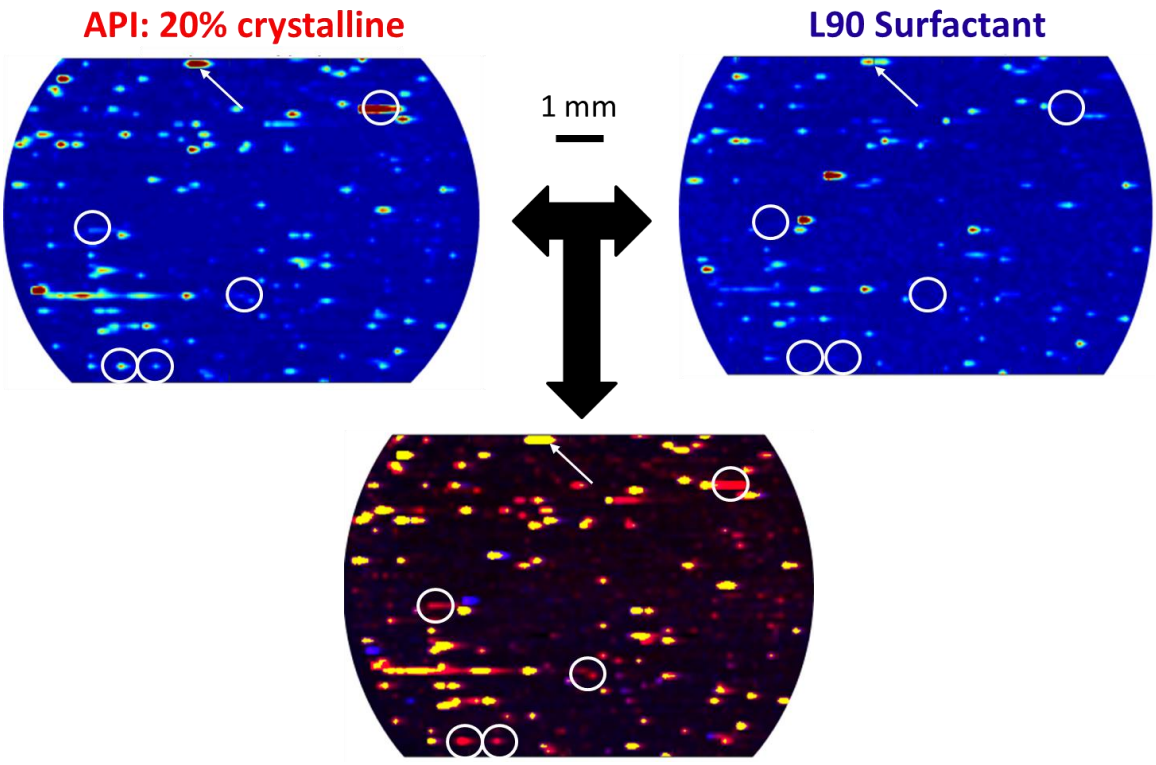

Figure 5. Co-localization MSI (bottom image) of 20% crystalline acetaminophen (APAP, top-left) and the L90 surfactant (top-right). The red represents signal from acetaminophen only, while the blue represents signal from only L90. The yellow shows where the acetaminophen and L90 signals overlap in the two MS-images. Areas circled show examples of identified crystalline acetaminophen. The white arrows point to an agglomeration of amorphous acetaminophen which has a corresponding surfactant signal.

Supplemental Figures:

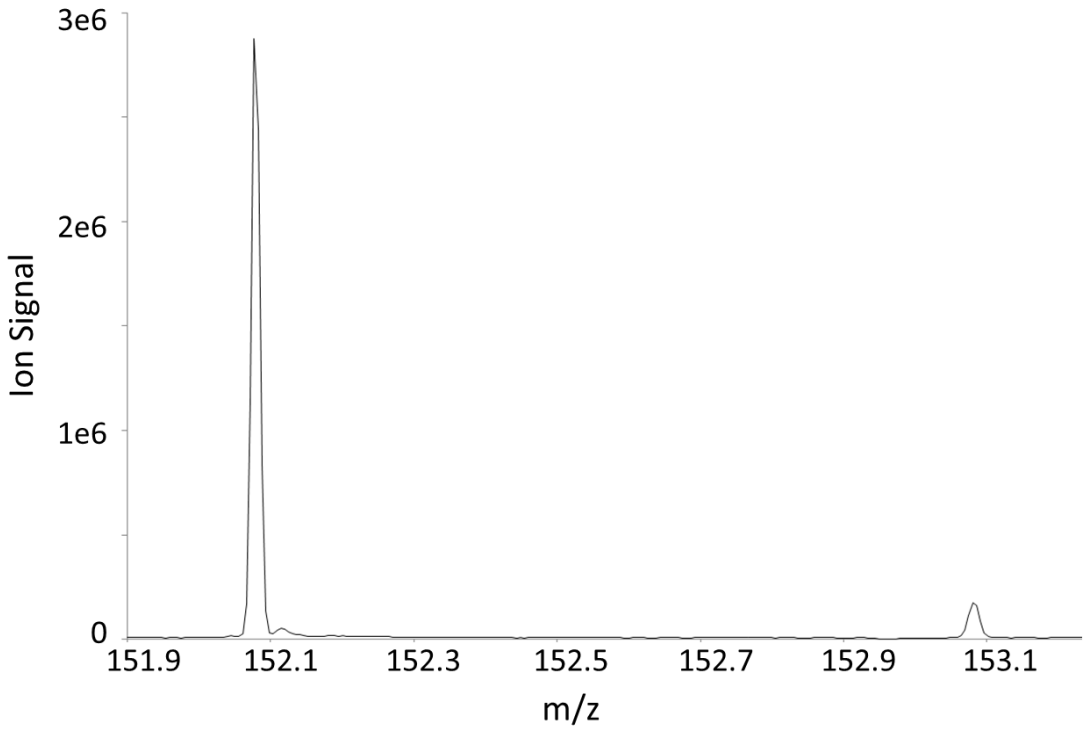

Supplemental Figure 1. Acetaminophen $[M+H]^+$ at a high intensity spot. Spectrum is not background subtracted. Peak just above m/z 152.0717 is a background ion.

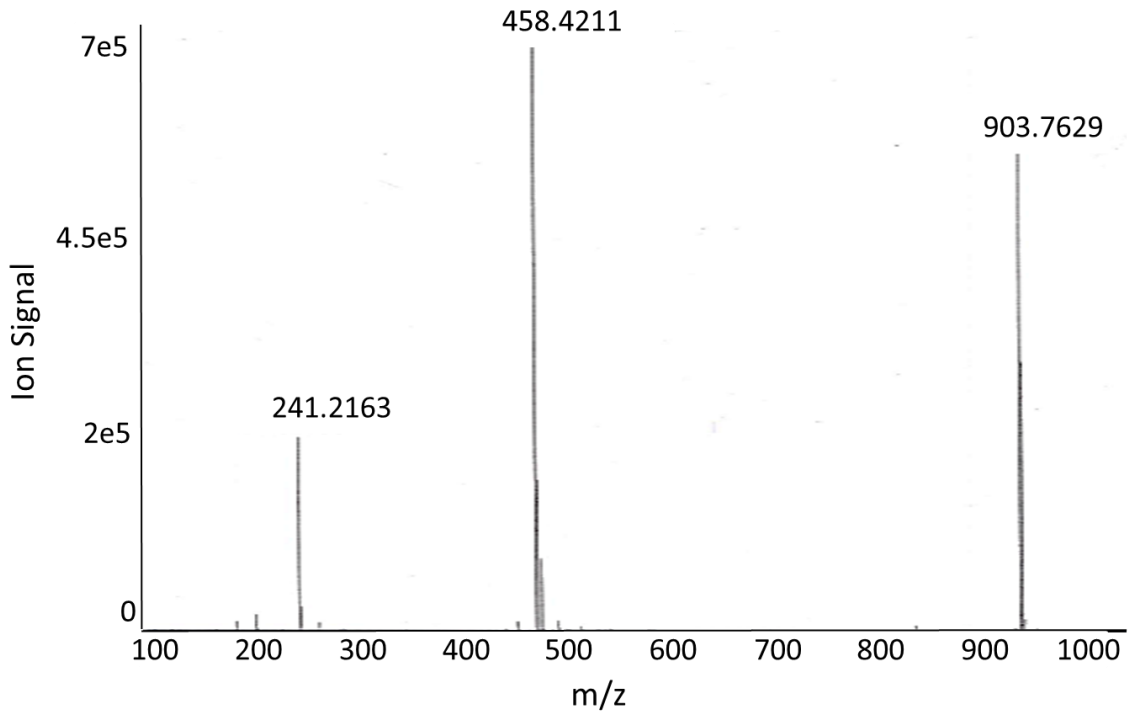

Supplemental Figure 2. LCMS of lauroglycol-90 surfactant standard.

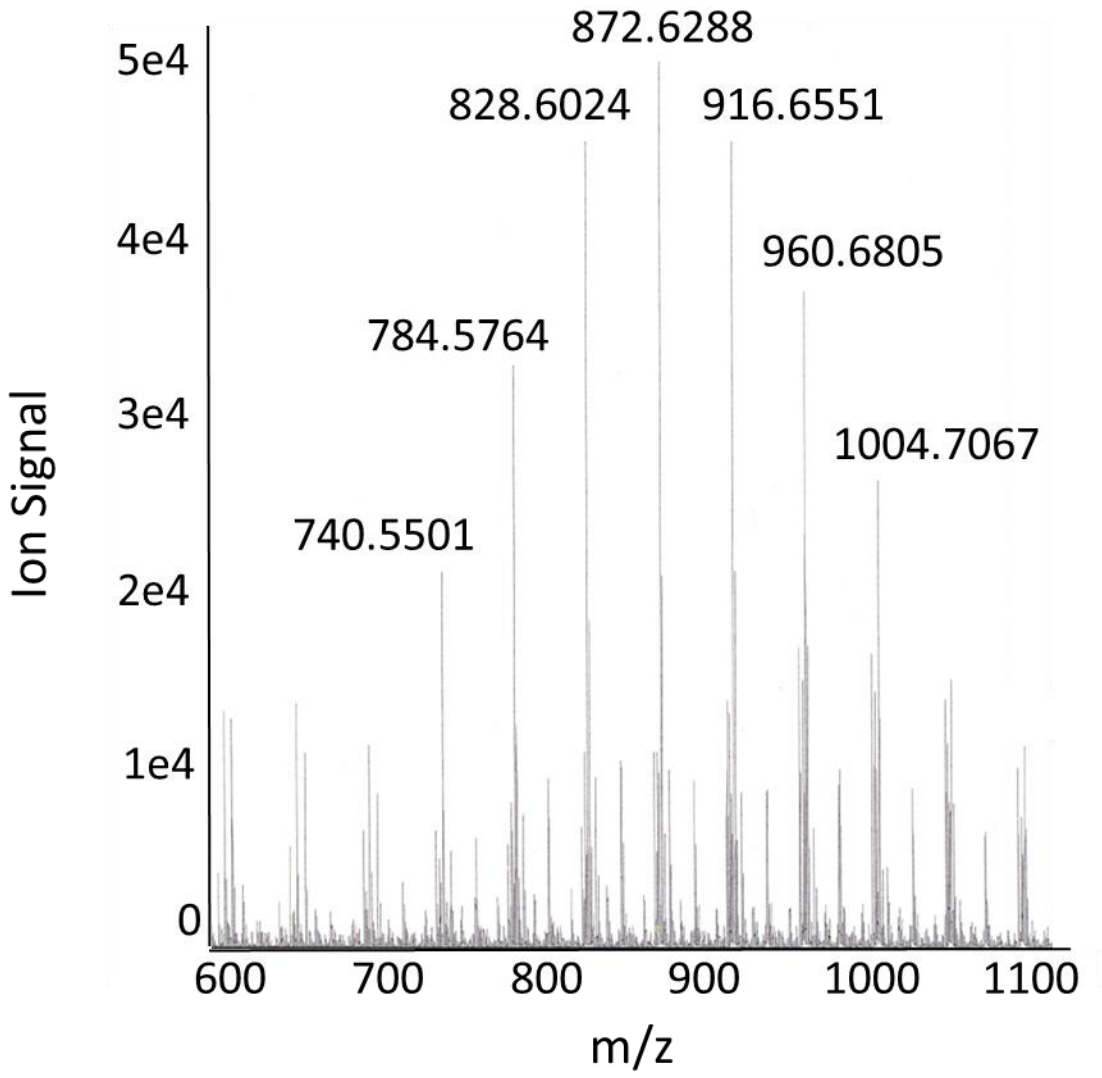

Supplemental Figure 3. LCMS of Tween-80 surfactant standard.

CHAPTER 6.

GENERAL CONCLUSIONS

This thesis discussed multiple applications of ELDI-MSI within the fields of plant metabolomics and one within pharmaceuticals. Also described were technical advancements of ELDI, including a lateral resolution increase to 50 µm. ELDI-MSI was successful in obtaining spatially resolved metabolite images from multiple plant samples, including: Peony, Marigold, Geranium, Hosta, Coleus, and Arabidopsis. Utilizing ELDI-MSI, spatial changes in the adaxial layer of coleus leaves as a result of external stimuli were interrogated. Isotopically labeled glucose was tracked in Arabidopsis plants through MS-images of amino acid isotopes. These studies showed the potential of ELDI-MSI in the field of plant metabolomics.

Agglomeration and crystallinity in pharmaceuticals directly affect the bioavailability of the active pharmaceutical ingredient(s) (APIs) in tablets. To diagnose agglomeration, ELDI-MSI was used on acetaminophen tablets and found intense spatial localization of the API as a result of increasing crystallinity. While this is typically done with spectroscopic imaging methods, MSI is advantageous due to its sensitivity and ability to image across the entire m/z acquisition range. ELDI-MSI is advantageous because it operates at ambient pressure and without any sample preparation for relatively flat tablets. This allows ELDI to be of potential use as an in-line monitor of crystallinity and agglomeration for the pharmaceutical industry.

Future work with ELDI-MSI would include an increase in the lateral resolution to ~20 µm. This would allow for improved images of smaller plants, such as Arabidopsis, and greater interrogation of crystals in tablets. Three-dimensional images of pharmaceutical tablets would also be worth exploring to determine where API agglomeration or crystals congregate in the pill. Also, a change of the laser to a more universal wavelength (such as 266 or 214 nm) would allow for analysis of pills without a TiO_2 dopant. The new ELDI-MSI setup would then be tested on commercial formulations to determine if crystallinity or agglomeration is observed in over-the-counter tablets.

APPENDIX A.

ANTHOCYANIN IMAGING IN *SOLENOSTEMON SCUTELLARIOIDES* (COLEUS) LEAVES USING ULTRAVIOLET LASER ABLATION ELECTROSPRAY IONIZATION MASS SPECTROMETRY

Galayda, K.J[1,2]., Xie, B.[1,3], Alexander, L.[3], **McVey, P.A.**[1,2], Nikolau, B.[3] and Houk, R.S.[1,2]

[1]*The Ames Laboratory, Iowa State University, Ames, Iowa, 50011,USA*

[2]*Department of Chemistry, Iowa State University, Ames, Iowa, 50011, USA*

[3]*Department of Biochemistry/Biophysics & Molecular Biology, Iowa State University, Ames, Iowa, 5011, USA*

Abstract

A common horticultural plant *Solenostemon scutellariodes* (coleus) has diverse foliage colors and is ideal for studying the biological role of flavonoid compounds. Prior research has determined how these variations in leaf color are altered by varying light sources. However little research has been done to determine the types of flavonoid compounds present in coleus leaves. In this study, laser ablation electrospray ionization (LAESI) mass spectrometry imaging (MSI) was used to determine a specific class of flavonoids- anthocyanins, which were additionally, confirmed using liquid chromatography mass spectrometry (LC-MS). Two varieties of *Solenostemon scutellariodes* (coleus) were used for the study. Broad Street is anthocyanin-rich (dark

burgundy/red leaf edged in green), while Wizard Jade is anthocyanin-poor (a leaf with creamy white center and green outer margin). Broad Street Coleus was found to be abundant in malonylshisonin. In contrast, Wizard Jade Coleus showed lower levels of this anthocyanin. Mass spectrometry imaging (MSI) showed that the biosynthesis of malonylshisonin in Broad Street Coleus progressed from cyanidin to cyanidin-3-O-β-D-glucoside to cyanidin-3-(p-coumaroyl)-glucoside to shisonin and finally to malonylshisonin. LAESI was proven to be a sensitive technique in identifying small amounts of shisonin and malonylshisonin in specific spatial regions of Wizard Jade Coleus leaves. Spatial resolution is important when compounds are heterogeneously distributed. The use of LAESI-MSI can prove a useful source to study biological processes as it requires little sample preparation.

Introduction

Anthocyanins are part of a larger class of secondary metabolites called flavonoids. They are commonly found in leaves and act as a stress protector especially against ultraviolet (UV) damage, since anthocyanins readily absorb UV light. Anthocyanins induce the characteristic blue, red, or purple pigment in various plant tissues. Common anthocyanins include cyanidin, pelargonidin, and delphinidin, which all have a cyclic backbone structure that is positively charged. This positive charge allows anthocyanins to have unique biological roles, which vary depending on the plant species and the location of anthocyanins in the plant itself.[1] When anthocyanins are found primarily in seeds, their colors attract animals, thus aiding in seed dispersal.

Alternatively, in leaves they can protect the plant against stressors like harsh weather conditions, heavy metal contamination, and UV radiation, the latter being the most commonly studied.[1-10] When a leaf is subjected to UV radiation, particularly UVB light (280-320 nm), proteins, DNA, and cell membranes can be altered or destroyed.[11] Thus, the anthocyanins accumulated in epidermal cells can protect leaves by acting as a barrier due to their strong UV absorbance.[12,13]

While the protective role of anthocyanins is the same across plant species, anthocyanin synthesis can vary depending on the plant.[14] The precursors of all anthocyanin syntheses are malonyl-COA and p-coumaroyl-COA; the latter is shown in Figure 1. These two compounds eventually form tetrahydroxychalcone, which is converted to naringenin, then dihydrokaempferol (DHK). DHK is hydroxylated to become dihydroquercetin (DHQ) or dihydromyricetin (DHM). DHK, DHQ, and DHM are reduced to leucoanthocyanidins, pelargonidin, cyanidin, and delphinidin as common byproducts, depending on the plant. For example, petunias do not produce pelargonidin but can produce delphinidin, whereas maize can produce delphinidin but not pelargonidin.

Solenostemon scutellariodes (coleus), a horticulturally attractive plant with highly ornamental foliage, has been used in many studies involving the influence of light intensity on foliage color and growth.[15] As a member of the *Lamiaceae* (mint) family, coleus plants accumulate anthocyanins in the outer epidermal region of their leaves. Most studies involving anthocyanins in coleus involve manipulating the amount of UV and visible light the leaf receives.[16-18] For example, a study by Nguyen et al., noted changes in pigmentation when various coleus species were subjected to high intensity

light.[16] There seems to be little information, however, on the actual anthocyanin compounds present in coleus.

Mass spectrometry imaging (MSI) can be used to study this question. MSI is an emerging tool in the plant field. It has recently shown its capabilities not only in spatial localization of metabolites but also in providing new insights into biological pathways.[19] Several ionization techniques are used in MSI, including matrix assisted laser desorption ionization (MALDI), desorption electrospray ionization (DESI), and laser ablation electrospray ionization (LAESI).[20-22] It should be noted in the literature LAESI is closely related to matrix assisted laser desorption electrospray ionization (MALDESI) and electrospray laser desorption ionization (ELDI).[22]

Previous studies involving plant metabolite identification through various MSI techniques, including reduced and atmospheric pressure laser desorption ionization, have been conducted on peonies, marigolds, Arabidopsis, and rice leaves.[21,23-25] While each technique offers its own advantages and disadvantages, LAESI has become useful for metabolite identification in both plant and biological samples over recent years. One the biggest advantage of this type of analysis is the ease of sample preparation (i.e. no matrix coating). An experiment conducted by Nemes et al[20] using IR-LAESI (2.94 µm), found ion abundances in petite French marigold seedlings were ~10^2-10^4 enhanced compared to atmospheric pressure IR-MALDI.

A typical LAESI experiment is shown in Figure 2. A sample leaf is prepped for analysis, and undergoes ablation from the laser. The ablation results in the formation of a neutral plume from the sample, which is then ionized by a charged electrospray

stream. The newly formed ions enter the mass spectrometer and the m/z ratio is measured for all the ions present, resulting in a mass spectrum. To obtain an image, several hundred spectra are gathered together to be processed. A mass spectrometry image can now be produced for every compound found in the sample. In our setup, a UV laser (355 nm) was used partly because anthocyanins efficiently absorb UV light.[12,13]

To date, there have been no attempts to image anthocyanins in coleus. We believe that MSI can allow further insight into anthocyanin synthesis. In this study, two varieties of coleus were imaged, Broad Street (dark burgundy/red leaf edged in green; an anthocyanin rich variety) and Wizard Jade (creamy white center and green outer margin; an anthocyanin poor variety). LAESI was performed on both types of leaves to identify the anthocyanins present and their spatial localization in the leaf. Additionally, extractions and liquid chromatography (LC-MS) were performed for validation and quantification.

Experimental

Plant Maintenance and Light Conditions

Solenostemon scuttellarioides – Broad Street and Wizard Jade were purchased from a local greenhouse (Earl May, Ankeny, Iowa). All plants were transferred to LC1 Sunshine Mix soil (Sun Gro Horticulture, Bellevue, WA), watered weekly in a growth room at 22 °C under continuous illumination (2568 Lux or photosynthetic photon flux density 100 µmol of photons m^{-2} sec^{-1}). Leaves (three biological replicates) were

harvested and taken for each experimental platform: MS imaging, optical imaging and/or anthocyanin analysis through LC-MS.

Tissue Sectioning and Microscopy

Fresh leaf tissues were hand-sectioned along the longitudinal axis of the leaves using a vibratome at 70-100 µm for spatial imaging. Each section was immediately visualized using a BX-40 microscope equipped with an Axioplan software. It should be noted that MS was not done on these sections.

Anthocyanin Extraction and LC-MS

For anthocyanin analysis, harvested leaves were immediately flash-frozen using liquid nitrogen, dried using a vacuum lyophilizer and pulverized using a Mixer Mill 301(Retsch GmbH, Germany) in 2 mL Eppendorf tubes prior to extraction. The anthocyanin extractions were extracted as described by Wu e. al[26] in 1.5 ml tubes containing 5 mg of lyophilized tissues. Briefly, 300 µL of methanol/ water/ acetic acid (85:10:0.5; v/v) was added to lyophilized samples and sonicated for one hour in dark at 4˚C and then further incubated in the same conditions (dark, 4°C) for an additional two hours. The samples were then centrifuged for five minutes at 13,000 rpm and the liquid phase (supernatant/upper layer) was filtered twice using 13 mm x 0.45µm Teflon Syringe filters (Supelco, PA).

An Atlantis T3 column (2.1×150mm, 3µm, Waters, Milford, MA) was used for separation. Elution was performed using mobile phase A (5% formic acid in LC-MS grade

water) and mobile phase B (5% Formic acid in methanol). The flow rate was kept at a 0.2mL/min. When a 5 µL of sample was injected, a gradient was used as follows: 0-6 min, 0-20% B; 6-40 min, 20-50% B; 40-44 min, 50-50% B; 44-48 min, 50%-100% B; 48-52 min, 100-100% B; 52-56 min, 100-0% B.

Chromatographic separations were performed with an 1100 series HPLC (Agilent Technologies). This was attached to an Agilent 6210 MSD time-of-flight mass spectrometer with an electrospray ionization (ESI) source. The ESI capillary voltage was +3.0 kV, nitrogen gas temperature was set to 350 ˚C, drying gas flow rate was 11 L/min, nebulizer gas pressure was 35 psi, skimmer was 65 V, and OCT RF was 250 V. Mass data from mass range 100-2000 were collected and analyzed using Agilent DataAnalysis.

Individual anthocyanin peak areas were generated using the QuantAnalysis, and then were used to quantitatively compare the different level of each anthocyanins expressed. The tentative structure identification for each anthocyanin was interpreted through MS/MS performed with various collision energy (25-35 eV).

Sample Preparation for LAESI-MSI

Leaves were cut from the plant using scissors and placed in a petri dish over a damp filter paper to prevent drying until ready for ablation. Both the petri dish and the scissors were washed in acetone prior to handling. No additional treatment or matrix was applied. Once the samples were ready to be ablated, they were mounted onto glass microscope slides with double sided tape and placed on a xyz- translation stage

(Z825B, Thorlabs, Inc. Newton, NJ). The samples were positioned 8 mm below the electrospray axis and translated at a rate 0.4 mm/s.

LAESI Source

A 53 µm i.d. polyimide-coated capillary was positioned with the tip approximately 10 mm from the cone inlet of the mass spectrometer. A mixture of methanol and water (1:1 v/v) with a 0.1% formic acid solution (purity ≥ 99.5%, Fischer Scientific) was pumped through the capillary by a syringe pump (Model 22, Harvard Apparatus, South Natick, MA) at a rate of 0.6 µl/min. Leucine-enkaphalin (0.1 ppm, Waters) was added to the electrospray solution as a lockspray mass calibrant. The ESI voltage was +2.7 kV.

A 355 nm Nd:YAG ultraviolet laser (ULTRA, Big Sky Laser Tech, Inc., Bozeman, MT) was used. Typical laser pulses of 250 µJ/pulse energy were focused to ~125 µm spot size by a 75 mm fused-silica plano-convex focusing lens. The laser was operated at 10 Hz with a 5 ns pulse width.

LAESI Mass Spectrometer

A Waters Synapt G2-S quadrupole time-of-flight mass spectrometer was used in these experiments. The mass spectrometer was modified by removing the ESI source enclosure. To bypass any electrical connections from this enclosure an adaptor, provided by Waters, was used. During a normal MS acquisition, the quadrupole collision energy was kept at a preset voltage of 30 eV. During tandem MS, the collision energy

was nominally 20 to 30 eV. The TOF mass analyzer was operated in sensitivity mode, with a mass resolution of approximately m/Δm 10,000 (FWHM). Mass spectra were recorded from 50 to 2000 m/z. The time-of-flight extraction events were not synchronized to the laser pulses.

LAESI Data Processing

Mass spectra were generated from total ion chromatograms using MassLynx V4.1 (SCN851) software provided by Waters. Peak assignments from these chromatograms were based on accurate mass measurements, tandem MS analysis, and database searches including METLIN[27], KEGG[28], and MetCyc[29]. These databases were last accessed on September 20, 2016.

To generate images, MassLynx *.raw data files were converted into mzML files using the Proteowizard Mass ConverterTool[30]. The mzML files were then converted into imzML files using imzMLConverter[31]. The imzML files were then made into black and white images in DatacubeExplorer[32] which were then converted to false-color images in GIMP 2.8.

Results and Discussion

Leaf color variations

Foliage color differences between Wizard Jade and Broad Street were visualized at a magnification of 10x using 100 µm thick hand-sections (Fig. 3). Both coleus cultivars showed no anthocyanin accumulation on the lower epidermal layers of the leaf. The

green pigments accumulated in chloroplast cells of the mesophyll and palisade layers imparting the differences in leaf color. In Broad Street coleus anthocyanins accumulated only in the upper epidermal layers of the leaf, no anthocyanins were found in Wizard Jade. This was expected considering the lack of a visual purple coloring.

Anthocyanin Identification by LC-MS and LC-MS/MS

Identification and peak assignment of anthocyanins were primarily based on the molecular weight, MSMS fragmentation and references.[26] The chromatogram from the red portion of Broad Street is shown in Figure 4. Table 1 gives tentative assignments for five major anthocyanins and their corresponding MSMS fragments. It should be noted that exact linkages among these structures were not able to be identified because the corresponding standards were not available for comparison.

Similar anthocyanin extraction and LCMS detection were performed on the creamy white area of Wizard Jade. As indicated in Figure 4, anthocyanins detected from the red portion of Broad Street were not detected in Wizard Jade. This is typical as the extracted solution from wizard jade is yellow and believed to not contain anthocyanins.

LAESI-MSI of Broad Street and Wizard Jade

A representative background subtracted positive-ion mass spectrum (integrated from one laser ablation trench over the course of 50 s) from Broad Street coleus is shown in Fig. 6a. The most abundant ion signals that were observed included peaks representing the anthocyanins, cyanidin and malonylshisonin at m/z 287.0550 and

843.1984. Other observable anthocyanins included apigenen (m/z 271.0615), Cyanidin-3-(p-coumaroyl)-glucoside (m/z 595.1451), and Cyanidin 3-(6”-p-coumarylglucoside)-5-4”, 6”-dimalonylglucoside (m/z 929.1982). Other anthocyanins and their suggested assignments are listed in Table 2. Linkage positions were based on literature, and were measured in present work.[14]

Figure 6b shows a representative background subtracted positive-ion mass spectrum (integrated from one laser ablation trench over the course of 50 seconds) from Wizard Jade coleus. This spectrum is very from that of Broad Street. The most abundant ions observed included caffeic acid $-H_2O + H^+$ at m/z 163, kaempferol at m/z 287.0570, and unknown ions at m/z 351 and 399. Lower abundance ions showed the presence of carotenoids and lipids and are listed in table 2. The integrated mass spectra did not show the presence of anthocyanins.

For both variety of leaves, tandem MS measurements were taken and compared to databases. Collision energies ranged from 15-30 eV. Representative spectra can be found in the supplementary materials. Furthermore, tandem MS measurements of Broad Street coleus were compared to the LC-MS/MS data.

Anthocyanin Imaging in Broad Street Coleus and the Malonylshisonin Pathway

Figure 7 shows the pre-ablation optical image and false-color ion maps for anthocyanins in Broad Street coleus. For the images shown, there are 35 ablation tracks 125 µm wide × 250 µm apart. Each ablation track took 50 s at a speed of 0.5 mm/s.

As expected, anthocyanins were concentrated in the red area of the leaf, particularly in the areas around the veins. This is understandable as veins transport anthocyanins to various parts of the leaves, and a small reserve of anthocyanins is stored in the veins for times of stress.[33,34] The only anthocyanin spatial images which appear to have some accumulation in the green area are those for cyanidin (m/z 287.0550) and cyanidin-3-O-β-D-glucoside (m/z 449.1084). These ions are isomers of the flavonoids kaempferol and kaempferol-3-O-β-D-glucoside. Tandem MS measurements were taken of both ions in the green and red portions of Broad Street coleus. Representative tandem MS spectra of the isomers cyanidin and kaempferol is show in Figure 8a. These results show that cyanidin was present in the red portion, while kaempferol was present in the green portion, shown by tandem MS measurements on a new Broad street leaf (figure 8b). MS/MS was taken of a single line in the green portion while a separate line was ablated in the red portion. Collision energies were 20 eV.

Malonylshisonin was the most abundant anthocyanin present in Broad Street coleus. It has been studied previously in *Perilla ocimoides* leaves and has a structure of *3-0-(6-0-(* E)-p-coumaryl-p- D-glucopyranosyl)-5-0-(6-0-malonyl-p- D-gluco pyranosyl)cyanidin.[35] It is the final product of the super pathway of malonylshisonin biosynthesis, which is common in plants and higher organisms (Fig. 9).[36-38] The pathway begins with cyanidin (287.0555 Da) which becomes cyanidin-3-O-β-D-glucoside (449.1084 Da). The pathway than splits into either cyanidin-3,5-di-O-β-D-glucoside (611.1612 Da) or cyanidin-3-(p-coumaroyl)-glucoside (595.1451 Da). The pathway then

converges to form shisonin (757.1980 Da) and eventually malonylshisonin (843.1984 Da).

Using mass spectrometry imaging, we were able to determine that malonylshisonin is formed in Broad Street coleus through cyanidin-3-(p-coumaroyl)-glucoside. The ion, cyanidin-3,5-di-O-β-D-glucoside, was not present in the mass spectrum, thus this pathway was not used. To verify that this ion can be seen with our instrument, another variegated hybrid of coleus, Mosaic, was tested. Cyanidin-3,5-di-O-β-D-glucoside (m/z 611.1513) was present in mosaic**.**

Anthocyanin Imaging in Wizard Jade Coleus

Upon initial review of the LC-MS and spatially integrated LAESI-MS data, no anthocyanins were found in Wizard Jade coleus. However, when images were processed, shisonin and malonylshisonin were present in a small portion of the leaf and at very low intensities. Upon further inspection, only a single time resolved mass spectrum at 1.35 min in a 2 minute acquisition showed these ions. Figure 10 shows the time resolved mass spectrum from abaltion trench 27. Shisonin and malonylshisonin were present in the stem of the leaf which we believe are there to protect the leaf from damage, much like the reserves found in the veins of Broad Street coleus.[33,34] The spatial resolution of LAESI-MS allowed measurement of these low –abundance compounds, which were not found by chemical extraction techniques, like LC-MS. MS images were made for other compounds found in Wizard Jade (such as carotenes) and can be found in supplementary materials.

Conclusions

Studies have reported that anthocyanins are water soluble pigments that contribute to the red coloration in coleus plants. These pigments are synthesized in the cytoplasm and actively transported and accumulate in the vacuoles of epidermal or mesophyll cells. To determine anthocyanin variations in both Broad Street and Wizard Jade coleus leaves laser ablation electrospray ionization was used. The use of an ultraviolet laser in this experiment helped any anthocyanins present in the samples to easily be absorbed and detected in the mass spectrometer. Several anthocyanin species were identified in Broad Street, but more surprisingly, anthocyanins were detected in Wizard Jade, a green and yellow variety of coleus. Two interesting compounds, shisonin and malonylshisonin, were found only in a few localized areas of the leaves and could not be observed by spatially-integrated methods.

When LAESI is coupled with mass spectrometry imaging, we were also able to determine the steps in the malonylshisonin biosynthesis pathway. Since there is little sample preparation, LAESI MSI is a quicker, sensitive option than assays or other forms of mass spectrometry to investigate biological processes in plants. Our results showed that Broad Street coleus favored unique steps in the malonylshisonin biosynthesis pathway and also demonstrated the sensitivity of LAESI in detection of small abundant molecules in coleus Jade.

Acknowledgments

The Authors would like to thank the US Department of Energy (DOE), the Office of Basic Energy Sciences, Division of Chemical Sciences, Geosciences, and Biosciences. The authors would also like to thank the Ames Laboratory which is operated by Iowa State University under DOE contract DE-AC02-07CH11358.

References

1) Holton, T.A., Cornish, E.C., Genetics and Biochemistry of Anthocyanin Biosynthesis. *The Plant Cell.* **1995**, 7: 1071-1083.
2) Burns K.C., Dalen J.L., Foliage color contrasts and adaptive fruit color variation in a bird-dispersed plant community. *Oikos*. **2002**, 96(3):463–469.
3) Chalker-Scott L., Environmental significance of anthocyanins in plant stress responses. *Photochem Photobiol*. **1999**, 70(1):1–9.
4) McKown R, Kuroki G, Warren G. Cold responses ofArabidopsis mutants impaired in freezing tolerance. JExpBot. 1996;47(305):1919–1925.
5) Nozzolillo C, Isabelle P, Andersen OM, Abou-Zaid M. Anthocyanins of Jack Pine *(Pinus banksiana)* seedlings. *Can J Bot*. **2002**, 80(7):796–801.
6) Mendez M., Gwynn-Jones D., Manetas Y., Enhanced UV-B radiation under field conditions increases anthocyanin and reduces the risk of photoinhibition but does not affect growth in the carnivorous plant *Pinguicula vulgaris*. *New Phytol*. **1999**, 144(2): 275–282.
7) Solecka D., Kacperska A., Phenylpropanoid deficiency affects the course of plant acclimation to cold. *Physiol Plant*. **2003**, 119(2):253–262.
8) Hale K.L., McGrath S.P., Lombi E., et al., Molybdenum sequestration in Brassica species. A role for anthocyanins?. *Plant Physiol*. **2001**, 126(4):1391–1402.
9) Hale K.L., Tufan H.A., Pickering I.J., et al., Anthocyanins facilitate tungsten accumulation in Brassica. *Physiol Plant*. **2002**, 116(3):351–358.
10) Krupa Z., Baranowska M., Orzol D,. Can anthocyanins be considered as heavy metal stress indicator in higher plants?. *Acta Physiol Plantarum*. **1996**, (18): 147–151.
11) Jansen, M.A.K., Gaba, V., Greenberg, B.M., Higher plants and UV-B radiation: Balancing damage, repair and acclimation. *Trends Plant Sci*. **1998**, (3): 131-135.
12) Stapleton, A.E., Ultraviolet radiation and plants: Burning questions. *Plant Cel.l* 1992, (4): 1353-1358.
13) Markham K.R., Techniques of Flavonoid Identification. *London, UK: Academic Press.* **1982**.
14) Holton, T., Cornish, E., Genetics and Biochemistry of Anthocyanin Biosynthesis. *The Plant Cell*. **1995**, (7): 1071-1083.

15) Nishimura T., Ohyama K., Goto E., Inagaki N., Morota T., Ultraviolet B radiation suppressed the growth and anthocyanin production of Perilla plants grown under controlled environments with artificial light. *Acta Hortic*. 2008, 797: 425–429.
16) Nguyen P., Valeriano D., The role of light on foliage colour development in coleus (Solenostemon scutellarioides (L.) Codd). *Plant Physiology and Biochemistry.* **2009**, 47: 934–945.
17) Burger J., Edwards G., Photosynthetic Efficiency, and Photodamage by UV and Visible Radiation, in Red versus Green Leaf Coleus Varieties . *Plant Cell Physiol*. **1996**, 37(3): 395-399.
18) Chalker-Scott, L., Do Anthocyanins Function as Osmoregulators in Leaf Tissues? *Advances in Botanical Research.* **2002**, 37: 103–106.
19) Lee Y. J., Perdian D. C., Song Z., Yeung E. S., Nikolau B. J., Use of mass spectrometry for imaging metabolites in plants. *The Plant Journal*. **2012**, 70: 81–95.
20) Nemes P., Vertes A., Laser ablation electrospray ionization for atmospheric pressure, in vivo, and imaging mass spectrometry. *Anal. Chem*. **2007**, 79: 8098.
21) Robichaud G., Barry J., Muddiman D., IR-MALDESI mass spectrometry imaging of biological tissue sections using ice as a matrix. *J Am Soc Mass Spectrom*. 2014, 25:319–328.
22) Boughton B.A., Thinagaran D., Sarabia D., Bacic A., Roessner, U., Mass spectrometry imaging for plant biology: a review. *Phytochem Rev.* **2016**, 15:445–488.
23) Lee Y. J., Perdian D. C., Song Z., Yeung E. S., Nikolau, B. J. Use of mass spectrometry for imaging metabolites in plants. *The Plant Journal*. 2012, 70: 81–95.
24) Klein A., Yagnik G., Hohenstein J., Zhiyuan J., Zi J., Reichert M., MacIntosh G., Yang B., Peters R., Vela J., Lee Y-L., Investigation of the Chemical Interface in the Soybean–Aphid and Rice–Bacteria Interactions Using MALDI-Mass Spectrometry Imaging. *Anal. Chem.* **2015**, 87 (10): 5294–5301.
25) Shroff R., Schramm K., Jeschke V., Nemes P., Vertes A., Gershenzon J., Svatos A., Quantification of plant surface metabolites by MALDI mass spectrometry imaging: glucosinolates on *Arabidopsis thaliana* leaves. *The Plant Journal.* **2015**. 81: 961-972.
26) Wu, X., Gu, L., Prior, R. L. & Mckay, S. Characterization of Anthocyanins and Proanthocyanidins in Some Cultivars of Ribes, Aronia, and Sambucus and Their Antioxidant Capacity. *Journal of Agricultural and Food Chemistry.* **2004.** 52: 7846–7856.
27) Smith C.A., O'Maille G., Want E.J., Qin C., Trauger S.A., Brandon T.R., Custodio D.E., Abagyan R., Siuzdak G., METLIN: a metabolite mass spectral database. *Ther Drug Monit* [Internet]. **2005**, 27 :747-51. https://metlin.scripps.edu/
28) Kegg Pathway database search. http://www.genome.jp/kegg/pathway.html
29) MetaCyc Compound Search. https://metacyc.org/cpd-search.shtml
30) Chambers M.C., MacLean, B., Burke R., Amode D., Ruderman D.L., Neumann S., Gatto L.,Fischer B., .Pratt B., Egertson J., Hoff K., Kessner D., Tasman N., Shulman N., Frewen B., Baker T.A., BrusniakM.-Y., Paulse C., Creasy D., Flashner L., Kani K.,

Moulding C., Seymour S.L., Nuwaysir L.M., Lefebvre B., Kuhlmann F., Roark J., Rainer P., Detlev S., Hemenway T., Huhmer A., Langridge J., Connolly B., Chadick T., Holly K., Eckels J., Deutsch E.W., Moritz R.L, Katz J.E., Agus D.B., MacCoss M., Tabb D.L., Mallick P., A cross-platform toolkit for mass spectrometry and proteomics. *Nature Biotechnology.* **2012**, 30:918.

31) Race I.M., Styles I.B., Bunch J., Inclusive sharing of mass spectrometry imaging data requires a converter for all. *J. Proteomics.* **2012**, *75*: 5111.

32) Klinkert I., Chughtai K., Ellis S.R., Heeren R.M.A., Methods for full resolution data exploration and visualization for large 2D and 3D mass spectrometry imaging datasets. *Int. J. Mass Spectrom*. **2014**, 362: 40.

33) Hughes N. M., Neufeld H. S., Burkey, K. O., Functional role of anthocyanins in high-light winter leaves of the evergreen herb ***Galax urceolata***. *New Phytologist*. **2005**, 168: 575–587.

34) Steyn W. J., Wand S. J. E., Holcroft D. M. Jacobs G., Anthocyanins in vegetative tissues: a proposed unified function in photoprotection. New Phytologist. 2002, 155: 349–361.

35) Kondo T., Tamura H., Yoshida K., Goto T., Structure of Malonylshisonin, a Genuine Pigment in Purple Leaves of Perilla ocimoides L. var. crispa Benth. Agric. Bioi. Chern. 1989, 53 (3):797-800.

36)Fujiwara H., Tanaka Y., Fukui Y., Ashikari T., Yamaguchi M., Kusumi T., Purification and characterization of anthocyanin 3-aromatic acyltransferase from Perilla frutescens**.** *Plant Science*. **1998,** 137: 87-94.

37)Yonekura-Sakakibara K., Tanaka Y., Fukuchi-Mizutani M., Fujiwara H., Fukui Y., Ashikari T., Murakami Y., Yamaguchi M., Kusumi T., Molecular and biochemical characterization of a novel hydroxycinnamoyl-CoA: anthocyanin 3-O-glucoside-6"-O-acyltransferase from Perilla frutescens. *Plant Cell Physiol.* **2000**, 41(4): 495-502.

38) Yamazaki M., Gong Z., Fukuchi-Mizutani M., Fukui Y., Tanaka Y., Kusumi T, Saito K., Molecular cloning and biochemical characterization of a novel anthocyanin 5-O-glucosyltransferase by mRNA differential display for plant forms regarding anthocyanin**.** *J Biol Chem*. **1999**, 274(11): 7405-11.

Table A1. Metabolites identified in Broad Street and Wizard jade coleus by LC-MS.

Peak	$[M]^+$ (m/z)	MS/MS fragments (m/z)	Proposed Anthocyanin Structure
3	757.3	287.0,449.0,595.1	Cyanidin 3-O-(6-O-p-coumaroyl)glucoside-5-O-glucoside
6	857.3	287.0, 549.1, 595.1	Cyanidin-3-rutinoside-5-succinyl-glucoside
7	857.3	287.0 595.2,649.1	Cyanidin-3-rutinoside-5-succinyl-glucoside
8	843.3	287.0, 535.0, 595.1, 799.1	Cyanidin-3-3-O-(6-O-p-coumaroyl)glucoside-5-malonyl-glucoside
9	957.3	287.0, 595.2, 649.1	Cyanidin-3-rutinoside-5-(succinyl)(succinyl)-glucoside
10	957.4	287.0, 595.2, 649.1	Cyanidin-3-rutinoside-5-(succinyl)(succinyl)-glucoside
11	943.3	287.0, 595.2, 635.1	Cyanidin-3-rutinoside-5-malonyl-succinyl-glucoside

Table A2. Metabolites identified in Broad Street and Wizard jade coleus by UV-LAESI under atmospheric pressure. Carotenes in Jade coleus are suggested due to mass defect of ~0.4xxx.

Plant	Suggested Assignment	Mean Measured (Da)	Accurate Mass (Da)	Δppm	Measured Product Ions
Broadstreet	Caffeic Acid	163.0364	163.0395	19	145,135,117,89
	Apigenin	271.0615	271.0606	3	212,194,153
	Cyanidin	287.0550	287.0550	0	
	Rosmarinate	383.0751	383.0737	3	271,221,163
	Cyanidin 3-O-(6-O-p-coumaroyl) glucoside	595.1451	595.1446	0.8	287
	Shisonin	757.1926	757.1974	6	595, 449, 287, 147
	Malonylshisonin	843.1984	843.1978	0.7	595, 535, 287
	Cyanidin 3-(6”-p-coumarylglucoside)-5-4”, 6”-dimalonylglucoside	929.1982	929.1982	0	843,621, 595, 287
Jade	Caffeic Acid	163.0364	163.0395	19	145,135,117,89
	Apigenin	271.0636	271.0606	11	212,194,153
	Kaempferol	287.0557	287.0550	2	
	ID Unknown	351.1137	--	--	333,191,163
	Rosmarinate	383.0751	383.0737	3	271,221,163
	ID Unknown	399.0544	--	--	383, 353, 296, 163
	ID Unknown-possible carotene	651.4186	--	--	637, 581
	ID Unknown-possible carotene	813.4608	--	--	271, 163
	ID Unknown-possible carotene	911.6208	--	--	271, 163
	ID Unknown-possible carotene	975.4839	--	--	637

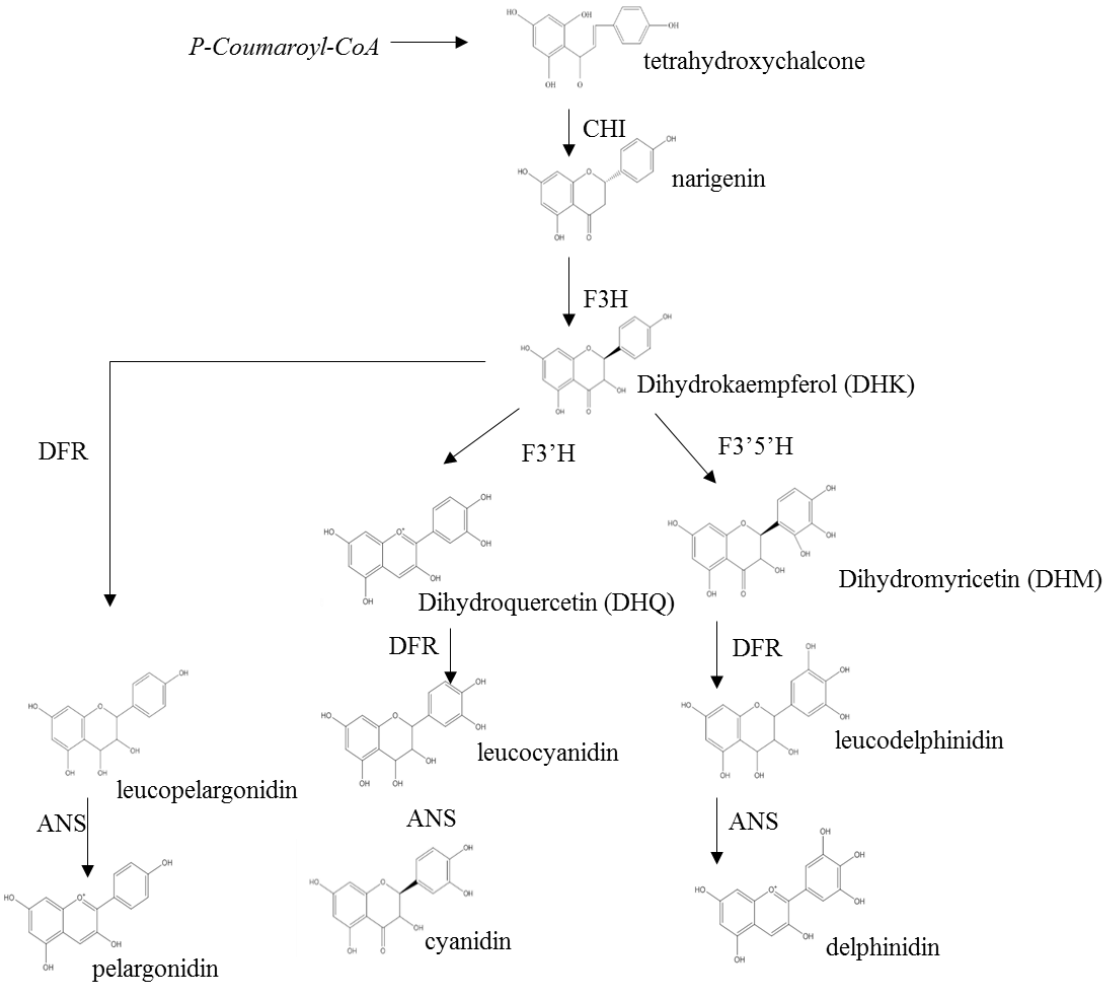

Figure A1. Anthocyanin biosynthesis. F3H is flavonone 3-hydroxylase, F3'H is flavonoid 3'-hydroxylase, F3'5'H is flavonoid 3'5'-hydroxylase, DFR is dihydroflavonol 4-reductase, and ANS is anthocyanidin synthase.

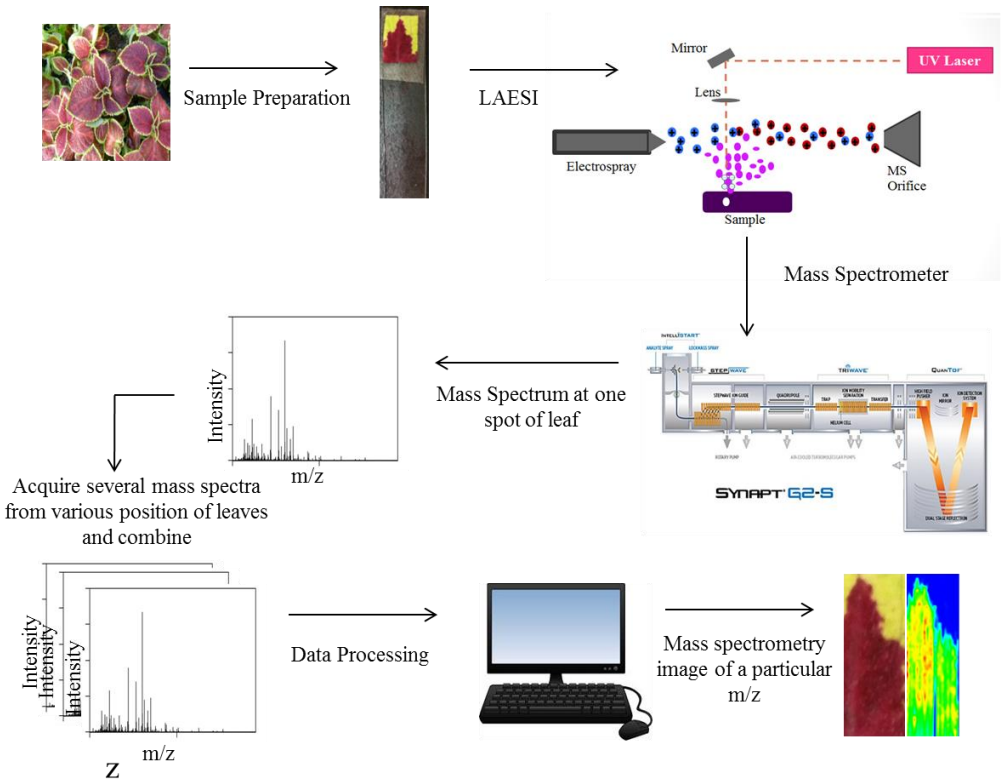

Figure A2. Typical LAESI-MSI experiment**.** Once the leaves are picked, they are put attached to a glass slide by double sided tape. The sample is ablated by a UV laser and an external electrospray source turns the ablated sample into ions. These ions can enter the mass spectrometer and an individual mass spectrum is produced. Over the course of an imaging run, every time the laser hits the sample, a mass spectrum is produced. Every individual spectrum is combined and data processed. Images can now be created for all m/z.

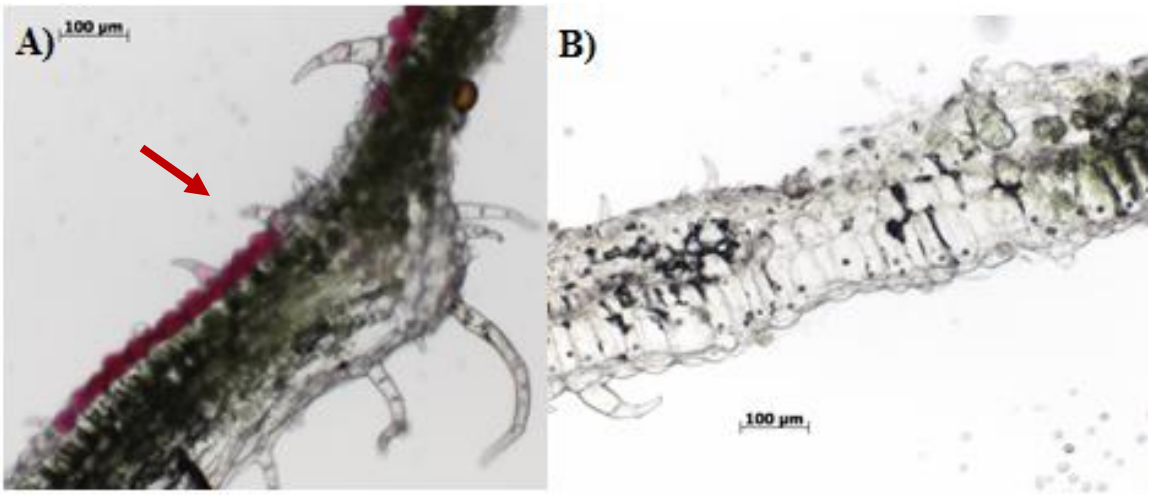

Figure A3. Tissue sectioning of coleus leaves at 100 µm thickness and a magnification of 10X. A) Tissue section of broadstreet coleus. Anthocyanins (red spots, indicated by red arrow) are accumulated on the upper epidermal layer of the leaf. B) Tissue section of Jade coleus. No anthocyanins are present, although there is a greater accumulation of chlorophyll than Broadstreet coleus**.**

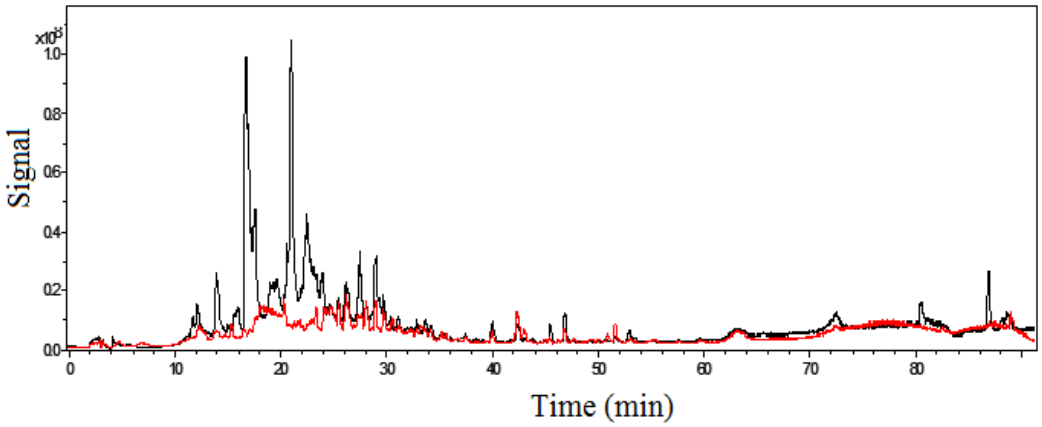

Figure A4. LC-MS comparison of Broadstreet coleus (black) and wizard jade (red). No anthocyanins were found in wizard jade.

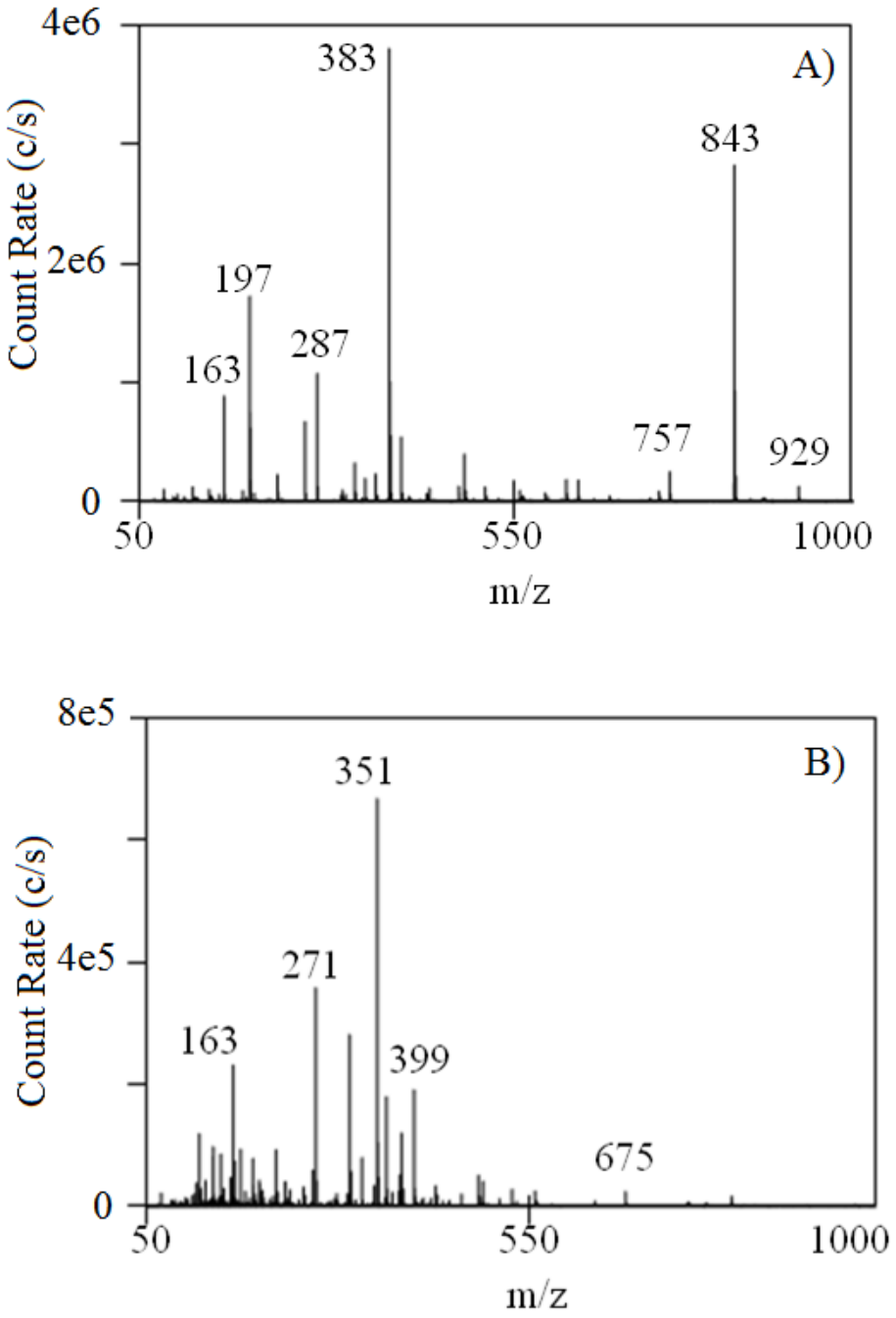

Figure A5. Integrated positive ion mass spectrum obtained from one ablation track in A) Broad Street coleus and B) Wizard Jade coleus. The ESI background has been subtracted from these LAESI spectra.

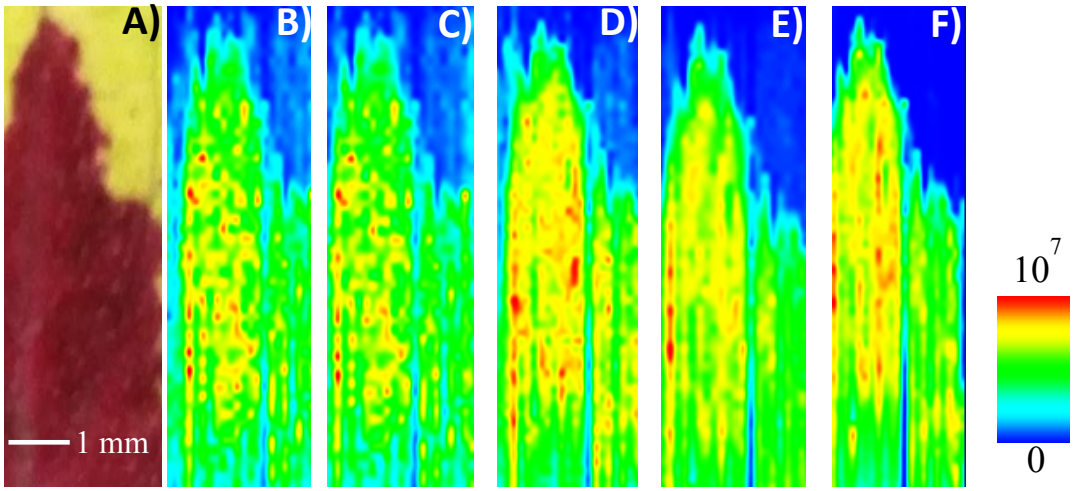

Figure A6. Images for positive ions from broadstreet coleus. a) Optical photograph before ablation. False color ion maps of broadstreet at b) m/z 287.0535, cyanidin, c) m/z 449.1177, Cyanidin-3-O-β-D-glucoside, d) m/z 595.1498, Cyanidin-3-(p-coumaroyl) glucoside, e) m/z 757.1926, shisonin, and f) m/z 843.2001, malonylshisonin.

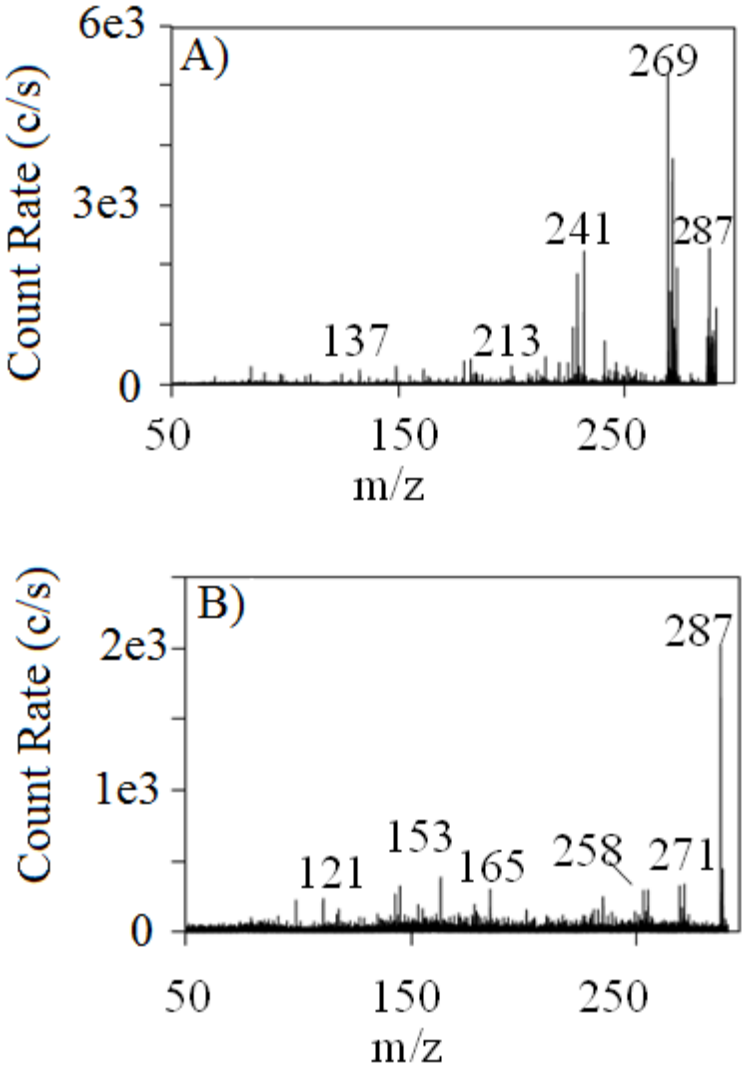

Figure A7. Typical tandem MS results for isomeric positive ions from broadstreet: A) tandem MS of spectrum of cyanidin and, B) tandem MS spectrum of kaempferol. The collision energies for these experiments were 30 eV.

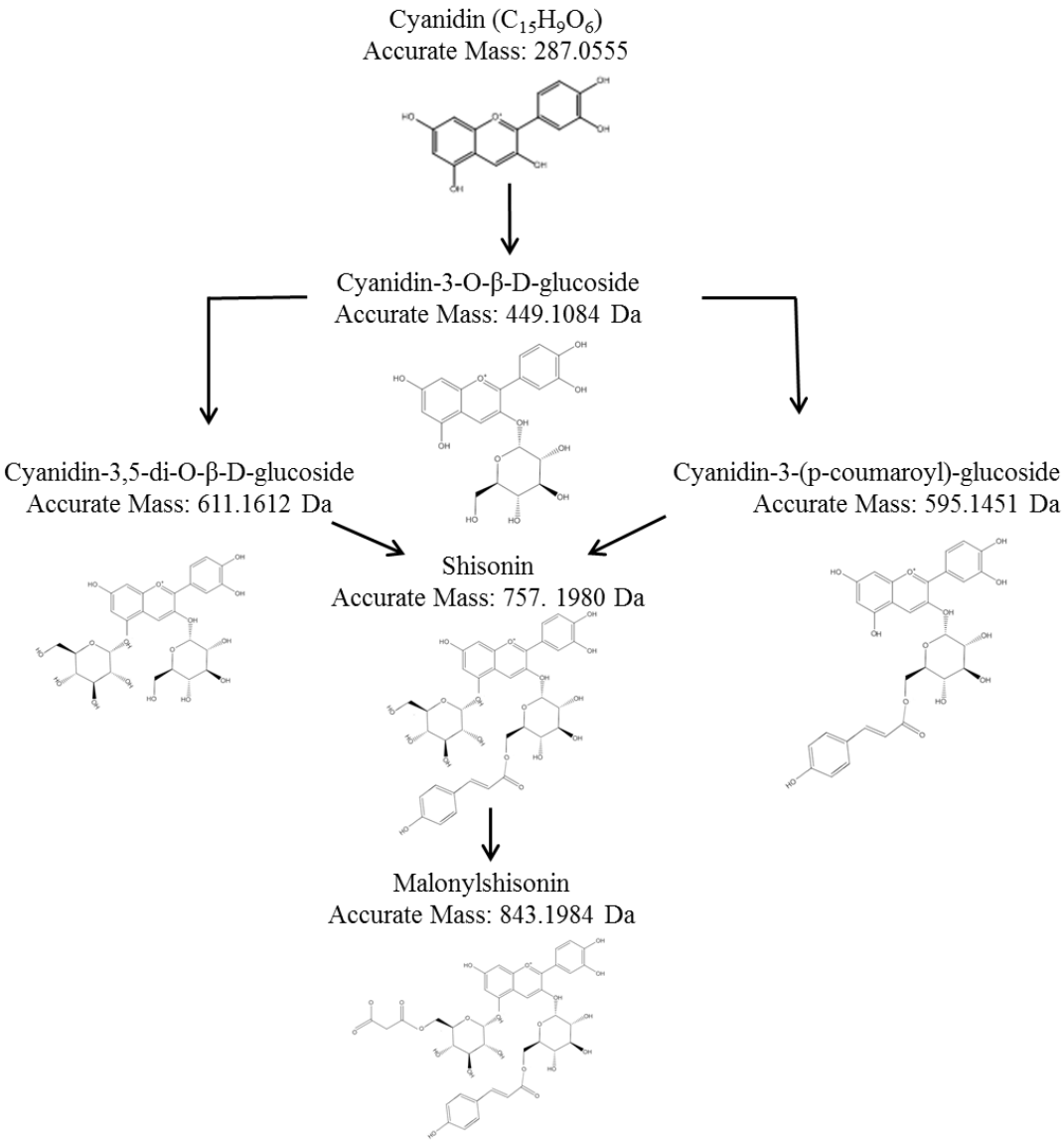

Figure A8. The biosynthetic pathway of malonylshisonin from cyanidin.

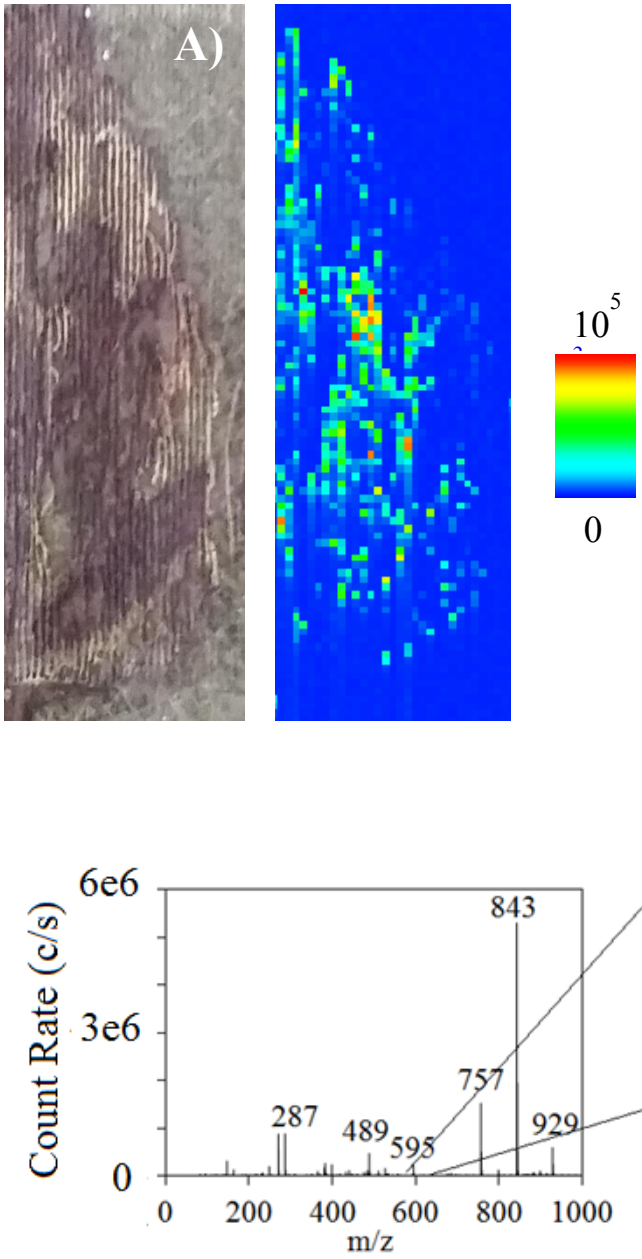

Figure A9. Mosaic coleus. A) image for cyanidin-di-glucoside (m/z 611.1513 Da). B) Integrated positive ion mass spectrum obtained from one ablation track in mosaic coleus acquired by atmospheric-pressure UV-LAESI. The ESI background has been subtracted from this LAESI spectrum. Inset shows the presence of cyanidin-di-glucoside at m/z 611.1513.

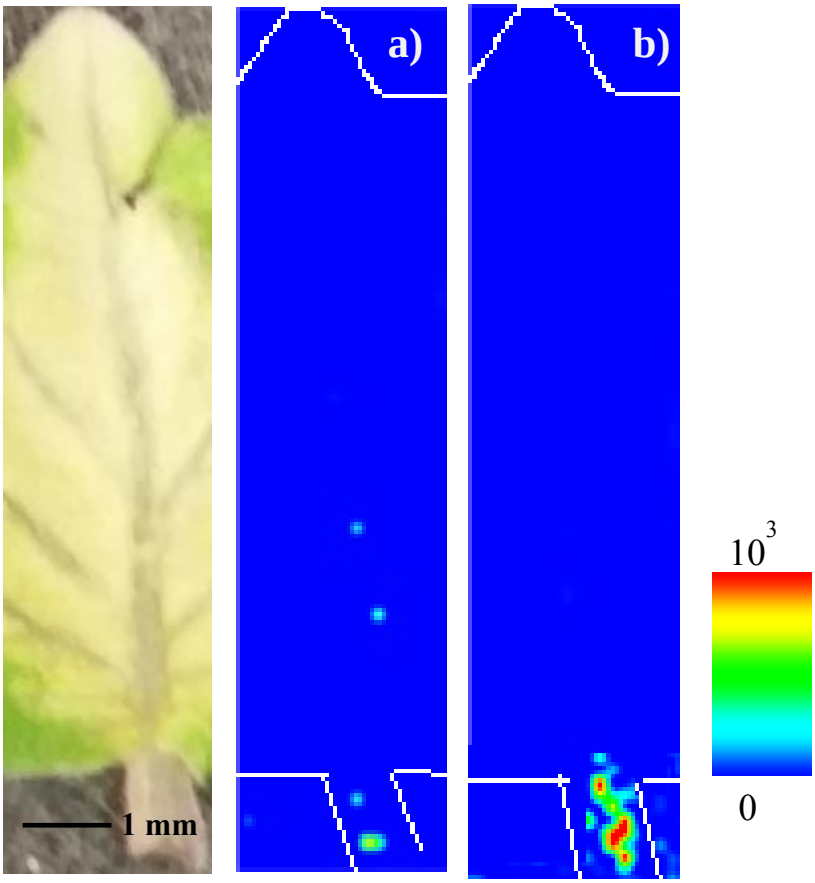

Figure A10. Images for positive anthocyanin images from jade coleus: a) optical photograph of jade coleus prior to ablation. False color ion maps of jade at b) m/z 757.1986, shisonin, and, c) m/z 843.1920, malonylshisonin.

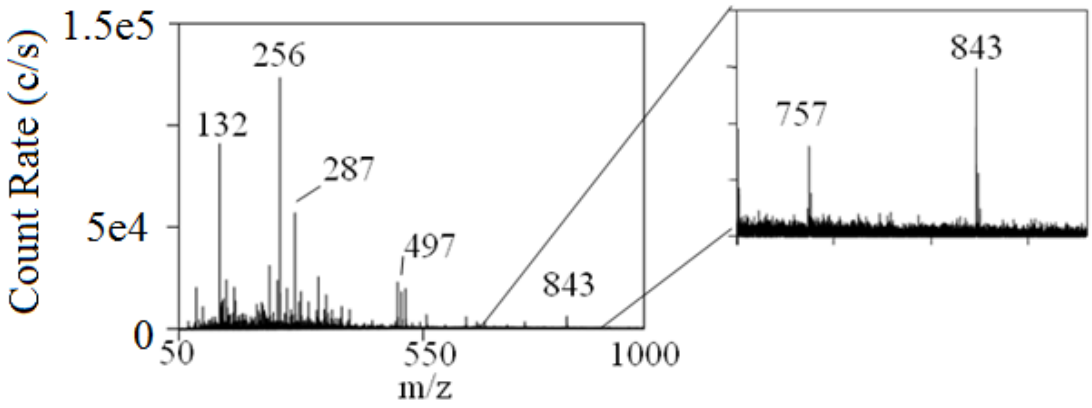

Figure A11. Time resolved mass spectrum of jade coleus taken at 1.36 minutes during a 2 minute acquisition. Inset (~5X zoomed) show the presence of shisonin (m/z 757.1986) and malonylshisonin (m/z 843.1920). This spectrum is not background subtracted.

Supplementary Materials
Prepared by Katherine-Jo Galayda and R.S. Houk

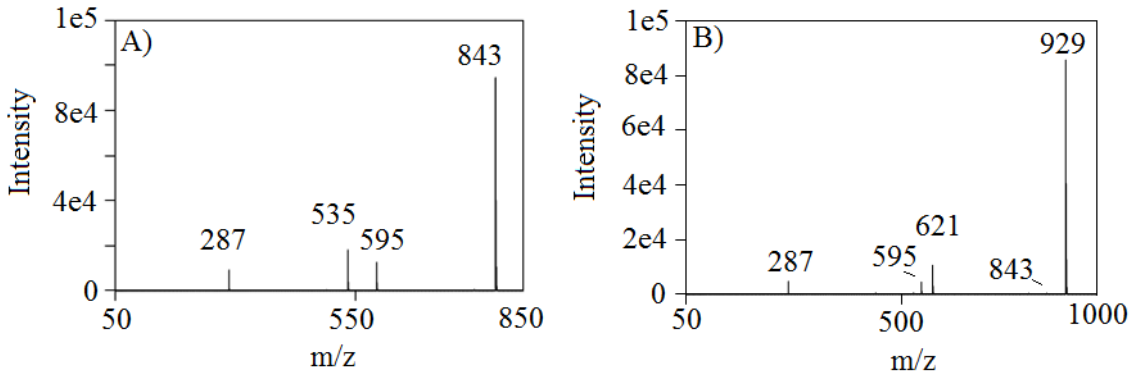

Figure AS1. MS/MS of the red section of broadstreet coleus taken by ambient-pressure UV-LAESI for A) m/z 843, malonylshisonin, and B) m/z 929, Cyanidin 3-(6”-p-coumarylglucoside)-5-4”, 6”-dimalonylglucoside. The collision energy for both was 15 eV.

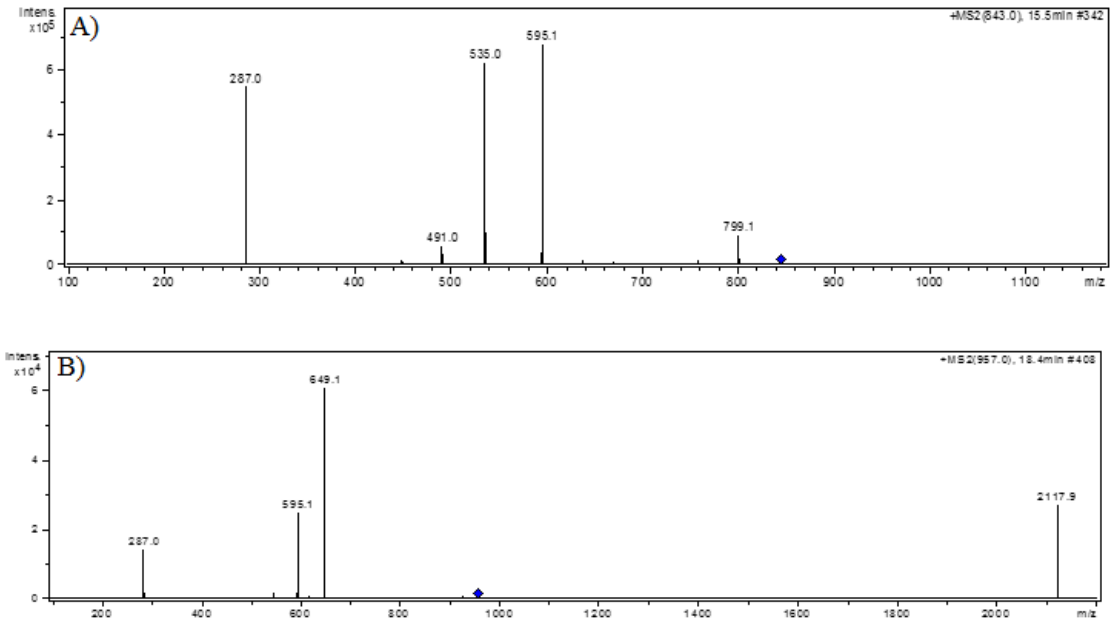

Figure AS2. MS/MS of the red section of broadstreet coleus taken by LC-MS. A) m/z 843, malonylshisonin, and B) m/z 929, Cyanidin 3-(6”-p-coumarylglucoside)-5-4”, 6”-dimalonylglucoside. The results are similar to those taken by UV-LAESI.

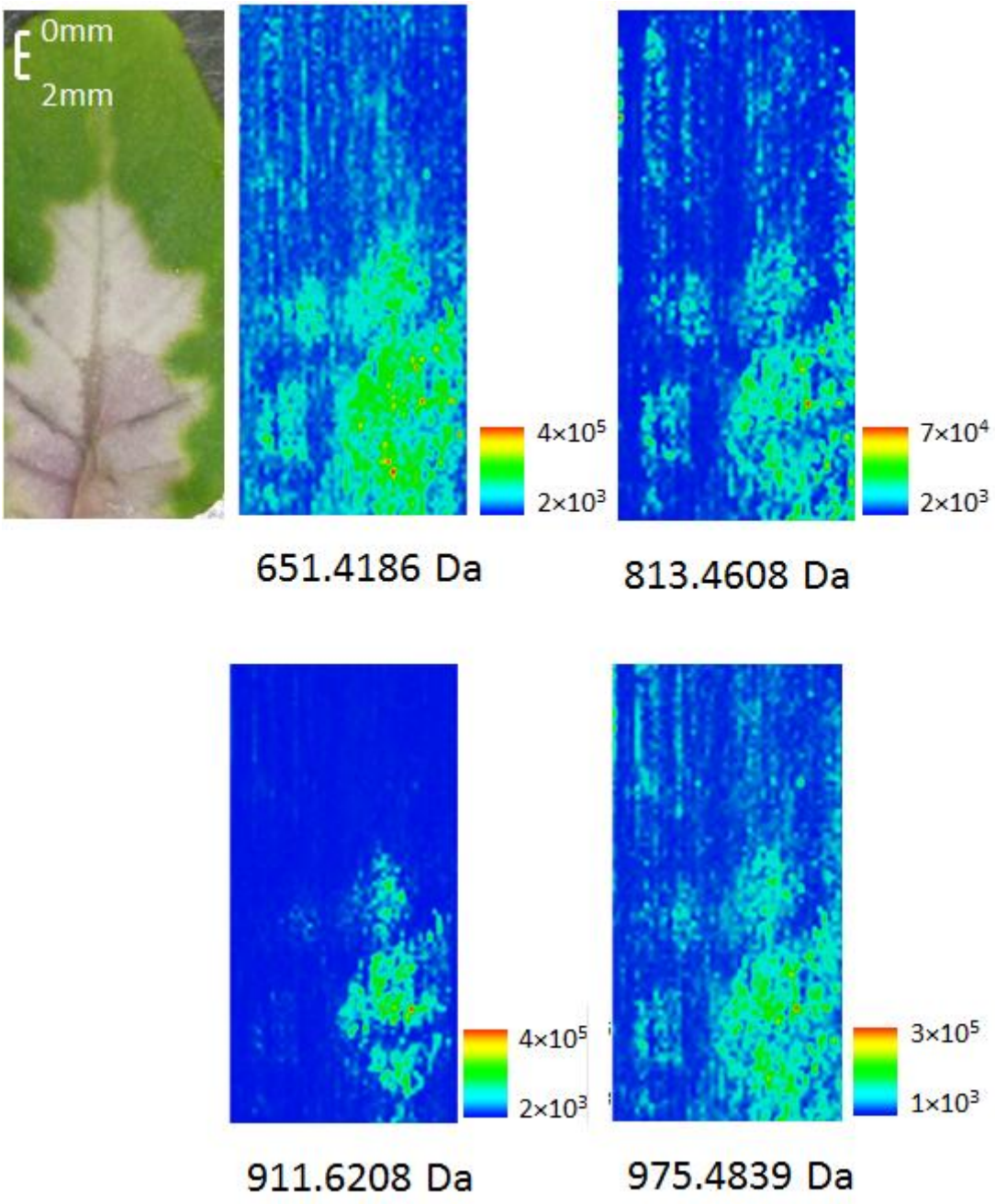

Figure AS3. Optical and positive images in Jade coleus leaves taken by ambient-pressure UV-LAESI. Due to the mass defect, it is assumed that the images represent lipids, although the actual IDs are unknown.

APPENDIX B.

AN INVERSE RUDDLESDEN-POPPER NITRIDE $Ca_7(Li_{1-x}Fe_x)Te_2N_2$ GROWN FROM Ca FLUX

A manuscript accepted by *Philosophical Magazine*

Gang Wang,[1,2,] S. Manni,[1,3] Qisheng Lin,[1,4] **Patrick A. McVey**,[1,4] Robert S. Houk,[1,4] Liming Wu,[5] Sergey L. Bud'ko,[1,3] and Paul C. Canfield[1,3]

[1]Ames Laboratory, Iowa State University, Ames, Iowa 50011, USA

[2]Research and Development Center for Functional Crystals, Beijing National Laboratory for Condensed Matter Physics, Institute of Physics, Chinese Academy of Sciences, Beijing 100190, China

[3]Department of Physics and Astronomy, Iowa State University, Ames, Iowa 50011, USA

[4]Department of Chemistry, Iowa State University, Ames, Iowa 50011, USA

[5]College of Chemistry, Beijing Normal University, Beijing 100875, China

Abstract

Nitridoferrates containing monovalent iron ions are a class of materials of recent interest as potentially novel magnetic materials. Aiming at the exploration of nitridoferrates of calcium, we report the single crystal growth from Ca flux and crystal structure of the first member (n = 2) of a series of inverse Ruddlesden-Popper nitride with a general formula of $A_{n-1}A'_2B_nX_{3n+1}$, where A = Li/Fe, A' = Te, B = N, and X = Ca. Single crystal X-ray diffraction analyses indicate the crystal with a composition of $Ca_7(Li_{0.32(1)}Fe_{0.68(1)})Te_2N_2$ and the tetragonal space group *I*4/*mmm* (a = 4.7884 (1)Å, c =

25.3723(4) Å, Z = 2). The structure features alternately stacking NaCl-type A'X slabs and the perovskite-type ABX_3 slabs along the *c* axis. The Li/Fe atoms are located in cuboctahedral cavities surrounded by eight Ca_6N octahedra in the ABX_3 slab. This work demonstrates the viability of the Ca-rich flux as a suitable solvent for the exploration of new complex nitrides with interesting crystal structure and properties.

Keywords

Nitrides; flux method; crystal structure

Introduction

Binary nitride materials have attracted strong interest in both science and technology for their properties over the past decades. GaN and its III-V solid solutions are semiconductors widely used for light emitting diode, laser diode, photodetector, and sensor application [1-5]. NbN, ZrN, and HfN are well known superconductors with relatively high superconducting transition temperatures for conventional superconductors [6-8]. Hexagonal BN is a good lubricant over wide temperature range and a two-dimensional (2D) material offering a remarkable opportunity for advanced 2D devices [9,10]. Cubic BN and wurtzite BN are reported to have hardness comparable to diamond [11,12].

More recently, interest in complex nitrides, like ternary and quaternary nitrides, has increased due to their specific properties [13]. Among complex nitrides, nitridoferrates of alkaline and alkaline earth metals, containing monovalent iron have attracted specific attention. Up to now, several nitridoferrates featuring one-

dimensional (1D) N-(Li/Fe)-N chains, such as $Li_2[(Li_{1-x}Fe_x)N]$ [14,15], $CaLi_2[(Li_{1-x}Fe_x)N]_2$ [16], $SrLi_2[(Li_{1-x}Fex)N]_2$ [16], $Ca_2\{Li[(Li_{1-x}Fe_x)N_2]\}$ [17], and $Li_2Sr[Li_{1-x}Fe_xN]_2$ [18] have been reported. $Li_2[(Li_{1-x}Fe_x)N]$ [15] and $Li_2Sr[Li_{1-x}Fe_xN]_2$ [18] have remarkable magnetic anisotropy and coercivity, which are desired for functional magnetic materials. Unlike the infinite N-(Li/Fe)-N chains, discrete N-(Li/Fe)-N linear blocks surrounded by Ca ion were discovered in the newly synthesized $Ca_6(Li_{1-x}Fe_x)Te_2N_3$ [19,20], which demonstrates the variety of possible coordination environments for the (Li/Fe)-N units.

Compared with their oxide counterparts, the growth and study of complex nitrides is difficult. Elemental nitrogen usually forms the diatomic molecule N_2 which has a strong covalent triple bond. The transition from atomic N to a N^{-3} anion needs to overcome a high energy barrier. Many of the nitrides are metastable phases and easily decompose. On one hand, these issues contribute to the challenge of synthesizing nitride materials. On the other hand, this situation offers a vast unexplored territory and creates excellent opportunities to discover new nitride materials with interesting crystal structures and properties by developing suitable synthetic methods to overcome these obstacles.

Tremendous efforts have been devoted to preparing nitrides by solid-state reaction [21], ammonolysis [22], solid-state metathesis [23,24], vapor deposition [25], carbothermal reduction [26], reactive sputtering [27], precursor decomposition [28], solvothermal process [29], and solution growth [30,31]. The solution growth method utilizes low melting point metals, such as alkaline metals or alkaline earth metals, as flux, dissolves reactants and facilitates reactions by attenuating the energy barrier for

breaking the N-N bonding. Na, Li, and Ca flux have been successfully used to grow GaN single crystal [32-37], as well as other nitrides [31]. As such, the viability of alkaline metal and alkaline earth metal fluxes should definitely not be limited to the single crystal growth of binary nitrides.

Nitrogen is highly soluble in Ca [38], which also has a moderately high melting point 842 °C. The eutectic point of Ca-Ca_3N_2 is determined to be at 1.94 at.% N and 814 °C [39]. As such, Ca-rich flux is postulated to be a suitable solvent for the exploration of complex nitrides of calcium. Here we report the discovery of an inversed Ruddlesden-Popper (RP) nitride $Ca_7(Li_{1-x}Fe_x)Te_2N_2$ with x = 0.68(1) grown by Ca flux. It crystallizes in the tetragonal space group *I*4/*mmm* and contains a Li/Fe mixed site inside the cuboctahedral cavities defined by Ca_6N octahedra.

Experimental

$Ca_7(Li_{1-x}Fe_x)Te_2N_2$ single crystals were grown by the solution growth method out of Ca-rich flux. Distilled Ca pieces (> 99.9%, Material Preparation Center (MPC), Ames Laboratory), lithium foil (99.9%, Alfa Aesar), tellurium (99.999%, Alfa Aesar), iron (99.99%, Alfa Aesar), and Ca_3N_2 (99%, Alfa Aesar) were weighed in the molar ratios of Ca:Li:Te:Fe:Ca_3N_2 = 7:1:1:0.1:1 and put inside a three-cap Ta crucible in an argon-filled glovebox [31]. The Ta crucible was sealed by arc welding under argon and loaded into an amorphous silica ampoule, which was sealed under roughly 0.2 atmosphere argon to prevent the oxidization of Ta during the growth process. The growth ampoule was heated over 3 hours to 450 °C, held for 3 hours to melt tellurium and to react the

elements, then heated over 12 hours to 1100 °C, held at this temperature for 4 hours, slowly cooled to 875 °C over 74 hours, and finally the assembly was decanted in a centrifuge to separate crystals from the remaining liquid. The $Ca_7(Li_{1-x}Fe_x)Te_2N_2$ crystals grow as rods with diameters ranging from several tens microns to millimeters and of lengths up to 7 mm, see Fig. 1. Single crystals of $Ca_7(Li_{1-x}Fe_x)Te_2N_2$ are very air sensitive and degrade within a few minutes in air. Besides $Ca_7(Li_{1-x}Fe_x)Te_2N_2$, CaTe was found as a byproduct.

Small $Ca_7(Li_{1-x}Fe_x)Te_2N_2$ pieces were selected under a microscope in a nitrogen-filled glovebox and sealed in quartz capillaries. Single-crystal X-ray diffraction data were collected at room temperature using a Bruker APEX II diffractometer equipped with a CCD area detector with Mo Kα radiation. Refinements of the diffraction data were performed using the SHELXTL package [40].

The chemical compositions of $Ca_7(Li_{1-x}Fe_x)Te_2N_2$ single crystals were determined using a Bruker Aurora Elite Inductively Coupled Plasma Mass Spectrometer (ICP–MS) without collision gas. Samples were dissolved in 1% nitric acid, 1% hydrochloric acid solutions. The total mass of solute ranged from 0.6 mg to 3.4 mg, with a final sample solution concentration of 500 ppb. The isotopes analyzed were $^{7}Li^{+}$, $^{42}Ca^{+}$, $^{43}Ca^{+}$, $^{44}Ca^{+}$, $^{56}Fe^{+}$, $^{57}Fe^{+}$, and $^{125}Te^{+}$. External calibration curves of net signal vs. concentration were created using standard concentrations of 20, 200, and 2000 ppb. The molar ratios of (Li+Fe)/Ca and Li/Fe were determined as 0.147 and 0.471, respectively. The [(standard deviation/mean result) * 100] (%RSD) of the solution concentration in ppb for Li, Fe, and Ca are 1.25, 0.08, and 0.79, respectively.

The isothermal magnetization of $Ca_7(Li_{1-x}Fe_x)Te_2N_2$ was measured as a function of magnetic fields (up to ± 5 T) that were applied parallel and perpendicular to the rod at 5 K and 300 K. No apparent magnetic anisotropy between the two measured directions was observed. The saturated magnetic moments for both directions are about 0.02 μ_B/Fe, likely a result of impurity We tried to measure the resistance of $Ca_7(Li_{1-x}Fe_x)Te_2N_2$ crystals by multimeter or making contacts using silver paint in the nitrogen-filled glovebox. In both cases, the resistance (sample and/or contacts) was too large to be measured.

Results and discussion

The crystal structure was determined by direct method in the tetragonal structure with space group *I*4/*mmm*, in which the five independent metal sites were identified. Atomic assignments were made on the basis of peak intensities and bond distances to neighboring atoms. Subsequent difference Fourier map yield the N site. The final refinement with anisotropic displacement parameters yielded a formula of $Ca_7(Li_{0.32(1)}Fe_{0.68(1)})Te_2N_2$. This proportion is consistent with the chemical composition determined by ICP–MS, which yielded a molar ratio of (Li+Fe)/Ca~0.147. Representative crystallographic data of the structural refinement are listed in Tables 1, 2, and 3. denote Ca atoms, with atomic sequence marked as given in Table 2. Purple and blue spheres denote Fe/Li and Te atoms, respectively. Representative bond distances are also marked.

As shown in Fig. 2(a), the structure of $Ca_7(Li_{0.32(1)}Fe_{0.68(1)})Te_2N_2$ manifest nitrogen centered Ca_6 octahedra, defined by four Ca1 atoms on the waist, and one Ca2 atom capping on the top and one Ca3 capping on the bottom. The Ca_6N octahedra are slightly distorted along *c*-axis, as indicated by the bond distance of d_{N-Ca2} = 2.325(3) Å and d_{N-Ca3} = 2.495(3) Å (see Table 3). These Ca-N distances of 2.325(3) Å, 2.4055(3) Å (d_{N-Ca1}), and 2.495(3) Å are within the range of reported Ca-N bond lengths for Ca_3N_2 (2.46 Å), $Ca_{11}N_8$ (2.308-2.900 Å), and Ca_2N (2.4426(4) Å) [41-43]. All Ca1 and Ca3 atoms are shared by neighboring octahedra to form 2D perovskite-type ABX_3 slabs, which are stacked along *c*-axis and separated by the more electronegative Te atoms. The Fe/Li atoms are located at the centers of cuboctahedral cavities in the perovskite layers, shown in Fig. 3(a). The (Fe/Li)-Ca distances are 3.2930(4)-3.3859(1) Å, within the range of Ca-Li and Ce-Fe distances commonly observed in intermetallics, e.g., $d_{Ca\text{-}Li}$ = 3.672 Å in Laves phase $CaLi_2$ [44] and $d_{Ca\text{-}Fe}$ = 3.219(1) Å in $CaFe_2Si_2$ [45]. The Te atoms in $Ca_7(Li_{0.32(1)}Fe_{0.68(1)})Te_2N_2$ are located between neighboring perovskites slabs; each has nine neighboring Ca atoms in its first coordinating sphere, shown in Figure 3(b).

Simply judging from the formula of $Ca_7(Li_{0.32(1)}Fe_{0.68(1)})Te_2N_2$, the title 7-1-2-2 phase seems to have certain underpinned relationship with $Ca_6Li_{0.48}Fe_{0.52}Te_2N_3$ [19], or in short, 6-1-2-3 phase. However, their differences are remarkable: (1) there are two sets of N atoms in the 6-1-2-3 structure, one with octahedral coordination of six calcium atoms and the other with five calcium and one Fe/Li atoms, as shown in Fig. 2(b). Noteworthy is that Fe in the 6-1-2-3 phase can be considered as a cationic atom with a rare formal charge of +1 (d^6s^1 configuration), as confirmed by susceptibility data and

theory calculations [19]. Yet the same is not true for the 7-1-2-2 phase, which in fact is a metallic phase. (2) The Fe/Li-Fe/Li separation in the 6-1-2-3 phase is *c*/2 = 3.36 Å [19]. However, each Fe/Li in the 6-1-2-3 structure has direct bonding interaction with two electronegative N atoms with a distance of 1.86 Å. This could yield Fe-N-Fe super-exchange interactions as indicated by susceptibility data [19]. In contrast, Fe/Li in perovskite-type layer of the 7-1-2-2 phase is surrounded by 12 Ca atoms and no direct Fe/Li-N bonding exists as the separation is 4.7884(1) Å. Therefore, this material likely does not show strong magnetic response because of an expected electron delocalization in the Ca_3N(Fe/Li) perovskite slab with intermetallic nature. In other words, the local region in the perovskite slabs is in fact dominated by homoatomic Ca-Ca and heteroatomic Ca-Fe/Li metallic bonding interactions. Although susceptibility and resistance data for $Ca_7(Li_{0.32(1)}Fe_{0.68(1)})Te_2N_2$ are not available, metallic luster is seen for the title crystals (cf. Figure 1).

In fact, the present 7-1-2-2 structure can be considered as the first member (n = 2) of an inverse RP phase, with a general formula of $A_{n-1}A'_2B_nX_{3n+1}$, here A = Li/Fe, A' = Te, B = N, and X = Ca. This type structure features alternately stacking NaCl-type A'X slabs and the perovskite-type ABX_3 slabs along the long axis. With this formula in hand, a series of new phases in the same system could be designed and to be synthesized by stoichiometric solid-state reactions, e.g., Ca_4Te_2N (n = 1) and $Ca_{10}(Li_{1-x}Fe_x)_2Te_2N_3$ (n = 3).

Conclusions

A novel inverse RP nitride $Ca_7(Li_{1-x}Fe_x)Te_2N_2$ with x = 0.68(1) was successfully grown from Ca flux. The single-crystal XRD indicates that it crystallizes in the tetragonal space group *I*4/*mmm* and contains Li/Fe ions located in cuboctahedral cavities in the perovskite-type layers formed by Ca_6N octahedra. This work demonstrates the viability of Ca flux to crystallize new complex nitride, and predicts the existence of a series of new inversed RP phases in the title system.

Supporting Information

The following file is available free of charge.

Crystallographic Information Files (CIFs)

Acknowledgements

We would like to thank T. Kong, W. Straszheim, and U. S. Kaluarachchi for useful discussions and experimental assistance.

Disclosure statement

No potential conflict of interests was reported by the authors.

Funding

This work was supported by the U.S. Department of Energy, Office of Basic Energy Science, Division of Materials Sciences and Engineering. The research was performed at

the Ames Laboratory. Ames Laboratory is operated for the U.S. Department of Energy by Iowa State University under Contract No. DE-AC02-07CH11358. G. Wang was supported by the National Natural Science Foundation of China (Grant Nos. 51572291 and 51322211), the National Key Research and Development Program of China (Grant No. 2017YFA0302902), and the China Scholarship Council. SM was supported by the Gordon and Betty Moore Foundations EPiQS Initiative through Grant GBMF4411. The ICP–MS device was originally provided by Bruker, presently Analytik Jena.

References

[1] S. Strite and H. Morkoç, *GaN, AlN, and InN: A review*, J. Vac. Sci. Tech. B 10 (1992), pp. 1237-1266.

[2] H. Morkoç, S. Strite, G.B. Gao, M.E. Lin, B. Sverdlov, and M. Burns, *Large-band-gap SiC, III-V nitride, and II-VI ZnSe-based semiconductor device technologies*, J. Appl. Phys. 76 (1994), pp. 1363-1398.

[3] S. Nakamura, M. Senoh, S.-I. Nagahama, N. Iwasa, T. Yamada, T. Matsushita, H. Kiyoku, and Y. Sugimoto, *InGaN-based multi-quantum-well-structure laser diodes*, Jpn. J. Appl. Phys. **1996**, 35 (1996), pp. L74-L76.

[4] F.A. Ponce and D.P. Bour, *Nitride-based semiconductors for blue and green light-emitting devices*, Nature 386 (1997), pp. 351-359.

[5] O. Ambacher, *Growth and applications of Group III-nitrides*, J. Phys. D: Appl. Phys. 31 (1998), pp. 2653-2710.

[6] B.T. Matthlas and J.K. Hulm, *A search for new superconducting compounds*, Phys. Rev. 87 (1952), pp. 799-806.

[7] B.T. Matthlas, *Transition temperatures of superconductors*, Phys. Rev. 92 (1953), pp. 874-876.

[8] X.-J. Chen, V.V. Struzhkin, Z.G. Wu, M. Somayazulu, J. Qian, S. Kung, A.N. Christensen, Y.S. Zhao, R.E. Cohen, H.-K. Mao, and R.J. Hemley, *Hard superconducting nitrides*, Proc. Natl. Acad. Sci. USA 102 (2005), pp. 3198-3201.

[9] R. Haubner, M. Wilhelm, R. Weissenbacher, and B. Lux, *In Book Series in Structure and Bonding, volume 102: High Performance Non-Oxide Ceramics II*, Springer, 2002, Chap. 1, pp. 1-45.

[10] L. Song, L.J. Ci, H. Lu, P.B. Sorokin, C.H. Jin, J. Ni, A.G. Kvashnin, D.G. Kvashnin, J. Lou, B.I. Yakobson, and P.M. Ajayan, *Large scale growth and characterization of atomic hexagonal boron nitride layers*, Nano Lett. 10 (2010), pp. 3209-3215.

[11] S.N. Monteiroa, A.L.D. Skuryb, M.G. Azevedob, and G.S. Bobrovnitchiib, *Cubic boron nitride competing with diamond as a superhard engineering material–an overview*, J. Mater. Res. Technol. 2 (2013), pp. 68-74.

[12] Z.C. Pan, H. Sun, Y. Zhang, and C.F. Chen, *Harder than diamond: Superior indentation strength of wurtzite BN and lonsdaleite*, Phys. Rev. Lett. 102 (2009), pp. 055503.

[13] R. Kniep, *Ternary and quaternary metal nitrides: A new challenge for solid state chemistry*, Pure Appl. Chem. 69 (1997), pp. 185-191.

[14] J. Klatyk and R. Kniep, *Crystal structure of dilithium (nitridolithiate/ferrate(I)), $Li_2((Li_{1-x}Fe_x)N)$ x = 0.63*, Z. Kristallogr. 214 (1999), pp. 447-448.

[15] A. Jesche, R.W. McCallum, S. Thimmaiah, J.L. Jacobs, V. Taufour, A. Kreyssig, R.S. Houk, S.L. Bud'ko, and P.C. Canfield, *Giant magnetic anisotropy and tunneling of the magnetization in $Li_2(Li_{1-x}Fe_x)N$*, Nature Commun. 5 (2014), pp. 3333.

[16] J. Klatyk and R. Kniep, *Crystal structure of alkaline earth dilithium bis(nitridolithiate/ferrates(I)), $CaLi_2[(Li_{1-x}Fe_x)N]_2$, x = 0.30 and $SrLi_2[(Li_{1-x}Fe_x)N]_2$, x = 0.46*, Z. Kristallogr. 214 (1999), pp. 449-450.

[17] J. Klatyk and R. Kniep, *Crystal structure of dicalcium (dinitridolithiate/ferrate(I)), $Ca_2\{Li[(Li_{1-x}Fe_x)N_2]\}$, x = 0.82*, Z. Kristallogr. 214 (1999), pp. 451-452.

[18] P. Höhn, T.J. Ball, M. Fix, Y. Prots, and A. Jesche, *Single crystal growth and anisotropic magnetic properties of $Li_2Sr[Li_{1-x}Fe_xN]_2$*, Inorganics 4 (2016), pp. 42.

[19] M.J. Dickman and S.E. Latturner, *Metal nitrides grown from Ca/Li Flux: $Ca_6Te_3N_2$ and new nitridoferrate(I) $Ca_6(Li_xFe_{1-x})Te_2N_3$*, J. Am. Chem. Soc. 138 (2016), pp. 10636-10644.

[20] X.-W. Yan, Z.B. Huang, C.F. Zhang, M. Gao, L. Chen, G.H. Zhong, and H.-Q. Lin, *Magnetic moment and spin state transition on rare monovalent iron ion in nitridoferrate $Ca_6Li_{0.5}Fe_{0.5}Te_2N_3$*, J. Mater. Chem. C 5 (2017), pp. 733-737.

[21] D.H. Gregory, *Structural families in nitride chemistry*, J. Chem. Soc., Dalton Trans. 3 (1999), pp. 259-270.

[22] P.S. Herle, M.S. Hegde, N.Y. Vasathacharya, S. Philip, M.V. Rama Rao, and T. Sripathi, *Synthesis of TiN, VN, and CrN from ammonolysis of TiS_2, VS_2, and Cr_2S_3*, J. Solid State Chem. 134 (1997), pp. 120-127.

[23] E.G. Gillan and R.B. Kaner, *Rapid solid-state synthesis of refractory nitrides*, Inorg. Chem. **1994**, 33 (1994), pp. 5693-5700.

[24] B. Song, J.K. Jian, G. Wang, M. Lei, Y.P. Xu, and X.L. Chen, *Facile and general route to nitrides by a modified solid-state metathesis pathway*, Chem. Mater. 19 (2007), pp. 1497-1502.

[25] S.C. Jain, M. Willander, J. Narayan, and R. Van Overstraeten, *III–nitrides: Growth, characterization, and properties*, J. Appl. Phys. 87 (2000), pp. 965-1006.

[26] H.Z. Zhao, M. Lei, X.A. Yang, J.K. Jian, and X.L. Chen, *Route to GaN and VN assisted by carbothermal reduction process*, J. Am. Chem. Soc. 127 (2005), pp. 15722-15723.

[27] J. Pelleg. L.Z. Zevin, and S. Lungo, *Reactive-sputter-deposited TiN films on glass substrates*, Thin Solid Films 197 (1991), pp. 117-128.

[28] P. Gibart, *Metal organic vapour phase epitaxy of GaN and lateral overgrowth*, Rep. Prog. Phys. 67 (2004), pp. 667-715.
[29] B.G. Wang and M.J. Callahan, *Ammonothermal synthesis of III-nitride crystals*, Crystal Growth Des. 6 (2006), pp. 1227-1246.
[30] E. Meissner, S. Hussy, and J. Friedrich, *In Book Series in Springer Series in Materials Science, Volume 133: Technology of Gallium Nitride Crystal Growth*, Springer, 2002, Chap. 12, pp. 245-273.
[31] A. Jesche and P.C. Canfield, *Single crystal growth from light, volatile and reactive materials using lithium and calcium flux*, Philos. Mag. 94 (2014), pp. 2372-2402.
[32] H. Yamane, M. Shimada, S.J. Clarke, and F.J. DiSalvo, *Preparation of GaN single crystals using a Na flux*, Chem. Mater. 9 (1997), pp. 413-416.
[33] Y.T. Song, W.J. Wang, W.X. Yuan, X. Wu, and X.L. Chen, *Bulk GaN single crystals: Growth conditions by flux method*, J. Cryst. Growth 247 (2003), pp. 275-278.
[34] G. Wang, J.K. Jian, W.X. Yuan, and X.L. Chen, *Growth of GaN single crystals using Ca-Li_3N composite flux*, Cryst. Growth Des. 6 (2006), pp. 1157-1160.
[35] J.K. Jian, G.Wang, C. Wang, W.X. Yuan, and X.L. Chen, *GaN single crystals grown under moderate nitrogen pressure by a new flux: Ca_3N_2*, J. Cryst. Growth 291 (2006), pp. 72-76.
[36] G. Wang, W.X. Yuan, J.K. Jian, H.Q. Bao, J.F. Wang, X.L. Chen, and J.K. Liang, *Growth of GaN single crystals by Ca_3N_2 flux*, Scripta Mater. 58 (2008), pp. 319-322.
[37] G. Wang and X.L. Chen, *Single-crystal growth: From new borates to industrial semiconductors*, Phys. Status Solidi A 207 (2010), pp. 2757-2768.
[38] V. P. Itkin and C. B.Alcock, *CaN phase diagram, In ASM Alloy Phase Diagrams Center*, P. Villars, H. Okamoto, and K. Cenzual, eds. ASM International, Materials Park, OH, 1990. Available at http://www1.asminternational.org/AsmEnterprise/APD
[39] G. Wang, W.X. Yuan, J.F. Wang, X. Zhao, J.K. Jian, and X.L. Chen, *Thermodynamic assessment of the Ca–Ca_3N_2 system*, Mater. Lett. 61 (2007), pp. 2266-2269.
[40] G.M. Sheldrick, *SHELXL-97. Program for the Solution of Crystal Structures*, University of Göttingen, Germany 1997.
[41] P.Y. Laurent, J. Lang, and E.M.T. Le Bihan, *Structure du nitrure de calcium α*, Acta Cryst. B 24 (1968), pp. 494-499.
[42] P.Y. Laurent, J. Lang, and E.M.T. Le Bihan, *Structure d'un nouveau nitrure de calcium: $Ca_{11}N_8$*, Acta Cryst. B 25 (1969), pp. 199-203.
[43] D.H. Gregory, A. Bowman, C.F. Baker, and D.P. Weston, *Dicalcium nitride, Ca_2N-A 2D "excess electron" compound; synthetic routes and crystal chemistry*, J. Mater. Chem. 10 (2010), pp. 1635-1641.
[44] D. Fischer and M. Jansen, *Eine neue modifikation der Laves-phase $CaLi_2$*, Z. Anorg. Allg. Chem. 629 (2003), pp. 1934-1936.
[45] V. Hlukhyy, A. Hoffmann, and T.F. Fäessler, *Synthesis, structure and chemical bonding of $CaFe_{2-x}Rh_xSi_2$ (x = 0, 1.32, and 2) and $ScCo_2Si_2$*, J. Solid State Chem. 203 (2013), 232-239.

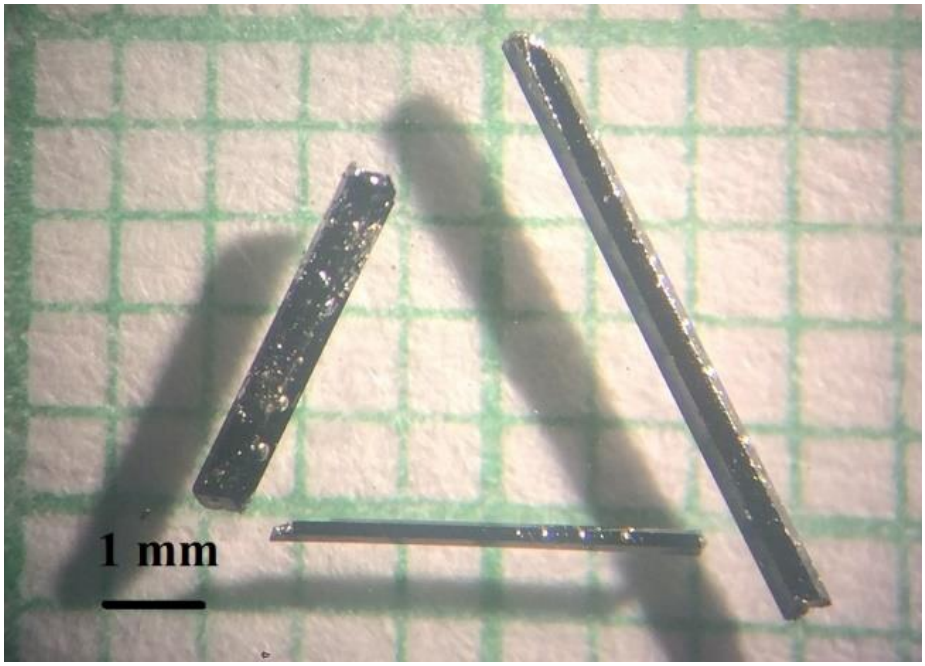

Figure B1. Optical photograph of $Ca_7(Li_{1-x}Fe_x)Te_2N_2$ single crystals.

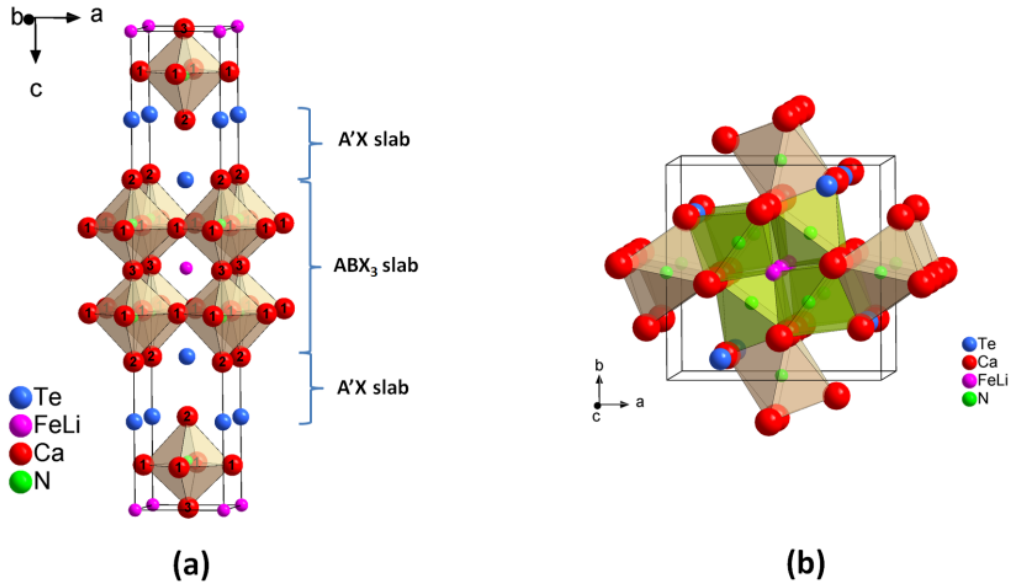

Figure B2. Crystal structures for (a) $Ca_7(Li_{0.32(1)}Fe_{0.68(1)})Te_2N_2$ and (b) $Ca_6Li_{0.48}Fe_{0.52}Te_2N_3$.

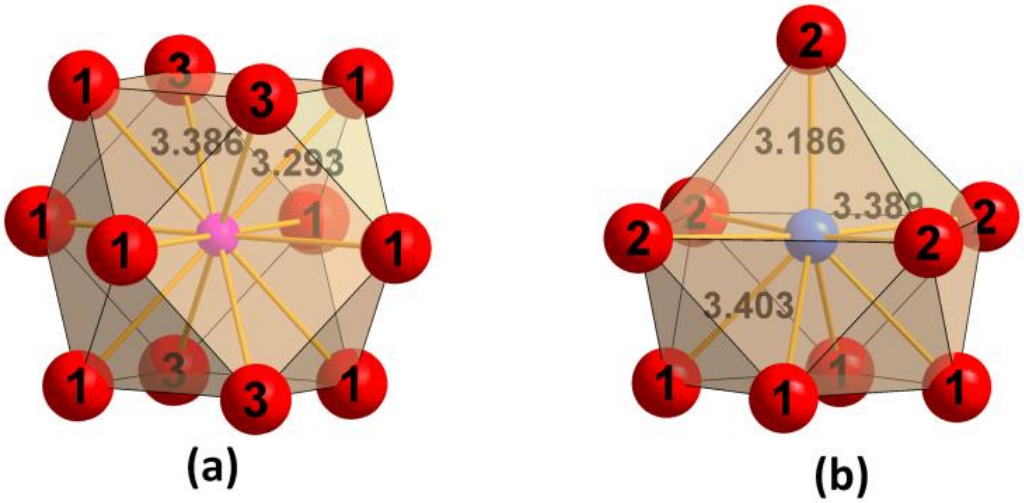

Figure B3. Environments of (a) Fe/Li and (b) Te in $Ca_7(Li_{0.32(1)}Fe_{0.68(1)})Te_2N_2$. Red spheres

Table B1. Crystal structure data of $Ca_7(Li_{0.32(1)}Fe_{0.68(1)})Te_2N_2$ obtained by structural refinement.

Empirical formula	**$Ca_7(Li_{0.32(1)}Fe_{0.68(1)})Te_2N_2$**
Space group, Z	*I*4/*mmm*, 2
Unit cell (Å)	a = 4.7884(1)
	c = 25.3723(4)
Vol. (Å^3)	V = 581.76(3)
d_{cal} (g/cm^3)	3.448
Reflections collected/R_{int}	8804/0.0302
Data/restraints/parameters	308/0/20
Goodness-of-fit on F^2	1.147
R1/wR2 [I>2σ(I)]	0.0118/0.0302
(all data)	0.0127/0.0305
Peak and hole (e.Å^{-3})	0.419/-0.517

Table B2. The refined atomic positions and equivalent isotropic displacement parameters for $Ca_7(Li_{0.32(1)}Fe_{0.68(1)})Te_2N_2$.

Atom	Wyck.	Site	S.O.F.	*x*	*y*	*z*	U_{eq} (Å^2)
Te	4e	4mm		0	0	0.1845(1)	0.013(1)
Fe/Li	2a	4/mmm	0.680/0.320(5)	0	0	0	0.007(1)
Ca1	8g	2mm		0	0.5	0.08912(1)	0.013(1)
Ca2	4e	4mm		0	0	0.3100(1)	0.017(1)
Ca3	2b	4/mmm		0	0	1/2	0.016(1)
N	4e	4mm		0	0	0.4017(1)	0.007(1)

Table B3. Environments and bond distances around Te, Fe/Li, and N atoms in $Ca_7(Li_{0.32(1)}Fe_{0.68(1)})Te_2N_2$, and selected interatomic distances between Ca atoms.

Bond	Distance (Å)	Bond	Distance (Å)	Bond	Distance (Å)
Te-Ca1 x 4	3.4032(5)	Fe/Li-Ca1 x 4	3.2930(4)	N-Ca1 x 4	2.4055(3)
Te-Ca2 x 1	3.1862(9)	Fe/Li-Ca1 x 4	3.2933(4)	N-Ca2 x 1	2.325(3)
Te-Ca2 x 4	3.3888(1)	Fe/Li-Ca3 x 4	3.3859(1)	N-Ca3 x 1	2.495(3)
Ca1-Ca1	3.3859(1)	Ca1-Ca2	3.5044(8)	Ca1-Ca3	3.2934(4)
		Ca1-Ca2	3.5040(8)	Ca1-Ca3	3.2930(4)